Title
The Dynamic Organization of the Yeast Genome

Author
Joyner, Ryan Preston

Publication Date
2014

Peer reviewed|Thesis/dissertation

The Dynamic Organization of the Yeast Genome

by

Ryan Preston Joyner

A dissertation submitted in partial satisfaction of the

requirements for the degree of

Doctor of Philosophy

in

Molecular and Cell Biology

in the

Graduate Division

of the

University of California, Berkeley

Committee in charge:

Professor Karsten Weis, Chair
Professor Jasper Rine
Professor Gary Karpen
Professor Peter Quail

Spring 2014

The Dynamic Organization of the Yeast Genome

Abstract

The Dynamic Genome Organization of the Yeast Genome

by

Ryan Preston Joyner

Doctor of Philosophy in Molecular and Cell Biology

University of California, Berkeley

Professor Karsten Weis, Chair

Regardless of size, shape, or function, all cells must rapidly respond to a changing environment, especially in adverse conditions. Various environmental stresses including heat shock, osmotic stress, and nutrient starvation consequently induce dramatic changes in the molecular composition of cellular machinery. Importantly, the cell's adjustment to a new homeostasis is accomplished through a variety of mechanisms, but most predominantly through the regulation of gene expression which is normally thought to function through the interplay of specific transcriptional repressors and activators. Recent evidence suggests, however, that more novel forms of transcriptional regulation may exist, including the repositioning of specific genes to distinct subdomains within the nucleus and through global changes in genome organization. Moreover, it has been hypothesized that such changes may function to supplement more traditional models of transcriptional regulation. Thus, upon environmental stress, cells may dramatically modify global transcriptional programs through a reorganization of their genome, facilitating a more rapid response to an adverse environment. The budding yeast *Saccharomyces cerevisiae* represents a remarkable model for elucidating how the organization of the genome and the repositioning of specific genes may function to regulate gene expression. In yeast, certain cellular stresses are known to stimulate the repositioning of genes within the nucleus and alter the global organization of the genome. Despite considerable research into the dynamic nature of genome organization, however, many questions remain as to the true function of gene positioning and the mechanism(s) by which cells establish specific organizational conformations of the genome.

In the following dissertation, I first provide evidence on the function of repositioning a specific gene to the nuclear periphery by examining the consequences of improperly localizing the *GAL* locus of budding yeast. Next, I describe my attempts to discern the coordinated diffusion of co-regulated genes as well as my findings on the independent movement of loci positioned various distances apart on the same chromosome. Finally, I describe novel findings on the mechanism of chromatin mobility through experiments focused on understanding the biological determinants of intracellular diffusion. Together, my results suggest that chromatin mobility is, in part, actively driven, which may function to facilitate more rapid alterations in genome organization and thus more rapid regulation of gene expression.

I first set out to understand the function of repositioning specific genes to distinct locations within the nucleus. In yeast, the *GAL* locus, comprised of *GAL1, GAL7,* and *GAL10* and necessary for the metabolism of galactose, re-localizes from a central position of the nucleus when repressed to the nuclear periphery when transcriptionally active. To understand the function of this specific repositioning, I took advantage of mutants in different macromolecular complexes, namely the nuclear pore complex and the SAGA transcriptional complex, which both fail to properly localize the *GAL* locus. I demonstrate that the *GAL* locus is negatively regulated at the nuclear periphery as both mutants, when compared to wild- type, displayed massively upregulated transcription of *GAL1* upon activation and a distinct lag in repression. Importantly, the increased induction kinetics of *GAL1* mRNA is mirrored by increased expression levels of GAL1 protein, suggesting that the over-expressed *GAL1* mRNA is functional and that export of the mRNA is not perturbed despite the mislocalization of the *GAL* locus. In my model, the *GAL* locus is positioned at the nuclear periphery to facilitate more rapid transcriptional repression when cells encounter their preferred carbon source, glucose.

Co-regulated genes may localize to transcriptional complexes known as transcription factories, hypothesized to facilitate more rapid and efficient transcription through colocalization and sequestration of specific transcriptional machinery. Because the *GAL* locus is known to re-localize at or near nuclear pore complexes upon activation, which may provide a scaffold for such transcriptional machinery, I next sought to observe transcription-induced coordinated diffusion of the two *GAL* loci within diploid yeast. To do so, I utilized a microscope capable of tracking both uniquely-labeled loci simultaneously using a double-helical point spread function. Although I did not discern evidence of potential transcription factories, I did reveal insights into the flexibility of chromatin by analyzing intrachromosomal loci separated by known distances. Overall, my results suggest that coordinated mobility of distinct loci correlates directly with their distance apart in space, regardless if they are intra or interchromosomal.

Finally, I explored the mechanism of chromatin mobility and, thereby, the driving force behind the re-organization of the genome by comparing the diffusion rates of chromatin and other macromolecules in distinct conditions. I began my investigation by starving cells of glucose and determining the effect on macromolecular mobility. Interestingly, both chromatin and mRNPs (messenger ribonucleoprotein particles) display a massive confinement in their mobility in such conditions. The reduction in mobility cannot be explained by a decrease in ATP, but can be replicated through a reduction of intracellular pH. I then show that both glucose starvation and reduction of intracellular pH induce a decrease in cell volume, increasing molecular crowding and reducing macromolecular mobility. Furthermore, I demonstrate a dependence of chromatin mobility on the cytoskeleton as simultaneous treatment with actin and microtubule depolymerizers specifically confines chromatin mobility. Lastly, by uncoupling metabolism and macromolecular mobility I propose that the preservation of an optimal cell volume is signaled independently from the energy status of the cell and discuss implications and future directions of this work.

Dedication

This work is dedicated to my incredibly supportive parents, my inspiring sister, and my wonderful, loving wife.

Acknowledgements

I owe a tremendous amount of gratitude to the chair of my thesis committee and my advisor, Karsten Weis. His steadfast commitment to the development of his students as scientists and as critical thinkers is second-to-none. Thank you, Karsten, for your incredible patience even in the face of my stubbornness. I greatly appreciate your enthusiasm for my pursuits outside of the lab and your unwavering support within it. It goes without saying that none of the work described here would have been possible without your guidance. Along the same vein, I would also like to thank my thesis committee members, Jasper Rine, Gary Karpen, and Peter Quail for their considerable support, advice, and thoughtfulness throughout the completion of this work. Thank you, as well, to our wonderful collaborators Mikael Backlund and W.E. Moerner.

In addition, I would like to thank all the members of the "Dot Project" subgroup including Erin Green, Ying Jiang, Ben Montpetit, and Zain Dossani, and all of our fantastic rotation students. I would like to especially thank Elisa Dultz for all of her help and tutelage with microscopy, coding, and just about everything else. The time it took to complete this work may have tripled without your assistance. You are a truly talented scientist and I was very lucky to learn from you.

Of course, special thanks go to other members of the lab as well. Leon Chan, thank you for your patience, your willingness to share your wealth of knowledge, and for shouldering a substantial amount of responsibility at a time when the rest of us really needed it. Christiane Brune, thank you for keeping everything afloat in lab. You always have the best wisdom and know the best times to share it. Chris "Big Mug" Mugler, thank you for your insightful suggestions and for constantly raising lab morale. Lab would not have been the same without you, baymate. I would like to also thank Matt Welch and Rebecca Heald and all members of the Trilab. The greatness that was the Trilab, especially the Halloween parties, will not be forgotten. I was very fortunate to work in close proximity with so many great and considerate people.

Outside of the lab, I would like to thank the greatest scientist softball team to ever take the field, The Foul Tips. Your debauchery was truly inspiring. As well, I would like to thank Robbie Calderon and Nicholas Justice for all the trips to Thai Noodle, Bobby G's, Raleigh's (R.I.P.), and Turkish Kitchen, in addition to the privilege to call you friends. Thank you for all the laughs. Thank you to my Aunt Terilyn Palanca for your encouragement and helpful advice when selecting a school.

In closing, I would like to thank my truly amazing parents, Danny and Toni Joyner, for their unrelenting support and encouragement. Thank you, additionally, to my sister and one of my best friends, Erin Joyner. My family has always been my greatest source of inspiration and admiration. You are my heroes and I thank you for all that you have done for me. To my wife, Megan Joyner, thank you for your constant reassurance, love, and encouragement. You are my rock. The completion of this journey would not have been possible without you.

Table of Contents

Chapter 1:

Introduction

Understanding the Functional yet Dynamic Organization of the Genome

From differentiation to apoptosis, the elegant regulation of transcription and its products ultimately drives the cellular responses and changes essential throughout the lifecycle of every organism. Consequently, cells have evolved a host of mechanisms to tightly control the temporal abundance of specific transcripts. One such mechanism, garnering more and more appreciation, is the non-random organization of the genome, beginning with the compaction of DNA and culminating in the dynamic localization of specific genes. Although early cytological studies of eukaryotic cells first established the non-random organization of the genome, our understanding of its function has expanded tremendously with technical advancements. For instance, with current methods and improvements in fluorescent microscopy, researchers can now sequentially track the localization and mobility of specific genes to investigate how and why chromatin repositions upon cellular stress. In this section I will describe the hallmarks of genome organization, progress in understanding how the cell adopts a specific configuration and, ultimately, how that organization may function to regulate gene expression.

Properties of Hierarchal Genome Organization in Eukaryotes

The Nucleus

To understand genome organization, a brief review of the nucleus and its constituent components is essential given that it serves as the host organelle for the eukaryotic genome and its defining characteristic (**Fig 1.1A**). The nucleus is demarcated by the nuclear envelope (NE), a double membrane bilayer which is contiguous with the endoplasmic reticulum (Fernandez-Martinez and Rout, 2009). The inner nuclear envelope serves as a platform for integral membrane proteins and membrane-associated proteins. For instance, the nuclear laminae compose a network of intermediate filaments along the inner nuclear envelope that are important for nuclear integrity and serve as a scaffold for chromatin and other proteins, though such filaments are absent in yeast (**Fig 1.1B**) (D'Angelo and Hetzer, 2006).

The nuclear envelope is punctuated by large macromolecular complexes known as nuclear pore complexes (NPC), which facilitate the regulated transport of various macromolecules between the nucleus and cytoplasm. Roughly 120 MDa in vertebrates, the NPC is composed of ~30 proteins, known as nucleoporins that interact to form subcomplexes within the NPC, resulting in an eight-fold symmetry around a central pore (**Fig 1.1C**) (Lim and Farhenkrog, 2006). Acting as a selective barrier between the nucleus and cytoplasm, proteins larger then 30-40 kDa can passage through the pore only when they are bound as cargo to transport receptors (Weis, 2007). Signal sequences, a nuclear localization sequence (NLS's) for import and nuclear export sequences (NES's) for export, confer specific transport receptor binding to cargo protein. Barrier formation within the pore is believed to be mediated via a meshwork of FG repeats from multiple nucleoporins which is then "dissolved" by transport receptors (**Fig 1.1D**) (Frey et al., 2007). However, the exact composition and properties of the

Figure 1.1

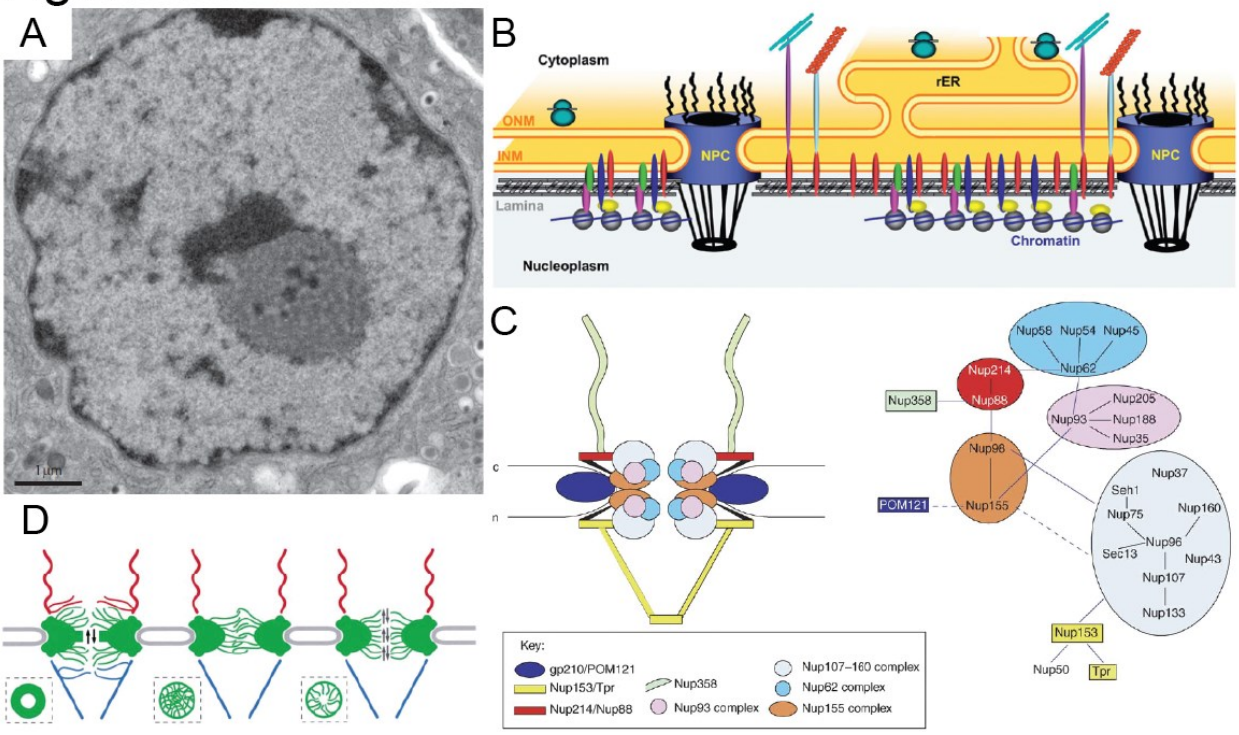

Figure 1.1: The Nucleus.
A. Electron micrograph of a mammalian liver nucleus showing dark-staining heterochromatin along the nuclear envelope (Akhtar and Gasser, 2007).
B. Depiction of the nuclear envelope including the contiguous endoplasmic reticulum, outer and inner nuclear membranes, nuclear pores, lamina, and chromatin (D'Angelo and Hetzer, 2006).
C. The various subcomplexes of the nuclear pore complex (Lim and Fahrenkrog, 2006).
D. Selectivity models of the nuclear pore complex. From left to right: Brownian affinity gate model; selective phase model; "oily-spaghetti" model (Weis, 2003).

meshwork have yet to be elucidated. Despite a high level of stringency, the NPC is still able to transport massive amounts of cargo within a short period of time (Weis, 2003). Given the selective permeability of the nuclear pore complex, on its whole, the nucleus not only safeguards the genome, but functions to regulate gene expression by uncoupling transcription from translation and facilitating precise temporal interactions with the genome (Fernandez-Martinez and Rout, 2009). Thus, the compartmentalization of the genome in the nucleus serves as the most fundamental form of genome organization in eukaryotes.

Chromatin

Within the eukaryotic nucleus, genomic DNA associates with a variety of proteins to form the dynamic polymer known as chromatin (Felsenfeld and Groudine, 2003; Jenuwein and Allis, 2001). Histones comprise the chief protein component of chromatin and form regular units of nucleosomes which consist of 146bp of DNA wrapped around an octamer of the core histones H2A, H2B, H3, and H4. The regulator pattern of DNA-wound-nucleosomes gives rise to the 10-nm chromatin fiber/beads-on-a-string configuration and roughly 7-fold compaction of otherwise naked DNA (Wegel and Shaw, 2005). In turn, the polynucleosome arrays are folded to produce the 30-nm fiber that represents a 50-fold net compaction of the genome (**Fig 1.2A**) (Felsenfeld and Groudine, 2003). Higher level or tertiary chromatin structures subsequently provide additional condensation and emerge through long-distance interactions of the 30-nm fiber, perhaps through the folding of thin fibers into thicker ones or the radial looping of the 30-nm fiber along a protein scaffold (**Fig 1.2B**) (Wegel and Shaw, 2005); however, the actual tertiary structure remains elusive (Adkins et al., 2004).

Importantly, the higher-order structures of chromatin, as well as the components that give rise to its organization, play a fundamental role in the regulation of gene expression. Highly condensed regions of the genome, known as heterochromatin, contain few active genes. Instead, heterochromatin encompasses transcriptionally repressed sequences, the silencing of which is thought to be facilitated, in part, through highly structured nucleosome arrays that prevent access to both nucleases and transcriptional activators (Wegel and Shaw, 2005). Euchromatin, conversely, is largely decondensed and contains a comparatively large number of genes poised for transcription.

Nucleosomes, the core structural unit of chromatin, also directly function in the strict regulation of gene expression as well as other essential biological processes. For instance, ATP-dependent chromatin-remodeling complexes, such as the SWI/SNF family of chromatin-remodelers, control access to underlying genomic sequences by coupling the hydrolysis of ATP with the physical repositioning of nucleosomes (**Fig 1.2C**) (Tang et al., 2010). Additionally, the flexible N-terminal domains of histones, known as histone tails, provide a platform for considerable and integrative posttranslational modification. Covalent modifications of specific residues, including (de)acetylation, methylation, phosphorylation, and ubiquitylation, alter the structure of the nucleosome arrays and affect the electrostatic interactions between DNA and histones, thereby relaxing or stiffening the chromatin structure (Felsenfeld and Groudine, 2003). Histone tail-modifications also recruit additional chromatin-associated

Figure 1.2

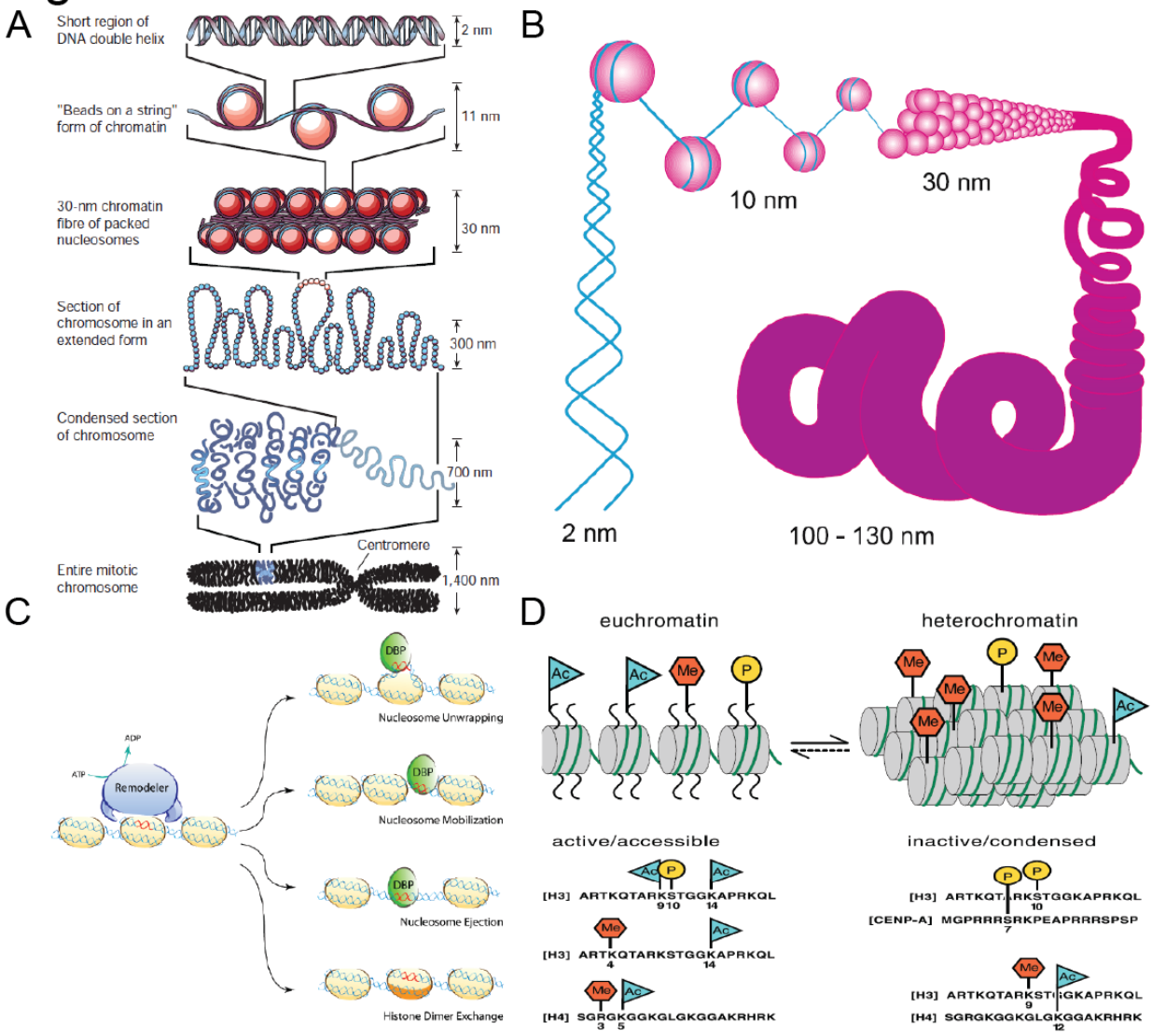

Figure 1.2: Chromatin.
A. Compaction of the genome from the double helix to nucleosomes to chromosomes (Felsenfeld and Groudine, 2003).
B. Different angle of chromatin compaction showing folding of the nucleosome array (Wegel and Shaw, 2005).
C. Various ATP dependent chromatin remodeling activities. Top to bottom: Nucleosome unwrapping; Nucleosome mobilization; Nucleosome ejection; Histone dimer exchange (Tang et al., 2010).
D. Proposed model of the "histone code". Euchromatin and heterochromatin are differentiated by particular post-translational modifications of histone tails, leading to different extents of compaction (Adapted from Jenuwein and Allis, 2001).

proteins containing specific binding domains, such as bromodomains or chromodomains, in a combinatorial manner. In doing so, the covalent modifications of histone tails establish a "histone code" that serves as a mechanism of transcriptional regulation (**Fig 1.2D**) (Jenuwein and Allis, 2001). Typically, euchromatin is characterized by the hyerperacetylation of histones, whereas heterochromatin is marked by hypoacetylation and methylation (Wegel and Shaw, 2005). Finally, the exchange of core histones with conserved variants also confers distinct biological properties to specific nucleosomes. H2A.Z, a universally conserved histone variant of the core histone H2A protein, acts as a boundary element that prevents the spread of silent heterochromatin into transcriptionally active euchromatin (Meneghini et al., 2003) and is found at highly-regulated promoters in yeast (Halley et al., 2010). CENP-A, on the other hand, is a variant of the core histone H3 and establishes centromeres in vertebrates (Felsenfeld and Groudine, 2003). Therefore, the principal components of genome organization play fundamental roles in the regulation of gene expression both dependent and independent of the higher-order structures they establish.

The Organization of Chromosomes and Distinct Chromatin Domains

Chromatin is non-randomly positioned within the nucleus and arranges into a higher-order configuration which supplements more traditional mechanisms of transcriptional regulation. Evidenced first in early cytological studies, heterochromatic regions of the genome localize predominately to the nuclear envelope while euchromatin is more internal (Fraser and Bickmore, 2007). As well, chromosomes are radially arranged in a manner that correlates with gene density - gene poor chromosomes are found along the nuclear periphery whereas gene rich chromosomes are located in the interior of the nucleus (Bolzer et al., 2005; Cremer and Cremer, 2010). Chromosomes, therefore, adopt unique relative positions known as chromosome territories in eukaryotes (**Fig 1.3A**) (Cremer and Cremer, 2010; Duan et al., 2010). Consequently, the genome is arranged into spatially and functionally distinct chromatin domains, further evidenced by the demarcation of rDNA into the discrete nucleolus (Karpen et al., 1988; Duan et al., 2010).

Although techniques such as 3D FISH and analogous chromosome painting methods solidified chromosome territories as a unique higher-order arrangement of chromatin, limitations imposed by the same approaches impede the interrogation of both specific and long-range interchromosomal and intrachromosomal interactions (Bolzer et al., 2005; Cremer and Cremer, 2010). The development of chromatin conformation capture, however, has not only surmounted these challenges but facilitated computational modeling of the genome-wide chromatin interaction matrix (Dekker et al., 2002; Lieberman-Aiden et al., 2009). Importantly, chromatin conformation capture reveals the spatial positioning of genomic sites by determining the relative frequency of physical interactions through: 1) formaldehyde cross-linking, 2) restriction enzyme digestion, 3) intra/intermolecular ligation, and 4) detection of the ligation product by means of paired-end sequencing or specific PCR primers (**Fig 1.3B**) (Dekker et al., 2002; Lieberman-Aiden et al., 2009). When applied genome-wide, Hi-C validates both chromosome territories and the existence of spatially distinct open and closed chromatin domains, as gene-rich chromosomes interact more with one another

Figure 1.3

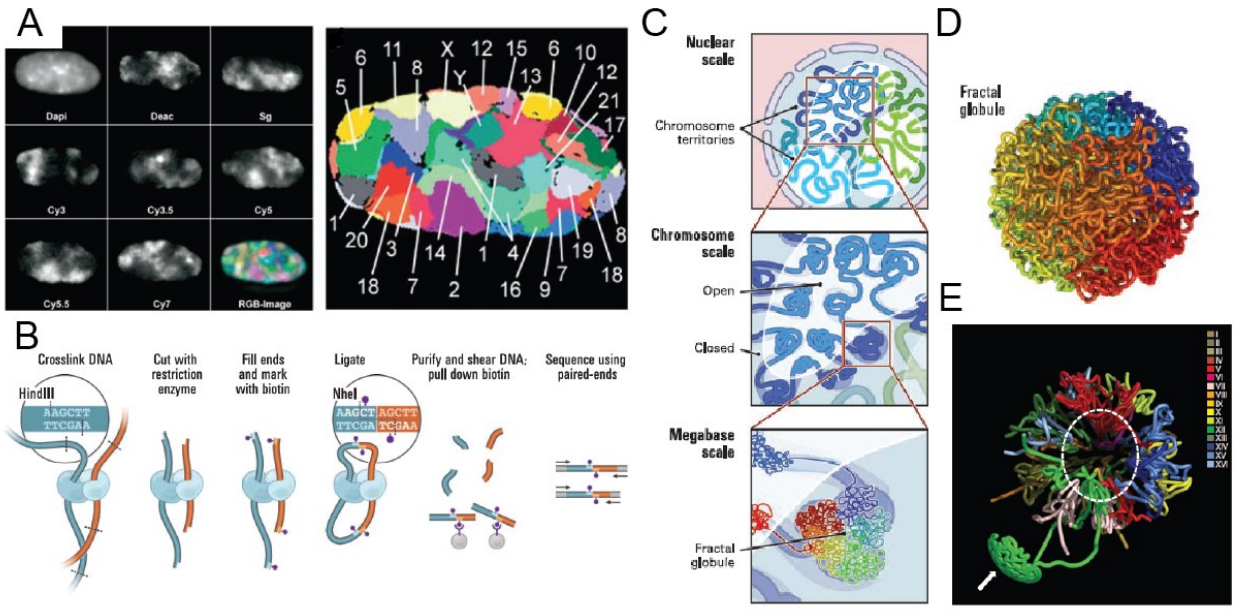

Figure 1.3: Chromosome Territories and Chromatin Conformation Capture.
A. Chromosome territories in human fibroblast nuclei obtained from 3D FISH (Bolzer et al., 2005).
B. Schematic of chromatin conformation capture applied genome-wide (Hi-C) through sequencing (Lierberman-Aiden et al., 2009).
C. Architecture of the human genome from the nuclear scale to the megabase scale obtained from computational modeling derived from Hi-C data (Lierberman-Aiden et al., 2009).
D. Close-up of the fractal globule model at the megabase scale of the genome (Lierberman-Aiden et al., 2009).
E. Three-Dimensional model of the yeast genome showing the demarcation of the nucleolus from the rest of the genome (white arrow) (Duan et al., 2010).

than with gene-poor chromosomes (**Fig 1.3C**). Overall, however, intrachromosomal contacts are enriched over interchromosomal. Interestingly, intrachromosomal interaction profiles are also consistent with discrete chromatin compartments as the observed interactions between intrachromosomal loci do not always correlate with linear distance. This suggests that even adjacent chromosomal loci are capable of accessing spatially and functionally distinct chromatin compartments. Genome-wide interactions profiles also indicate that, on the megabase scale, the genome folds into a fractal globule, a non-equilibrium conformation that permits sequential folding/unfolding of genomic loci and lacks knots (**Fig 1.3D & E**) (Lieberman-Aiden et al., 2009).

Transcriptional Regulation through Looping and Compartmentalization in Metazoans

Notably, consistent with Hi-C data, individual genes are not constitutively retained within a chromosome territory but, rather, escape their corresponding boundaries and are positioned correlative with transcriptional activity into distinct subnuclear domains. The dominant allele of the *brown* gene (bw^D) in *Drosophila*, for instance, inactivates a wild type copy of the allele positioned on a homologous chromosome by stochastically prompting its association with centromeric heterochromatin, demonstrating both long-range chromosomal interactions and position-dependent silencing of gene loci (Dernburg et a., 1996). In agreement, the transcriptional repressor Ikaros is thought to recruit genes to heterochromatic domains to fortify their repression (Fisher and Merkenschlager, 2002). Transcriptionally silent regions of the *Drosophila* genome are also associated with nuclear lamina, consistent with the nuclear periphery functioning as a domain of transcriptional repression (Pickersgill et al., 2006). Similarly, in mammalian cells, the recruitment of genes to nuclear lamina is also sufficient to induce transcriptional repression (Reddy et al., 2008) and the repositioning of Immunoglobulin loci away from the nuclear periphery correlates with transcriptional activation during B lymphocyte development (Kosak et al., 2002).

Thus, the repositioning of specific genes functions not only in gene silencing, but also during transcriptional activation. Consistent with this, Francastel and colleagues demonstrated that a transcriptional enhancer suppresses silencing of a transgene by precluding its association with heterochromatin and, thereby, maintaining it in a subnuclear domain which favors transcription (Fancastel et al., 1999). The locus control region (LCR) contained within a 200kb region encompassing the murine β-globin locus also establishes an open chromatin domain for transcriptional activation by enabling interactions between active globin genes while simultaneously looping-out inactive ones (**Fig 1.4A**) (Tolhuis et al., 2002). This is accompanied by repositioning of the β-globin locus away from the nuclear periphery, although transcription is first initiated at the nuclear envelope (Ragoczy et al., 2006). Moreover, in a model congruent with gene looping, megabase-scale decondensed chromatin loops containing either the MHC or the *HOX* gene cluster expand away from their respective chromosome territories when transcribed (Volpi et al., 2000; Chambeyron and Bickmore, 2004; Mahy et al., 2002). The repositioning of genes away from their chromosome territories may, therefore, facilitate the spatial and specific regulation of gene expression by sequestering genes and their regulators into specific subnuclear domains (Fraser and Bickmore, 2007).

Figure 1.4

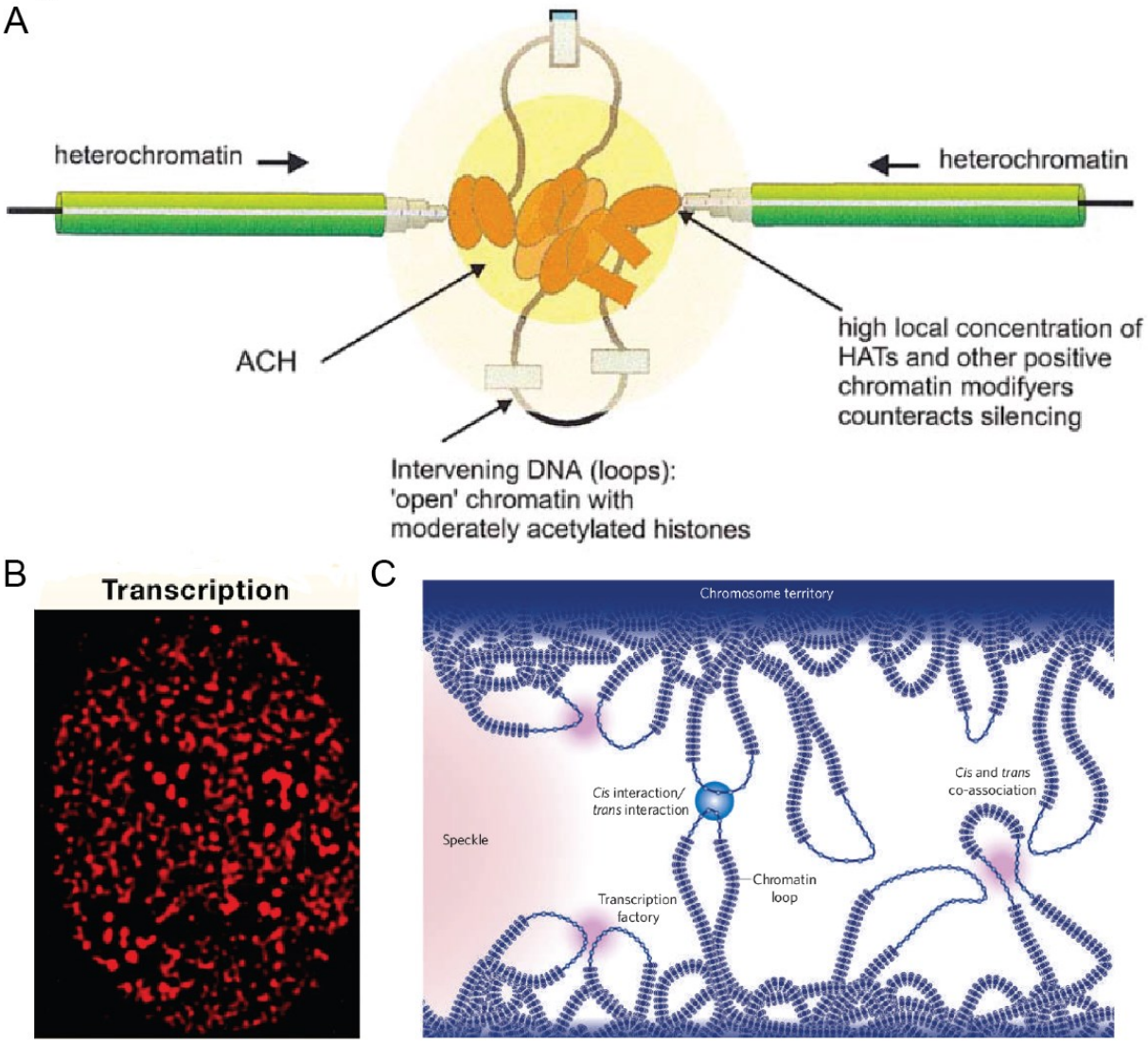

Figure 1.4: Gene Looping and Transcription Factories.
A. Model of the Active Chromatin Hub exhibiting the looping of active genes away from antagonistic heterochromatin (de Laat and Grosveld, 2003).
B. Transcription foci visualized by bromo-UTP, possibly representing transcription factories (Adapted from Misteli, 2007).
C. Decondensed chromatin loops extending from chromosome territories and colocalizing both *in cis* and *in trans* for expression in transcription factories (pink) and co-regulation (blue) (Fraser and Bickmore, 2007).

An extension of gene looping, the transcription factory model postulates that activated genes are localized to distinct sites within the nucleus where RNA polymerases are concentrated for efficient transcription. Such organization subsequently gives rise to sustained and coordinate gene expression through recruitment of co-regulated genes to specific factories (Sutherland and Bickmore, 2009). Evidence for the transcription factory model includes microscopy-based observations of large (200-500nm) RNA Pol I foci within the nucleolus as well as discrete (45-100nm) RNA Pol II foci in the remaining nucleoplasm (**Fig 1.4B**) (Sutherland and Bickmore, 2009; Misteli, 2007). Furthermore, although the mechanism of nucleation remains unclear, once transcription factories are established, RNA Pol II molecules recycle within the distinct compartments localized around activated-*HSP70* loci in *Drosophila* (Yao et al., 2007). Triple-label DNA immuno-FISH experiments additionally indicate that actively transcribed genes associate with the same RNA Pol II transcription factories at high frequencies, while inactive genes do not (Osborne et al., 2004). Finally, oestrogen receptor α binding in the human genome induces long-range chromatin interactions, facilitated through extensive intrachromosomal looping and concurrent with synchronized transcriptional activation (**Fig 1.4C**) (Fullwood et al., 2009). This is also consistent with observations in yeast, indicating an evolutionary conservation of transcription-dependent colocalization of co-regulated genes and suggestive of a central function in gene regulation (Brickner et al., 2012). However, the mechanism of formation, biological function, and even the existence of transcription factories are still widely contested (Sutherland and Bickmore, 2009).

Chromatin Mobility

Quantifying Chromatin Mobility

Despite a defined hierarchal organization of the eukaryotic genome, phenomena such as gene looping and transcription factories clearly reveal a non-static architecture, particularly in the temporal repositioning of specific genes. Indeed, chromatin mobility and the successive variations in the spatial arrangement of genes and chromosomes is fundamental to a variety of essential biological processes, including homolog pairing during meiosis, enhancer-promoter interactions, recombination, and double-strand break repair (Marshall et al., 1997; Neumann et al., 2012). Accordingly, the mechanism(s) by which chromatin repositions within the nucleus has been explored extensively, with advancements in technology now allowing researchers to directly monitor the movements of chromatin in real-time rather than relying on static images produced through fixation-dependent techniques such as fluorescent in situ hybridization (FISH). Moreover, because modern methods do not require fixation, the mobility of chromatin can be scrutinized throughout distinct cellular perturbations and followed over time. Such methods therefore allow for direct analysis and quantification of chromatin motion.

In brief, the approach predominantly employed to investigate the mechanisms of chromatin mobility entails integrating long stretches of heterologous repeats (*lacO*; *tetO)*, containing binding sites for DNA-binding proteins, near a gene or chromosomal locus of interest (**Fig 1.5A & B**). Concurrent expression of a fusion protein

Figure 1.5

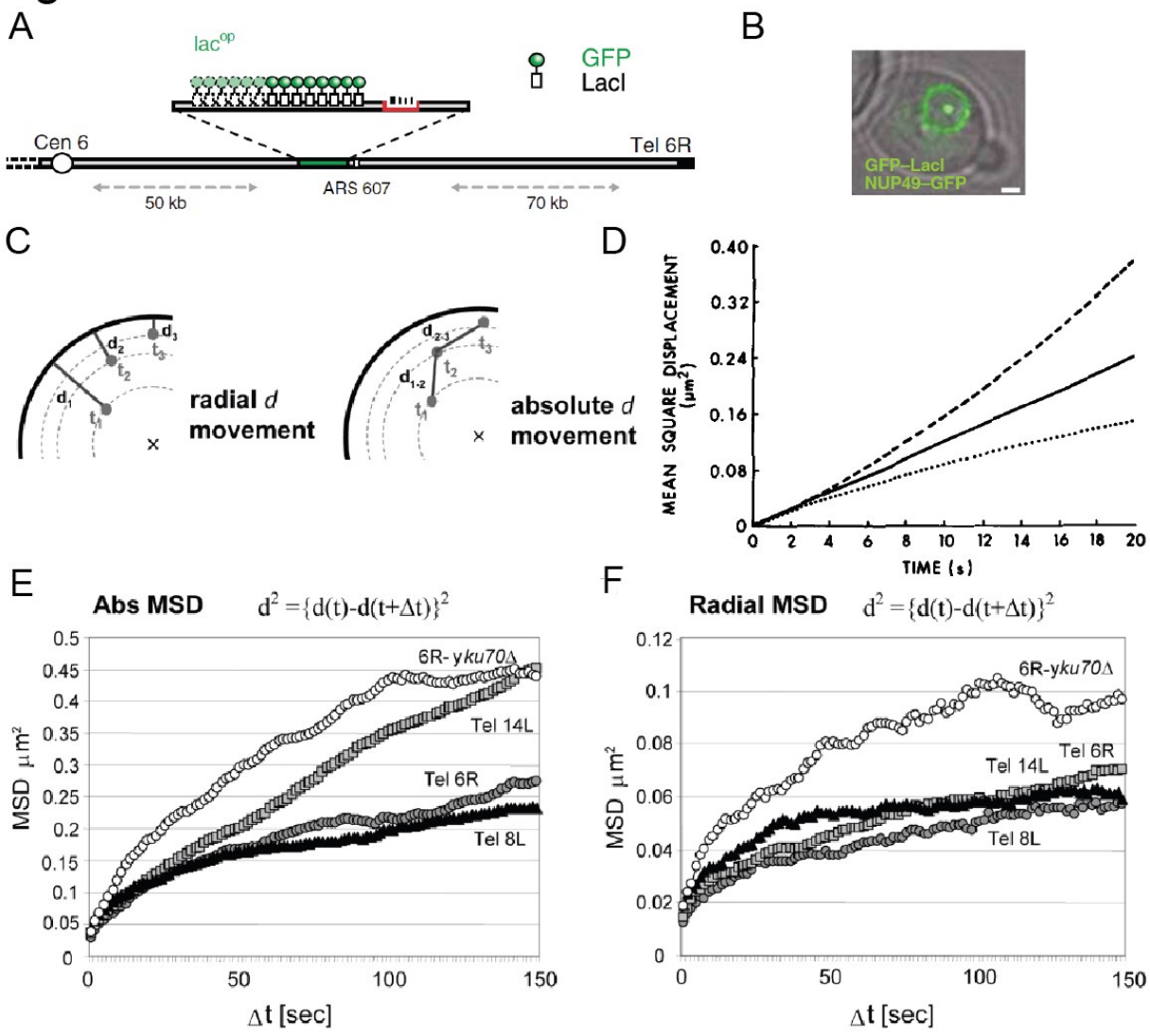

Figure 1.5: Quantifying Chromatin Mobility.
A. Schematic describing the widely-utilized method for visualizing and tracking chromatin loci by integrating repetitive sequences (*lacO*) and co-expressing the corresponding DNA binding protein fused to GFP (LacI-GFP) (Adapted from Taddei et al, 2004).
B. Visualization of chromatin *in vivo* as a result of labeling in A (Taddei et al, 2004).
C. Tracking the displacement of a chromosomal locus in reference to the nuclear envelope (radial displacement) versus absolute displacement (Sage et al., 2005).
D. Simulated Mean Square Displacements. Solid line= Ideal diffusion; Dashed line= Diffusion with flow; Dotted line= Corralled or constrained diffusion (Qian et al., 1991).
E. Radial and Absolute MSDs of different telomeres in yeast exhibiting corralled diffusion (Adapted from Sage et al., 2005).

containing the corresponding DNA-binding domain fused to a fluorescent reporter then allows for visualization and sequential, time-lapse imaging of the chromatin-site *in vivo* (Marshall et al., 1997; Heun et al., 2001). Combinatorial integrations of repeat/fluorescent-reporters additionally permit the direct, simultaneous examination of multiple and distinct loci. Once time-lapsed images are collected, single particle analysis tracks the position of the chromosomal-site(s) in each consecutive frame and computes the chronological displacement of the particle (Qian et al., 1991). Importantly, the displacement of the particle can be calculated as a function of the distance from its origin, the distance from a reference point, or the distance between two (or more) moving particles (**Fig 1.5C**) (Sage et al., 2005).

The displacements for a given trajectory are then compiled into a Mean Squared Displacement (MSD), based on the equation:

$$MSD\tau = \langle \left(r_{(t+\tau)} - r_t\right)^2 \rangle$$

(Qian et al., 1991). MSD's reveal important quantitative characteristics of motion hypothesized to be diffusive and, thus, stochastic (Qian et al., 1991). The slope of the MSD varies dependent on the nature of the diffusive motion and therefore depicts more than just the magnitude of the diffusive movement. For instance, a positive curvature to the slope suggests diffusion with flow, perhaps due to the activity of directed motion consistent with active transport. Conversely, a negative curvature implies sub-diffusion, also known as "corralled" diffusion or diffusion within a cage, and may arise from interactions with other particles or biological barriers. Both a positive and negative MSD slope is considered anomalous diffusion, whereas a linear slope represents true or ideal diffusive motion (**Fig 1.5D**). Regardless of the shape of the curve, however, diffusion coefficients can be calculated from the initial slope of the MSD as the rate of diffusion is not affected by anomalous behaviors at sufficiently early time points (Qian et al., 1991). The MSD therefore represents a convenient method to quantify chromatin mobility, as well as the effects of specific perturbations on its motion (**Fig 1.5E & F**).

The Diffusive Characteristics and Mechanisms of Chromatin Mobility

From bacteria to eukaryotes, the mobility of chromosomal loci is best described as a constrained random walk consistent with anomalous sub-diffusion and characterized by "wiggling" in place (Marshall et al., 1997; Heun et al., 2001; Weber et al., 2012). Importantly, the constraints imparted on the diffusion of interphase chromosomes are largely independent of barriers presented by biological membranes, such as the nuclear envelope, but instead likely due to crowding and polymer entanglement (Marshall et al., 1997). Nevertheless, anchoring chromatin along the nuclear periphery also confines its motion (**Fig 1.6A**) (Heun et al., 2001; Chubb et al., 2002; Cabal et al., 2006).

Notably, the mechanisms that propel the diffusion and "wiggling" of chromosomal loci are widely hypothesized to be ATP-dependent (Akhtar and Gasser, 2007). In accordance with this hypothesis, perturbations to dynamic components of the cytoskeleton also confine chromatin mobility. For instance, treatment of yeast cells with nocodazole, a microtubule depolymerizer, reduces the frequency of large chromatin

Figure 1.6

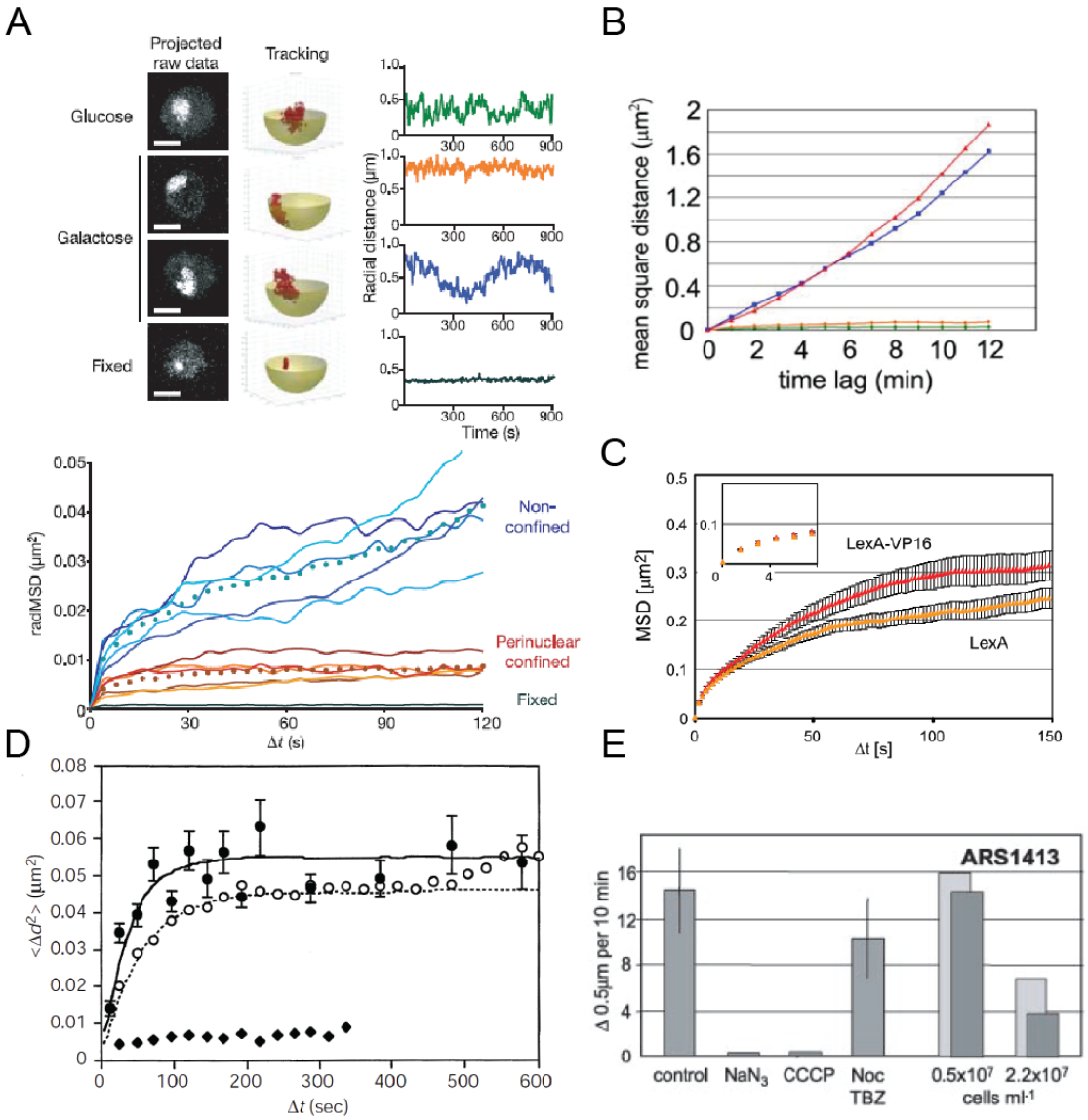

Figure 1.6: Characteristics and Potential Mechanisms of Chromatin Mobility.
A. Mobility of the *GAL* locus when confined at the nuclear periphery versus centrally localized (Cabal et al., 2006).
B. Average MSD's of long-range, curvilinear trajectories of chromatin loci in rat glial cells consistent with diffusion with flow and/or directed motion (red and blue lines) (Chuang et al., 2006).
C. Ectopic targeting of the VP16 activation-domain, via the DNA binding-domain of LexA, increases the mobility of a transcriptionally active chromosomal locus in yeast (Neumann et al., 2012).
D & E. Contrast of analogous experiments exhibiting startlingly different results. Left, sodium azide has only minor effects on the mobility of a chromosomal locus (open circles) (Marshall et al., 1997); versus right, sodium azide (NaN_3) ablates long-distance movements of a chromosomal locus (Heun et al., 2001).

movements (Heun et al., 2001). Specific actin and myosin I mutants also disrupt the long-range directional movements of chromosomal loci in C6 rat glial cells (**Fig 1.6B**) (Chuang et al., 2006). Moreover, in further concurrence with cytoskeleton-driven mobility, the dramatic movement of meiotic chromosomes is known to be propelled by microtubules in *S. pombe* and actin cables in *S. cerevisiae* (Hiraoka and Dernburg, 2009; Conrad et al., 2008; Koszul et al., 2008). In both cases, the transduction of force is conferred through the nuclear envelope (Koszul et al., 2008). Even in the absence of such directed force, however, the actin cytoskeleton may yet influence the mobility of interphase chromatin as it is has been shown to form dynamic filaments within the nucleus and influence the diffusion of large macromolecules (Baarlink et al., 2013; Zhou et al., 2011).

Alternatively, independent of the cytoskeleton, the "wiggling" of chromosomal loci may be driven by the ATP-dependent processes that occur along the length of the chromosome, including nucleosome remodeling, transcription, and replication (Neumann et al., 2012; Weber et al., 2012; Zidovska et al., 2013). Consistent with this, the ectopic targeting of a transcriptional activator (VP16) or chromatin remodeler (INO80) to a particular locus increases its mobility and suggests that such activity can enhance the local flexibility and movement of chromatin (**Fig 1.6C**) (Neumann et al., 2012). As well, inhibition of RNA polymerase activity with rifampin treatment decreases the movement of chromosomal loci in bacteria, which has been interpreted to result from a decrease in ATP-dependent activity (Weber et al., 2012).

It is worth noting, however, regardless of the described evidence, that analogous experiments exploring the central ATP-dependence of chromatin mobility arrived at astonishingly different conclusions. Treatment of cells with sodium azide (NaN_3), an inhibitor of oxidative phosphorylation, only slightly reduced mobility of a chromosomal locus in one treatment (**Fig 1.6D**) (Marshall et al., 1997), but, conversely, substantially reduced mobility and the frequency of large chromosomal movements in others (**Fig 1.6E**) (Weber et al., 2012; Heun et al., 2001). In theory, all azide treatments poison cellular metabolism and subsequently deplete ATP, thus the actual mechanism of confinement induced by the identical treatments remains unknown. Moreover, inhibitors of oxidative phosphorylation induce pleiotropic effects within the cell, including a startling reduction of intracellular pH and depolymerization of the actin cytoskeleton, which could also influence the diffusion of chromatin independently of ATP (Peters et al., 2013). Therefore, given the conflicting results of analogous experiments, as well as the confounding pleiotropic effects of the methods employed, the true mechanism(s) of chromatin mobility is yet to be defined and may emerge from a combination of many distinct processes.

Gene Positioning and the Regulation of Gene Expression in Budding Yeast

The Nuclear Periphery Functions as a Domain of Transcriptional Repression

Like metazoans, the heterochromatic regions of the yeast genome, including telomeres and the silent mating-type loci, are found predominately at the nuclear periphery, suggesting a conserved role of the inner nuclear envelope in gene silencing (Gotta et al., 1996). In agreement, the Silent Information Regulator (Sir) proteins,

essential for the silencing of yeast heterochromatin, are localized at the nuclear periphery though multiple mechanisms. Esc1, a nuclear envelope associated protein, binds directly to Sir4 and is necessary for the Sir4-based anchoring and segregation of a plasmid (Andrulis et al., 2002). Similarly, the yKu70/80 complex binds and recruits Sir4 to the nuclear periphery, although its anchor at the NE is only known to be Msp3 during S-phase (Roy et al., 2004; Schober et al., 2009). As a result of Sir4's interactions with proteins localized to the NE, a fusion protein containing a 312 amino acid fragment of Sir4 is sufficient to reposition an inner-chromosomal locus to the nuclear periphery (Taddei et al., 2004). Therefore, by anchoring the Sir proteins, the nuclear envelope of budding yeast functions as a silencing domain sufficient to anchor chromatin at the nuclear envelope.

Consistent with the idea that the nuclear periphery demarcates a zone of transcriptional repression, in 1998 Andrulis et al. provided key evidence that the positioning of a gene at the nuclear periphery actively functions in its silencing, rather than simply localizing there due to the presence of heterochromatin. To do so, the researchers first constructed an *HMR* locus with a defective silencer. Normally, the mating type loci of budding yeast, including *HMR*, are actively repressed through *cis*-acting factors, known as silencers, and *trans*-acting factors, including ORC, RAP1, and ABF1, which initiate the cooperative binding of the Silent Information Regulator (Sir) proteins (Rusche et al., 2003; Andrulis et al., 1998). The defective silencer, however, contained multiple elements (2/3) replaced with binding sites for the DNA-binding domain of the Gal4 transcription factor. In the absence of additional manipulations, the cryptic silencer remaining on the *HMR* locus was unable to confer sufficient silencing of an adjacent *TRP1* gene (*hmr::TRP1)*. However, upon ectopic localization to the nuclear periphery through co-expression of a fusion protein, silencing was restored to wild-type levels. Importantly, the restoration of silencing was directly dependent on the presence of *SIR2* and *SIR3* and at least one functional element of the normal silencer. The authors therefore concluded that localization at the nuclear periphery plays an important role in the transcriptional silencing of chromatin, though is not sufficient for full repression (Andrulis et al., 1998).

The Silencing of Telomeres at the NE Facilitates the Formation of a Silent Domain

Analogous to the mating type loci, the telomeres of budding yeast are also silenced by means of Sir-mediated repression, through the binding of Rap1 to telomeric repeats (Hediger et al., 2002). As a result of their silencing, the telomere position effect (TPE) results in the repression of RNA Pol II-dependent genes when placed adjacent to telomeres (**Fig 1.7A**). The effect is heritable and follows from the formation of a compact, heterochromatin-like structure that materializes due to the spreading of silent chromatin (Hediger et al., 2002). Importantly, the effect of telomeres on the expression of adjacent genes provides a functional read-out on the efficiency of telomere repression, such that higher expression of a subtelomeric gene should follow from defective silencing.

Using the TPE assay in combination with live imaging of telomeres, Hedinger et al. (2002) identified parallel and redundant pathways of telomere anchoring at the nuclear periphery by associating the localization of telomeres with the efficiency of

Figure 1.7

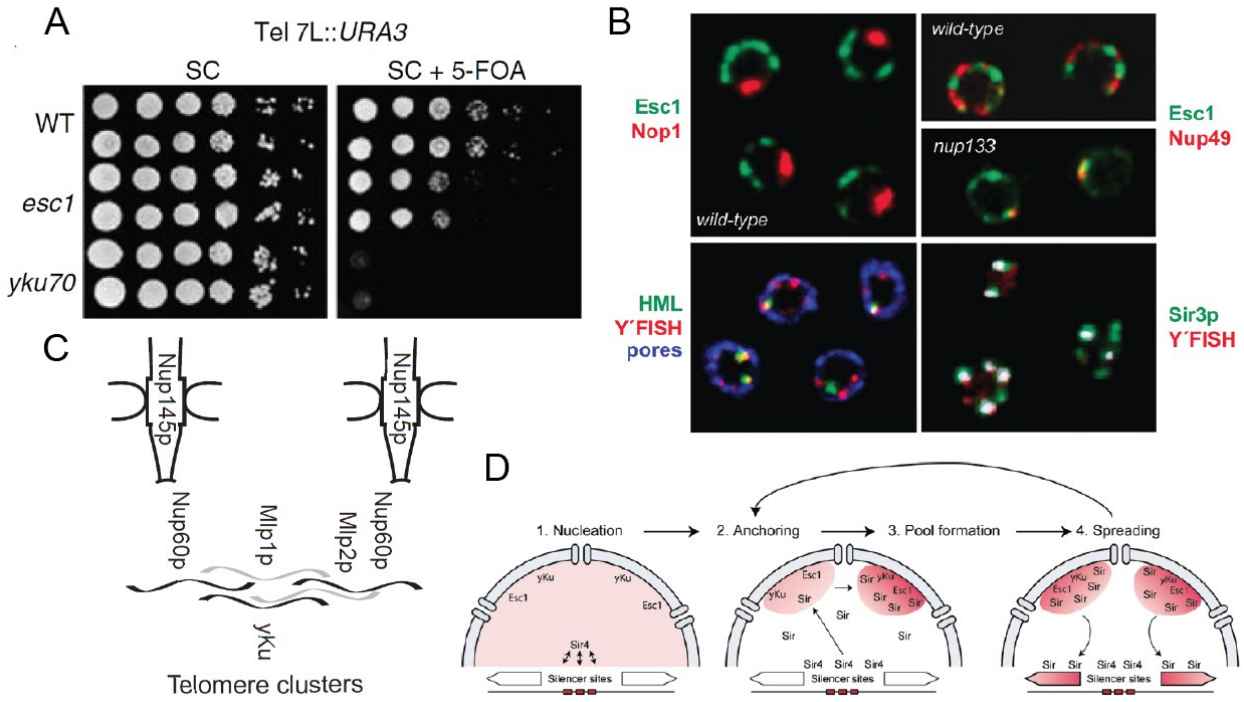

Figure 1.7: Transcriptional Silencing at the Nuclear Periphery of Budding Yeast.
A. Example of the Telomere Position Effect (TPE) inducing the repression of a subtelomeric *URA3* gene; effective silencing results in growth. TPE is reduced in mutants that mislocalize the telomeres (*esc1*Δ and *yku70*Δ) (Taddei et al., 2004).
B. Esc1, an inner nuclear envelope protein which binds Sir4 and anchors telomeres at the nuclear envelope, is positioned distinct from nuclear pores. Telomeres colocalize with the silencing factor Sir3 and also independently of pores (Gasser et al., 2004).
C. Nucleoporins involved in maintaining the architecture and integrity of the silencing domain at the nuclear periphery. Disruption of any of the components in the hierarchal complex results in the release of telomeres from the nuclear periphery (Feuerbach et al., 2002).
D. Model of telomere anchoring in the establishment and maintenance of silencing at the nuclear periphery. Overall, telomere silencing at the nuclear periphery results in a "self-propagating", high-local concentration of the silencing factors at the nuclear periphery (Gasser et al., 2004).

subtelomeric repression. One such mechanism involves the binding of Esc1 to Sir4, and is sufficient to localize telomeres to the nuclear periphery which correlates with subtelomeric repression. The other mechanism can operate independently of silencing through the yKu70/80 complex that is thought to bind telomerase at the ends of chromosomes as well as Sir4 (Schober et al., 2009). Accordingly, Sir-dependent anchoring of telomeres is dependent on the presence of either Esc1 or yKu80 (Hedinger et al. 2002). The anchorage of individual telomeres seems to differ based on their dependence on the parallel pathways and is hypothesized to be due to the proficiency of heterochromatin formation (Gasser et al., 2004). Thus, the anchoring of telomeres at the NE may actively facilitate functional silencing, consistent with a mislocalization-induced reduction of TPE (Hedinger et al. 2002).

Given the colocalization of telomeres, the silent mating type loci, and the Silent Information Regulator proteins at the nuclear periphery, it was hypothesized that silencing is dependent on positioning at the nuclear envelope (**Fig 1.7B**). To test such a model, Gartenberg et al. (2004) conducted a clever study to determine if the peripheral localization of a gene is necessary for its silencing. By inducing site-specific recombination around the *HMR* locus, the researchers liberated the gene from its chromosomal context to exclude confounding effects from a nearby telomere. Independent from the chromosome, the circularized *HMR* locus, nevertheless, localized to the nuclear periphery in a manner dependent on functional silencing, as the Sir proteins necessary for repression of *HMR* are also essential for its localization at the nuclear envelope. Importantly, however, simultaneously releasing the Sir proteins from the nuclear periphery re-establishes silencing within a non-peripheral, excised *HMR* locus. Thus, repression can occur independently of subnuclear context only if the silencing factors are diffuse throughout the nucleus rather than sequestered at the nuclear envelope (Gartenberg et al., 2004).

Collectively, then, the concurrent anchoring of both telomeres and Sir silencing proteins suggest that the nuclear periphery establishes a zone of transcriptional repression through the sequestration of factors essential to transcriptional silencing. In doing so, the nuclear periphery may function to nucleate silencing across distinct regions of heterochromatin, including the telomeres and silent mating type loci, while also preventing aberrant silencing throughout the rest of the genome (Gasser et al., 2004). Given the parallel pathways by which telomeres anchor to the nuclear envelope, Gasser et al. (2004) proposed a model wherein the nucleation of Sir-mediated repression across telomeres induces their positioning at the nuclear periphery, predominantly through SIR4. Subsequently, the clustering of telomeres at the nuclear periphery creates a high local concentration of the Sir proteins, which also reinforces the attachment of telomeres to the NE. In turn, the high concentration of repressors aids in the assembly and spreading of silent heterochromatin. Thus, the anchoring of telomeres creates a “self-propagating” sink of localized silencing factors (**Fig 1.7D**) (Gasser et al., 2004) and consequently establishes a domain of transcriptional repression at the nuclear periphery.

The Role of the Nuclear Pore Complex in the Establishment of Silencing

Although Esc1, Sir4, and telomeric foci all colocalize to positions distinct from nuclear pores, the integrity of the nuclear pore complex plays a key role in the efficient silencing of heterochromatin (**Fig 1.7B**) (Gasser et al., 2004). Double deletions of *MLP1* and *MLP2*, coiled-coil extensions of the nuclear pore complex, disrupt the clustering of telomeres at the nuclear periphery and result in a reduction of subtelomeric silencing of a reporter gene, an effect similar to the deletion of a known telomere anchor *YKU70* (Galy et al., 2000). Consistent with this, a deletion of *NUP60* or the C-terminus of Nup145 (*nup145*Δ*Cter*) also results in the mislocaliztion of telomeres, as both Mlp1 and Mlp2 anchor to the nuclear pore complex through Nup60 and Nup145 (Feurerbach et al., 2002). Disruptions of the elements that compose this hierarchal structure subsequently de-repress a perinuclear reporter construct (*hmr::TRP1*). Furthermore, ectopic silencing of a reporter gene is increased in these strains since the silencing factors are released from the nuclear periphery (**Fig 1.7C**) (Feurerbach et al., 2002). Together, these results strongly suggest that the nuclear pore complex plays a fundamental role in maintaining the structural integrity of silent domains that are critical for transcriptional repression of heterochromatin.

In addition to these results, Van de Vosse et al. (2013) found a fundamental role for the nucleoporin Nup170 in establishing the chromatin structure and subsequent silencing of subtelomeric and ribosomal protein genes. Nup170 is a component of the symmetrical core scaffold of the nuclear pore complex and interacts with chromatin-modifying complexes in *Drosophila* (Mendjan et al., 2006). Similarly in yeast, Nup170 functionally interacts with various chromatin modifying complexes, including SWR-C and Rpd3, through binding of the RSC chromatin remodeling complex component, Sth1. Both the deletion of *NUP170* or depletion of Sth1, results in altered nucleosome positioning and up-regulated expression of subtelomeric and ribosomal protein genes. Furthermore, Nup170 binding is enriched at both subtelomeric and ribosomal protein genes in chromatin immunoprecipitation (ChIP) analysis. This binding is dependent on the presence of Sir4, which mediates the anchoring and functional silencing of subtelomeric genes. Finally, Nup170 establishes the proper localization of Sir4 and it's anchoring of telomeres at the nuclear envelope (Van de Vosse et al., 2013). Thus, Nup170 and the nuclear pore complex play a central role in maintaining the architecture of the repressive domains at the nuclear periphery. This work also further corroborates previous results suggesting that a functional silencing domain at the nuclear periphery enables the efficient silencing of yeast heterochromatin (Andrulis et al., 1998).

Additional Functions of the NPC in Regulating Gene Expression

Contrary to the idea that the nuclear periphery constitutes an exclusively repressive environment, Casolari et al. (2004) presented the first clear evidence that the nuclear pore complex also displays a strong association with transcriptionally active genes in yeast. Nup116, Nup2, Nup60, and Nic96, all components of the nuclear pore complex, were found to bind preferentially to highly expressed genes when analyzed using genome-wide chromatin immunoprecipitation (ChIP). Moreover, the *GAL* genes

Figure 1.8

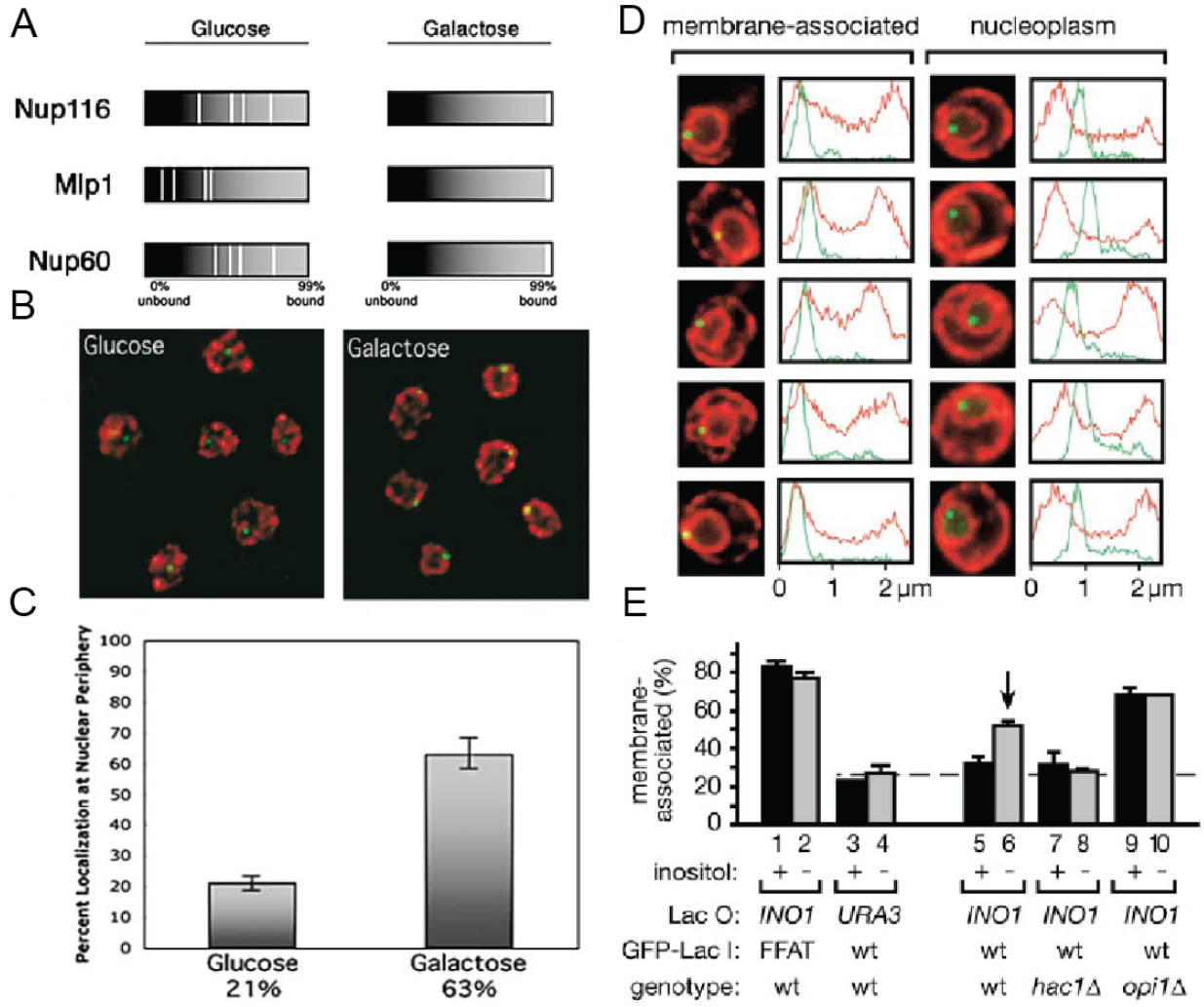

Figure 1.8: The Nuclear Pore Complex Associates with Active Genes.
A. *GAL* genes (white bars) exhibit a striking alteration in the distribution patterns of binding for multiple nucleoporins dependent on their transcriptional status. When repressed in glucose the *GAL* gens are in the lower 75% of binding whereas activation in galactose causes redistribution to the 99th percentile (Adapted from Casolari et al., 2004).
B. The *GAL* locus repositions to the nuclear periphery upon transcriptional activation, consistent with changes in the genome-binding patters of nucleoporins (Casolari et al., 2004).
C. Quantification of *GAL* localization as determined by FISH in B (Casolari et al., 2004).
D. The *INO1* locus localizes to the nuclear envelope upon transcriptional activation in the absence of inositol (Brickner and Walter, 2004).
E. Quantification of D. The repositioning of the *INO1* locus is disrupted in a *hac1*Δ (Brickner and Walter, 2004).

comprised of *GAL1*, *GAL2*, *GAL7*, and *GAL10*, exhibit an increased interaction with several nucleoporins, directly dependent on their transcriptional status. In glucose, the repressed *GAL* genes distribute randomly within the genomic localization profiles of Nup116, Nup60, and Nup100. However, upon a carbon source shift to galactose and subsequent transcriptional activation, all four genes are found to be represented in the 97th percentile of the binding profiles for the same nucleoporins. The data, therefore, strongly suggest that the *GAL* genes preferentially associate with the nuclear pore complex during transcription. Indeed, through fluorescence in-situ hybridization (FISH) of the *GAL* locus, the *GAL* genes were found to co-localize with the nuclear pore complex when transcriptionally active but not when repressed in glucose (**Fig 1.8A**) (Casolari et al. 2004).

Several studies quickly corroborated the findings of Casolari and colleagues in suggesting that the nuclear periphery simultaneously constitutes a zone of transcriptional repression as well as activation. For instance, the *INO1* locus is recruited to the nuclear membrane in activating conditions where the integral membrane protein Scs2 antagonizes the transcriptional repressor Opi1 and thus facilitates transcriptional activation of *INO1* (**Fig 1.8B**) (Brickner and Walter, 2004). In addition, and analogous to the ChIP interactions of nucleoporins with the *GAL* locus, Nup2 interacts with the promoters of highly regulated and expressed genes, dependent on their transcriptional activation (Schmid et al., 2006), again suggestive of an interaction between the nuclear periphery and actively transcribed genes.

Perhaps most compelling in describing a role of the nuclear pore complex in gene activation, in 2005 Menon et al. provided marked evidence for a distinct model of transcriptional activation, termed “reverse recruitment”, in which activators recruit genomic loci to assembled transcriptional machinery at the NPC rather than the transcriptional machinery assembling directly on the DNA. Such a model portends that the nuclear pore complex plays an integral role in the regulation and activation of gene expression, and is somewhat harmonious with the transcription factory model (Sutherland and Bickmore, 2009). Consistent with this, the coactivators of Rap1, Gcr1 and Gcr2, which coordinate cell growth and cell-cycle progression, display synthetic genetic interactions with multiple members of the Nup84 subcomplex of the NPC, indicating a functional connection through a shared or parallel pathway(s). Gcr1 and Gcr2 also coimmunoprecipitate Nup84, Pom34, Pom152, and Kap123, signifying a biochemical association between the distinct cellular machinery. Strikingly, members of the Nup84 subcomplex, firmly anchored within the nuclear pore complex, are correspondingly able to drive the expression of a reporter construct when fused to a DNA-binding domain; notably, however, the expression of the reporter construct is dependent on the presence of Gcr1. Therefore, the nuclear periphery and, in particular, the NPC play a fundamental role in the activation of transcription, converse to its hypothesized function as a zone of transcriptional repression (**Fig 1.9A**). Moreover, this work underscores the value of budding yeast as a model for understanding the complexities of genome organization, as the data are also consistent with oncogenic rearrangements in acute myeloid leukemia that result in the fusion of a DNA-binding domain to the nucleoporin Nup98 (Nup145 in yeast) (Menon et al. 2005).

Figure 1.9

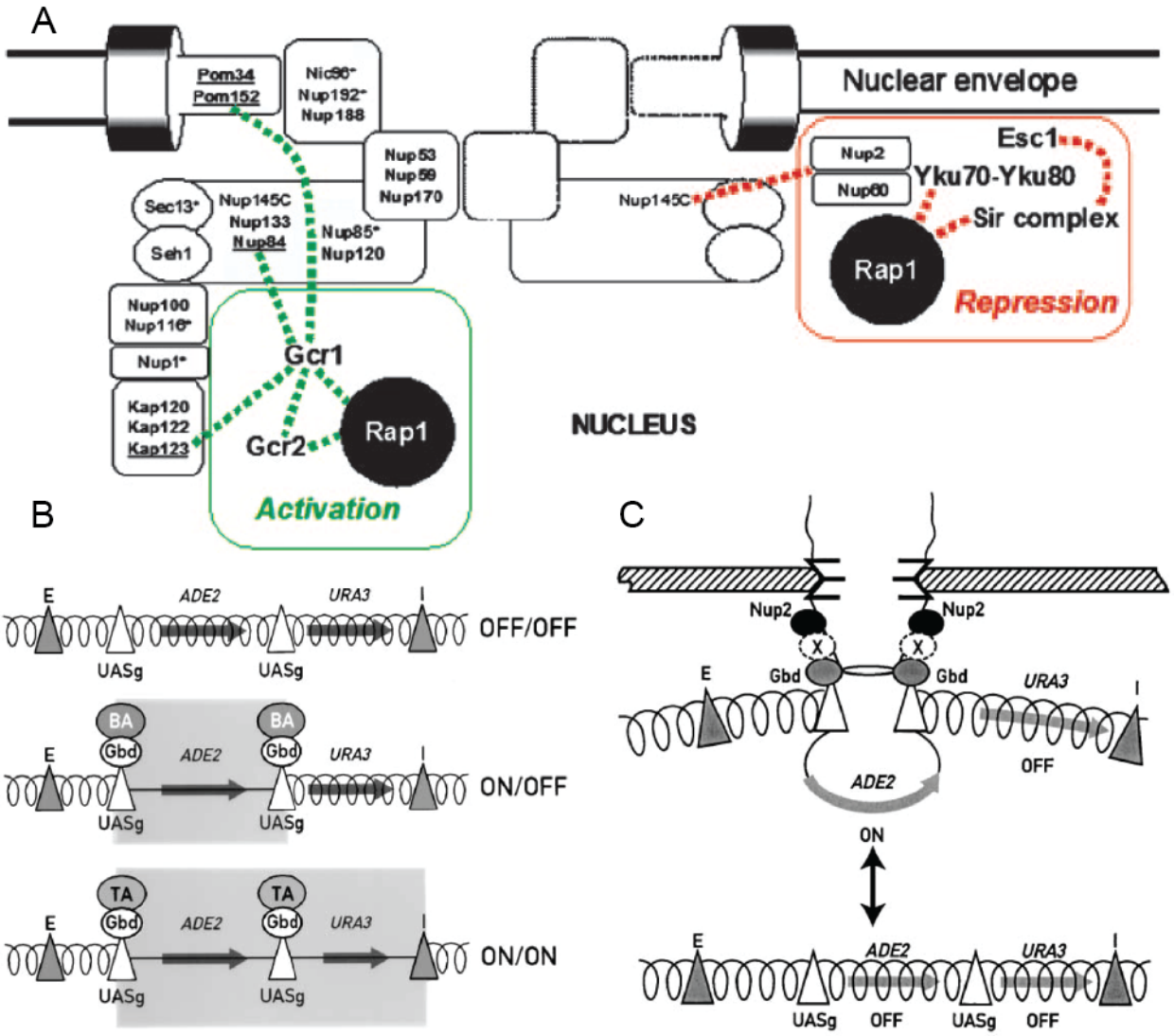

Figure 1.9: Bipartite Functions of the Nuclear Pore Complex.
A. Green: Model of "reverse recruitment", describing the function of the nuclear pore complex in transcriptional activation through the interactions of several nucleoporins with Gcr1 and Gcr2. Red: Involvement of the nuclear pore complex in transcriptional repression through interactions with the yKu70/80 complex (Menon et al., 2005).
B. Schematic of the construct developed to assay boundary activity of various fusion proteins. True boundary activity is depicted in the center cartoon in which the *ADE2* gene is transcriptionally active while the *URA3* gene is transcriptionally repressed (Ishii et al., 2002).
C. Model of how various transportins may induce chromatin boundary activity through interactions and association with Nup2 and the nuclear pore complex (Ishii et al., 2002).

Boundary Activity at the Nuclear Pore Complex

Consistent with a multipartite function of the nuclear pore complex in the simultaneous repression of specific genes and activation of others, the nuclear pore complex also possesses chromatin boundary activity (Ishii et al. 2002). Boundary activity is illustrated when a particular sequence or chromatin structure, a boundary element, partitions the genome such that a gene is protected from the silencing or activation of its neighbors. To demonstrate such a role for the nuclear pore complex, Ishii et al. (2002) developed a "boundary-trap" strain containing reporter genes inserted into the *HML* locus with flanking binding sites for chimeric proteins, similar to the reporter construct used to target a crippled silencer to the nuclear periphery (Andrulis et al., 1998). Normally, both reporter genes are repressed due to heterochromatin formation across the *HML* locus. However, if a chimeric protein capable of boundary activity binds the sites flanking one of the reporter genes, then one of the genes will be activated with the other remaining repressed (**Fig 1.9B**). Notably, many proteins involved in nuclear transport were found to harbor such boundary activity but only in the presence of the nucleoporin Nup2, which is positioned at the inner nuclear basket of the nuclear pore complex. This strongly suggests that the boundary activity of the chimeric proteins is due to the ectopic positioning of the reporter construct to the nuclear pore complex. Indeed, the chimeric proteins sufficient for boundary activity also physically tether the reporter construct to the nuclear pore complex, indicating that the NPC may physically block the spread of heterochromatin to neighboring genes, and, simultaneously, the erroneous activation of others (**Fig 1.9C**) (Ishii et al. 2002). These results substantiate the idea that the NPC and nuclear envelope play multiple roles in the proper spatiotemporal regulation of the genome through the establishment of distinct subnuclear domains.

Gene Gating

Similar to "reverse recruitment", Gunter Blobel proposed the gene gating hypothesis in 1985 as an explanation for the association of nuclear pore complexes with domains of the genome encompassing transcribable genes (Blobel, 1985). The postulation also stems from observations in prokaryotes indicating that the prokaryotic genome is attached to the plasma membrane, suggesting that genome-membrane associations are an evolutionary conserved mechanism of genome regulation, perhaps resulting from primitive gene-capturing mechanisms. Importantly, the gene gating model predicts that the coupling of an active gene with a nuclear pore complex facilitates the prompt and efficient export of transcripts, providing more rapid gene expression and translation within the cytoplasm (Blobel, 1985). Thus, gene gating represents a robust and testable model for describing the functional interactions of nuclear pore complexes with active genes.

Interestingly, in agreement with gene gating, Taddei et al. (2006) described evidence that interactions with the nuclear pore complex confer maximal rates of expression to an inducible yeast gene. *HXK1*, a glucose-repressed gene, repositions to the nuclear periphery, where it colocalizes with nuclear pores, concurrent with its transcriptional induction in non-glucose media (**Fig 1.10A**). The peripheral localization

of the *HXK1* locus can also occur independently of carbon source but only in the absence of the transcriptional repressor, *HXK2*. Association with the nuclear periphery is, however, dependent on the presence of the 3'UTR (three prime untranslated region), suggesting an mRNA-dependent tethering mechanism that can only initiate during ongoing transcription. Importantly, to determine if the transcription-dependent NPC association also confers transcriptional regulation of *HXK1*, the researchers directly manipulated the localization of the gene while simultaneously monitoring transcript expression levels. Strikingly, artificially tethering the *HXK1* locus to the nuclear periphery results in maximal gene expression, implying a functional role of gene positioning in determining expression levels (**Fig 1.10B**) (Taddei et al. 2006). However, although the data and conclusions are consistent with gene gating, many caveats complicate these results. For one, the periphery-dependent maximal expression was driven from a non-native promoter integrated at the *HXK1* locus. Moreover, ectopic localization to the nuclear periphery was facilitated through a domain of Esc1, known to localize independently of nuclear pores (Gasser et al., 2004), thus conflating whether association with the periphery or the NPC is important for optimal gene expression. Finally, protein levels were not analyzed to ensure a strict correlation between transcript and protein abundance to validate functional mRNA production. Therefore, the results of Taddei et al. (2006) support but do not validate gene gating.

Nevertheless, several other lines of inquiry in yeast also substantiate the Blobel model, especially the coupling of transcription with mRNA export at the nuclear pore complex. For instance, the *GAL* locus comprised of *GAL1*, *GAL7*, and *GAL10*, is recruited to the nuclear periphery concurrent with its transcriptional activation and results in the confinement of its dynamic motion along the nuclear envelope (Cabal et al., 2006). Mechanistically, the *GAL* locus is localized to the nuclear periphery through a variety of distinct macromolecular complexes. Deletions of individual nucleoporins, members of the SAGA histone acetyltransferase complex, or components of the TREX2 mRNA export machinery all disrupt the peripheral localization of the *GAL* genes (Cabal et al., 2006; Luthra et al., 2007). Notably, these macromolecular complexes are all involved with *GAL* gene expression from transcription to processing to export as SAGA functions to initiate the activation of *GAL* transcription while the other complexes function in the processing and export of the mRNA (Luthra et al., 2007).

These collective results predict the formation of an activation-dependent supercomplex at the nuclear pore complex, functioning to integrate transcription with mRNA export (Rodríguez-Navarro et al., 2004). Indeed, biochemical evidence indicates that the SAGA complex directly interacts with Mlp1 of the NPC, which also associates with similar regions within *GAL* promoters (Luthra et al., 2007). Additionally, Mex67, the export receptor responsible for shuttling mRNA out of the nucleus, also anchors *GAL10* and *HSP104* to the nuclear periphery and co-transcriptionally associates with the genes independently of RNA (Dieppois et al., 2006). Sus1, moreover, a relatively diminutive protein, couples the activities of SAGA and TREX2 by bonding with both complexes through Sgf73 of SAGA and Sac3/Cdc31 of TREX2 (**Fig 1.10C**) (Wilmes and Guthrie, 2009; Jani et al., 2009). Predictably, then, a deletion of *SUS1* results in the mislocalization of the *GAL* locus (Cabal et al., 2006). Collectively, these results provide significant credence to the model of gene gating and are concomitantly consistent with proposed gene loops that link promoters with terminators as well as with analogous

Figure 1.10

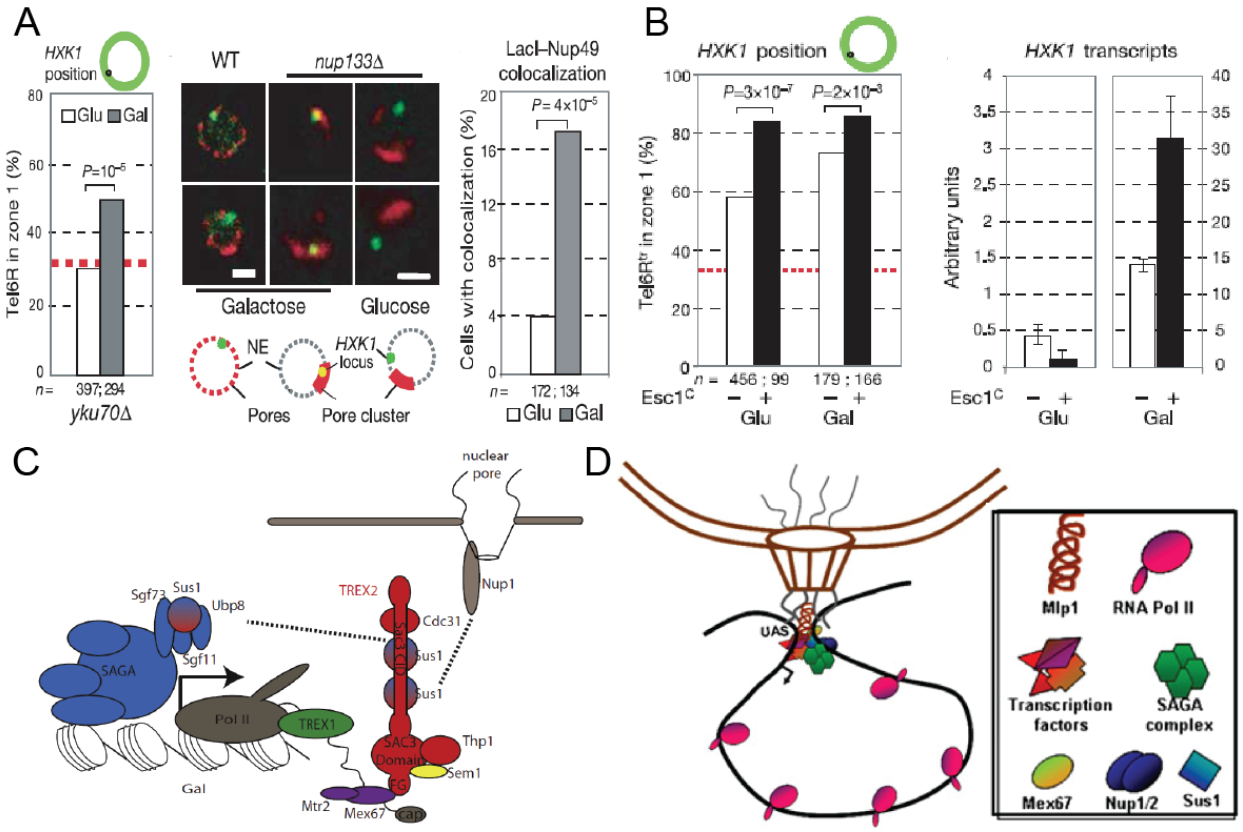

Figure 1.10: Gene Gating.
A. The *HXK1* locus associates with nuclear pore complexes when transcriptionally active in the absence of glucose (Taddei et al., 2007).
B. Ectopic positioning of the *HXK1* locus through a domain of Esc1 confers maximal gene expression, inferred through transcript abundance (Taddei et al., 2007).
C. Model of the supercomplex which couples transcription to mRNA export for SAGA-regulated genes at the nuclear pore complex. Sac3 bridges SAGA and TREX2 through Sus1 (Wilmes and Guthrie, 2009).
D. Proposed gene looping at the nuclear pore complex which may confer optimal gene expression through continued rounds of transcription and coupling of distinct processes (Adapted from Tan-Wong et al., 2009).

results from *Drosophila* (**Fig 1.10D**) (Blobel, 1985; O'sullivan et al., 2004; Tan-Wong et al., 2009; Kurshakova et al., 2007).

However, in addition to conflicting results suggesting that active-gene positioning does not correlate with gene expression (Dieppois et al., 2006; Cabal et al., 2006), gene gating posits that genes are localized to nuclear pore complexes to facilitate expedited mRNA export and gene expression. This implies that the rate limiting step of mRNA export is the diffusion of a processed transcript to the nuclear pore complex. However, this is inconsistent with known rates of mRNP diffusion and export through the NPC (Shav-Tal et al., 2004; Weis, 2003). Moreover, a confirmation of gene gating, demonstrating that the positioning of a gene at an NPC results in more rapid gene expression from transcripts to translation, remains lacking. Such an experiment is necessary before concluding on the validity of the gene gating model (Blobel, 1985).

Future Directions

Clearly, the organization of the eukaryotic genome is expected to perform a fundamental role in the regulation of gene expression. From chromatin compaction to chromosome territories to gene looping, the hallmarks of genome organization are conserved from yeast to man, indicating a central function in directing the cellular adaptations that guide the life cycles of all eukaryotic organisms. Based on experimental evidence described here, through the active demarcation of specific genes into distinct subnuclear domains, the dynamic organization of the genome enables spatiotemporal transcriptional regulation and, in addition, may facilitate both coordinate gene expression and robust boundary activity. However, much remains to be known about how cells mechanistically adopt a particular organization and, in turn, how that organization determines gene expression.

Budding yeast represent an indispensable model organism for unraveling the mechanistic complexities and functions of dynamic gene positioning due to their conserved genomic characteristics and relative experimental-ease. For instance, telomeres and the silent mating type loci, the heterochromatic regions of the yeast genome, are anchored to the nuclear periphery in a manner analogous to the association between the nuclear envelope and heterochromatin in metazoans (**Fig 1.11A**) (Akhtar and Gasser, 2007). Additionally, nuclear pore complex components of budding yeast interact with both transcriptionally repressed and transcriptionally active genes, a bipartite function shared with their homologs in *Drosophila* (Feurerbach et al., 2002; Van de Vosse et al., 2013; Casolari et al. 2004; Mendjan et al., 2006; Capelson et al., 2010). These collective results from various eukaryotes therefore suggest that the function of positioning a gene near or at a nuclear pore complex is gene specific. This is correspondingly evidenced mechanistically in yeast, as genes activated through analogous pathways yet require distinct nucleoporins and components of other complexes for anchoring at the NPC (**Fig 1.11B**) (Ahmed et al., 2010; Dieppois et al., 2006; Cabal et al., 2006). Consideration must therefore be taken before extrapolating the findings for one gene to others and underscores the importance of utilizing yeast to elucidate the true mechanisms and functions of dynamic gene positioning.

Despite considerable advances in our understanding of the organization of the eukaryotic genome, fundamental questions regarding the mechanism and function of its

dynamicity remain. Therefore, in the following dissertation, we utilize the budding yeast *Saccharomyces cerevisiae* to determine the functional consequences of mislocalizing a specific genomic locus. We then explore whether co-regulated genes colocalize during ongoing transcription, hypothesized to result in the coordinated mobility of both loci. Finally, we investigate the mechanism of chromatin mobility by elucidating the determinants of intracellular diffusion.

Figure 1.11

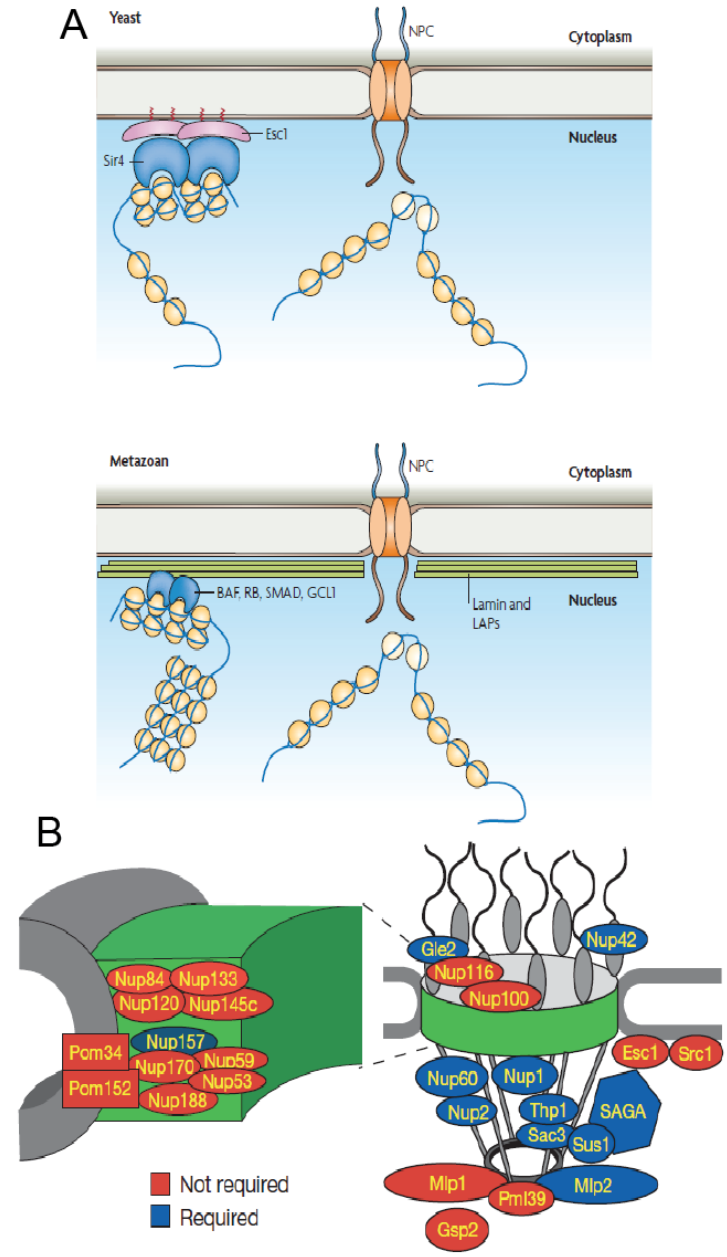

Figure 1.11: The Mechanisms and Functions of Dynamic Gene Positioning.
A. Similarities and differences between the nuclear periphery of yeast and metazoans, which functions in transcriptional repression yet also associates with active genes (Akhtar and Gasser, 2007).
B. Graphical depiction of the nuclear pore complex components involved in the peripheral localization of the activated *INO1* locus (Ahmed et al., 2010). Some components necessary for *INO1* are dispensable for other gene loci (and vice versa), indicating that the mechanism and function of gene positioning may be gene specific.

Chapter 2:

A negative feedback loop at the nuclear periphery regulates *GAL* gene expression

Note: The work presented in the following chapter is reprinted from *Molecular Biology of the Cell*, published by The American Society for Cell Biology:
Green, E. M., Jiang, Y., Joyner, R., and Weis K. (2012). A negative feedback loop at the nuclear periphery regulates GAL gene expression. *Mol. Biol. Cell* **23**, 1367-1375.
To this work, I contributed data and figures and aided in the preparation of the manuscript. I thank and credit the publisher for the right to reprint the material.

Background

The correct spatial organization of the genome within the nucleus is thought to play a critical role in the regulation of gene expression (Fraser and Bickmore, 2007). Genomes are non-randomly arranged and the radial position of a gene within the nucleus can vary correlating with its functional status (Misteli, 2007). The periphery of the nucleus, comprising the nuclear envelope and associated proteins, was originally implicated in transcriptional silencing. In mammalian cells, cytological observations indicate that heterochromatin is localized near the periphery of the nucleus (Taddei *et al.*, 2004). Chromosomes with low gene density, and therefore low transcriptional activity, are often found near the nuclear periphery, whereas chromosomes with high gene density tend to localize to the nuclear interior (Croft *et al.*, 1999). Additionally, a number of genes have been identified that move away from the nuclear periphery upon transcriptional activation, including *IgH* in B lymphocytes (Kosak *et al.*, 2002; Lanctot *et al.*, 2007). Similar to mammalian cells, heterochromatic regions in *Saccharomyces cerevisiae* such as telomeres and silent mating type loci are found at the nuclear periphery (Akhtar and Gasser, 2007) and tethering to the nuclear envelope can be sufficient to repress a crippled silencer (Andrulis *et al.*, 1998). Together, these data have supported the hypothesis that the nuclear periphery is predominantly a site of transcriptional repression. However, more recent evidence has suggested that regulation of gene expression at the nuclear periphery is not limited to repression (Liang and Hetzer, 2011). An investigation of the murine β-globin locus revealed that it localizes to the nuclear periphery during transcriptional activation, and only subsequently relocalizes to the nuclear interior (Ragoczy *et al.*, 2006). Moreover, hypertranscription of the X chromosome in *Drosophila* males occurs at the nuclear periphery and appears to be dependent on components of the nuclear pore complex (NPC) (Mendjan *et al.*, 2006; Vaquerizas *et al.*, 2010), although a direct role of NPC components in this process has been controversial (Grimaud and Becker, 2009). Work in *Drosophila* has also demonstrated a role for some NPC components in transcriptional activation of stress-responsive and developmentally regulated genes (Capelson *et al.*, 2010; Kalverda *et al.*, 2010). Interestingly, this gene activation does not occur at the NPC as the chromatin-Nup interaction occurs away from the nuclear periphery in the nucleoplasm (Capelson *et al.*, 2010; Kalverda *et al.*, 2010; Vaquerizas *et al.*, 2010).

In budding yeast, multiple genomic loci, including genes that respond to carbon source shifts, heat shock, and mating pheromones, move to the nuclear periphery upon transcriptional activation (Brickner and Walter, 2004; Casolari *et al.*, 2004; Casolari *et al.*, 2005; Dieppois *et al.*, 2006; Taddei *et al.*, 2006; Berger *et al.*, 2008). Chromatin near highly transcribed genes associates with members of the NPC and the mRNA export machinery (Casolari *et al.*, 2004). Furthermore, direct physical links have been identified between the NPC and components of the transcriptional machinery, particularly the SAGA complex (Rodriguez-Navarro *et al.*, 2004). In addition, mutations in components of the NPC, the transcriptional regulator SAGA and other chromatin remodeling factors, and the transcription/RNA export complex TREX-2 have been shown to interfere with the association of active genes and the nuclear periphery (Rodriguez-Navarro *et al.*, 2004; Cabal *et al.*, 2006; Dieppois *et al.*, 2006; Drubin *et al.*, 2006; Kohler *et al.*, 2008; Ahmed *et al.*, 2010). In specific cases, the gene-periphery interaction also appears to be

dependent on DNA sequence elements in active gene promoters (Ahmed *et al.*, 2010; Light *et al.*, 2010). In combination, these observations have challenged the tenet that the nuclear periphery demarcates an exclusively repressive zone, particularly within the yeast nucleus, and have led to the suggestion that a zone of transcriptional activity exists at or near nuclear pore complexes (Akhtar and Gasser, 2007; Taddei, 2007). A number of models have been proposed to ascribe functionality to this active gene-nuclear periphery interaction. For example, localization of the *GAL7-10-1* gene cluster at the nuclear periphery has been suggested to be consistent with the gene gating hypothesis, in which active genes are found near nuclear pore complexes to facilitate efficient export of mRNAs from the nucleus (Blobel, 1985; Cabal *et al.*, 2006). Other models suggest that the nuclear periphery: plays a role in chromatin-mediated transcriptional memory at active loci (Brickner *et al.*, 2007), is associated with the formation of gene loops (Laine *et al.*, 2009; Tan-Wong *et al.*, 2009), or recruits genes for activation via localized transcription components (Sarma *et al.*, 2007). Furthermore, there is evidence that genes associate with the nuclear periphery post-transcriptionally (Abruzzi *et al.*, 2006; Vodala *et al.*, 2008) and that the gene-periphery interaction can exist independently of active transcription (Schmid *et al.*, 2006). However, the functional significance of active gene positioning at the nuclear periphery remains unclear.

In this work, we identify the functional role of *GAL* locus movement to the nuclear periphery in budding yeast. We take advantage of mutations that disrupt the gene-periphery interaction to address the significance of the spatial regulation of the *GAL* gene locus. Consistent with a model that the nuclear periphery constitutes a repressive environment, we find that *GAL* gene expression is negatively regulated at the nuclear periphery both upon activation and after repression. Our results suggest that the nuclear position of a gene is important to modulate gene expression, allowing cells to rapidly respond to changes in environmental conditions.

Results

The *GAL* locus is positioned at the nuclear periphery in galactose, raffinose and glycerol

The interaction of the *GAL* locus with the nuclear periphery concomitant with the induction of gene expression has been shown to depend on the function of diverse protein complexes including the nuclear pore complex (NPC) and the transcriptional activation complex SAGA (Casolari *et al.*, 2004; Cabal *et al.*, 2006; Dieppois *et al.*, 2006; Luthra *et al.*, 2007; Kohler *et al.*, 2008; Ahmed *et al.*, 2010). *GAL* genes exist in at least three distinct functional states (Johnston *et al.*, 1994; Santangelo, 2006). When cells are grown in glucose, *GAL* genes are fully repressed. Growth in the presence of other carbon sources, such as the trisaccharide raffinose or non-fermentable glycerol, relieves the glucose-mediated repression but does not induce transcription of the *GAL* genes. By contrast, growth in galactose transcriptionally induces all *GAL* genes (Johnston *et al.*, 1994; Santangelo, 2006). To analyze the dynamic localization of the *GAL* genes in these distinct physiological states, we performed live cell imaging on yeast strains containing 256 copies of the LacO repeat integrated three kilobases downstream of the *GAL1* gene (see **Fig 2.4A**), the LacO-binding protein LacI fused to GFP, and the fluorescent protein dsRED fused to an HDEL peptide to retain it in the

nuclear envelope. Consistent with previous reports (Casolari *et al.*, 2004; Cabal *et al.*, 2006; Drubin *et al.*, 2006; Taddei *et al.*, 2006), we verified that the *GAL* locus interacts with the nuclear periphery at a higher frequency during transcriptional activation by galactose than when repressed by glucose. Interestingly, we also observed significant interaction between the *GAL* locus and the nuclear periphery when cells were grown in raffinose or glycerol (**Fig 2.1A**). This demonstrates a greater degree of interaction between the *GAL* locus and the nuclear periphery than previously described and suggests that peripheral position of the *GAL* locus occurs in response to the relief of glucose repression.

These observations prompted us to examine whether the interaction of *GAL1* with the periphery relies on similar molecular mechanisms in both active conditions (galactose) and in non-induced conditions (raffinose/glycerol). We first examined the role of SAGA and the NPC in the raffinose and galactose-induced tethers. The interaction between the *GAL* locus and the nuclear periphery had previously been shown to require components of the SAGA complex, such as Ada2, and components of the nuclear pore complex (NPC), such as Nup1 (Cabal *et al.*, 2006). We verified that deletion of either *ADA2* or *NUP1* prevented the efficient interaction of the *GAL* locus with the periphery in galactose, and we also observed decreased interaction with the periphery in raffinose (**Fig 2.1B**). These data indicate that SAGA and the NPC are required for the peripheral localization of the *GAL* locus in both derepressed and induced conditions.

Previous work has shown that the gene-periphery interaction can occur independently of transcription (Schmid *et al.*, 2006; Brickner *et al.*, 2007), consistent with our finding that *GAL* gene recruitment to the nuclear periphery occurs in derepressed conditions (i.e., in raffinose or glycerol medium). This observation led us to re-investigate the role of transcription in the gene-periphery interaction, asking whether the interaction in galactose requires ongoing transcription by using the temperature sensitive allele of RNA polymerase II, *rpb1-1*. We monitored the position of the *GAL* locus in cells containing the *rpb1-1* allele grown continuously in galactose or in raffinose. When transcription is halted by *rpb1* inactivation at the non-permissive temperature (37ºC), the *GAL* locus is no longer maintained at the nuclear periphery in galactose, whereas there is no significant change in wildtype cells at this temperature (**Fig 2.1C**). Moreover, there is no change in the interaction between the *GAL* locus and the periphery in raffinose in the absence of functional RNA pol II. These results demonstrate that the maintenance of the *GAL* locus at the nuclear periphery in galactose is dependent on active transcription, but there is no role for active transcription in the pre-transcriptional tether in raffinose. Together these findings demonstrate the existence of two distinct gene-periphery interactions, differentiated by their requirement for transcription, though both the pre-transcriptional and transcriptional tethers share a requirement for components of the NPC and SAGA nuclear subcomplexes.

The nuclear periphery negatively regulates *GAL* gene expression

Despite intense investigation, the functional significance of *GAL* gene movement to the nuclear periphery has remained elusive. One prevalent hypothesis is that gene

Figure 2.1

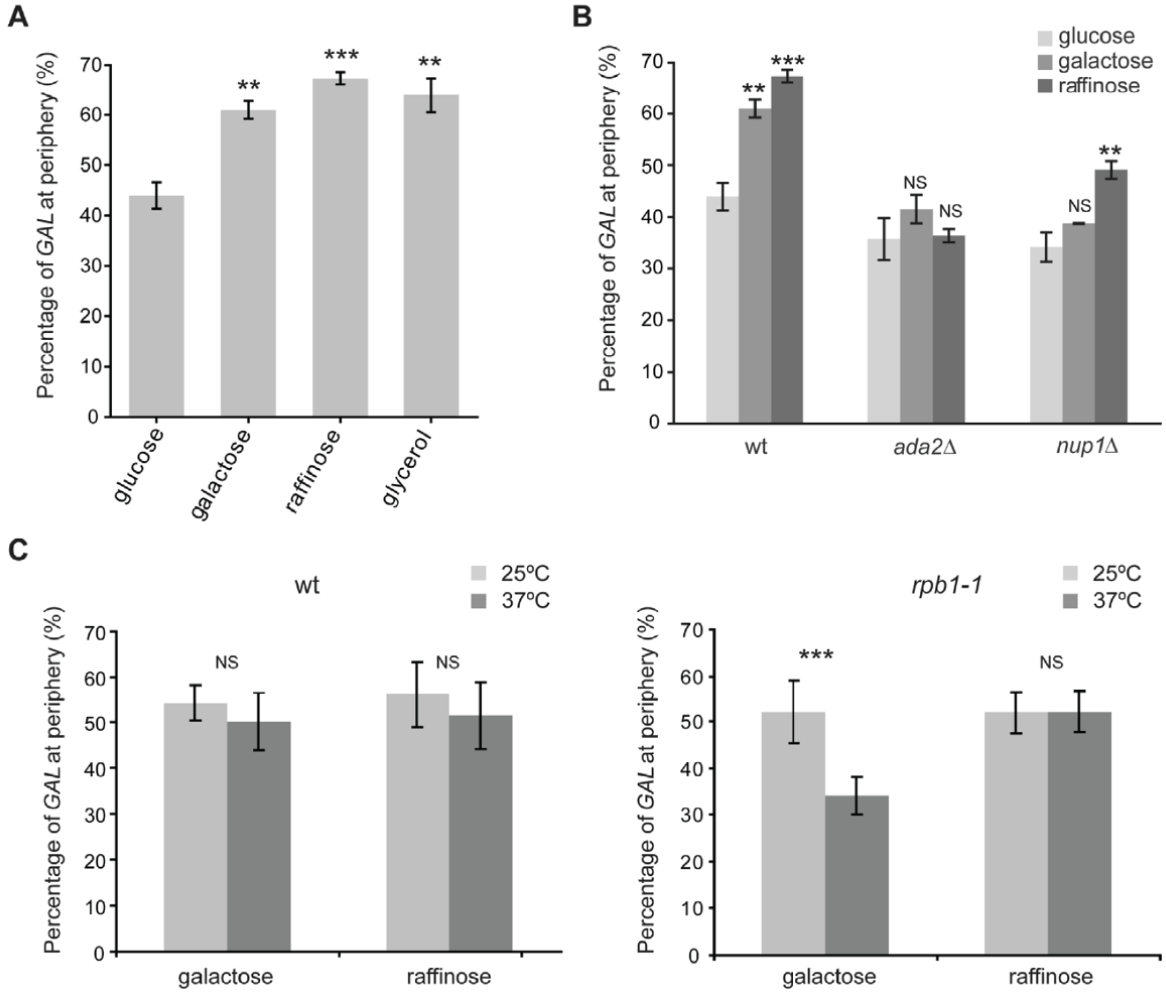

Figure 2.1: Determinants of peripheral positioning of the GAL locus.
A. The *GAL* locus is at the nuclear periphery in the absence of glucose. Wildtype cells expressing the LacO/LacI system and dsRED-HDEL were grown in synthetic medium containing 2% raffinose (SRaf) medium to mid log phase, then maintained in raffinose or shifted to 2% glucose (SGlu), 2% galactose (SGal) or 2% glycerol (SGly) for two hours prior to imaging. Percentage of cells with peripheral localization was scored as described in the Materials and Methods section.
B. *GAL* locus localization in wt and *nup1*Δ or *ada2*Δ mutant cells. The percentage of cells with the *GAL* locus at the nuclear periphery in SGlu, SGal or SRaf for wildtype, *nup1*Δ, and *ada2*Δ cells was determined by microscopy.
C. Localization of the *GAL* locus after transcriptional inhibition. Wildtype and *rpb1-1* mutant cells were grown continuously in SGal or SRaf medium at 25ºC, then shifted to 37ºC for two hours.
The asterisks represent statistical significance as follows: $p > 0.05$ is not significant (NS), $0.05 > p > 0.01$ is one asterisk (*), $0.01 > p > 0.001$ is two asterisks (**) and $p < 0.001$ is three asterisks (***). *p*-values represent a comparison between percentage of cells at the nuclear periphery in glucose to other selected media in wt or mutant cells.

gating at the NPC increases the overall rate of gene expression by facilitating efficient mRNA export (Blobel, 1985; Cabal *et al.*, 2006; Luthra *et al.*, 2007). To test this hypothesis and to analyze the functional role of the gene-periphery interaction, we took advantage of mutations in distinct nuclear subcomplexes, the nucleoporin *NUP1* and the SAGA component *ADA2*, that abrogate the interaction between the *GAL* gene cluster and the nuclear periphery (**Fig 2.1B**). We investigated changes in gene expression associated with disrupting the *GAL*-nuclear periphery interaction using quantitative PCR after reverse transcription (qRT-PCR) to monitor *GAL1* mRNA levels in wildtype, *nup1Δ*, and *ada2Δ* cells pre-grown in glucose and treated with galactose. *GAL1* mRNA levels were measured relative to the non-galactose regulated mRNAs, *ACT1, TFC1* and *ALG9*, at 20, 40 and 60 minutes following galactose induction (**Fig 2.3A** and data not shown). Surprisingly, in both *nup1Δ* and *ada2Δ* cells, an increase in *GAL1* mRNA could be detected at all-time points compared to wildtype cells. At later time points, the expression levels in all strains reach similar steady state levels (**Fig 2.2A**) consistent with prior reports (Cabal *et al.*, 2006). When mutant cells were pre-grown in raffinose and then treated with galactose a similar *GAL1* mRNA hyperinduction phenotype was observed (**Fig 2.2B**).

Since a comparable increase in *GAL1* mRNA levels can be observed in *nup1Δ* and *ada2Δ* mutants, our results suggest that association with the nuclear periphery dampens the induction of the *GAL1* gene. To distinguish whether this repressive effect was primarily caused by direct regulation of transcription or by changes in mRNA turnover, we analyzed the rate of *GAL1* mRNA decay in galactose in wildtype and *ada2Δ* strains, which also contained the RNA polymerase II temperature sensitive allele, *rpb1-1.* Cells were shifted to the non-permissive temperature to inactivate transcription and *GAL1* mRNA turnover was monitored by qRT-PCR and normalized to the RNA polymerase III transcript, *SCR1*. Both wildtype and *ada2Δ* cells displayed identical rates of *GAL1* mRNA decay, ($t_{1/2}$ ~ 25 min; **Fig 2.3B**). These data argue that the increased levels of *GAL1* mRNA in strains lacking the gene-periphery tether is due to an increase in transcription, and not due to a decreased mRNA turnover rate.

In addition to monitoring the kinetics of mRNA expression in the mutants, we also analyzed the effect of disrupting the gene-periphery tether on the kinetics of Gal1 protein production. Using flow cytometry of yeast cells expressing a GFP-tagged Gal1, we followed the protein levels of Gal1-GFP following galactose induction after growth in raffinose. For these experiments we predicted that any delay in mRNA export due to the absence of the gene-periphery tether would be reflected by a slowed rate of protein production. Therefore, we only monitored the protein expression in *ada2Δ* and wildtype cells since *nup1Δ* cells were previously shown to be deficient in mRNA export (Schlaich and Hurt, 1995; Fischer *et al.*, 2002). We observed that the increased level of *GAL1* mRNA found in *ada2Δ* cells was reflected by an increase in protein levels of Gal1-GFP after induction with galactose (**Fig 2.3C**). This demonstrates that the overexpressed mRNA in *ada2Δ* cells is functional and suggests that the localization of the *GAL1* gene adjacent to the nuclear pore complex is not critical for efficient nuclear export of the *GAL1* mRNA.

Figure 2.2

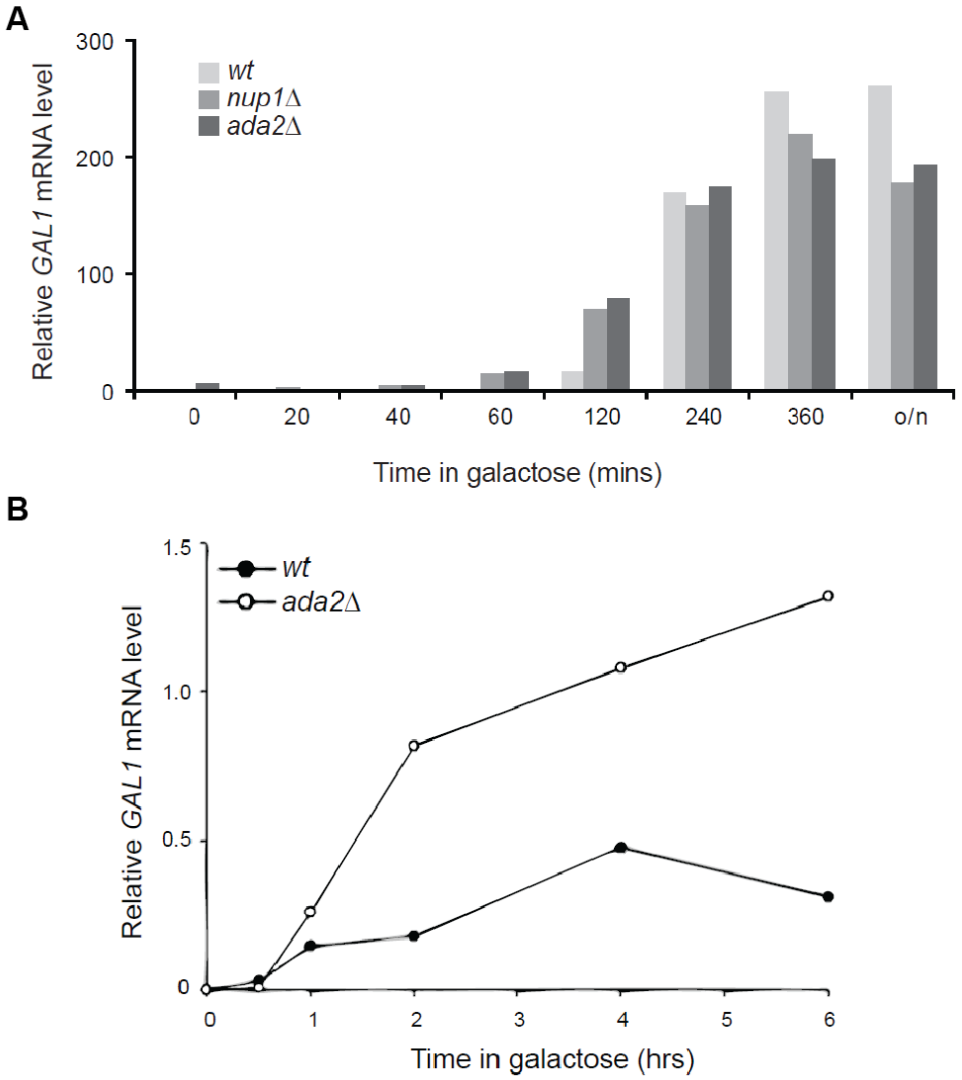

Figure 2.2: *GAL1* mRNA expression after induction in galactose medium.
A. Long-term *GAL1* expression in wildtype and mutant cells. Wildtype, *nup1Δ* and *ada2Δ* cells were grown were grown in YP plus 2% glucose (YPD) to mid-log phase. *GAL1* mRNA expression was induced by galactose. *GAL1* mRNA levels were measured at the indicated times in galactose by qRT-PCR and normalized to ACT1. (o/n = overnight.)
B. *GAL1* mRNA expression levels following growth in raffinose. Wildtype and *ada2Δ* cells were grown in SRaf medium to mid-log phase and then shifted to SGal medium. *GAL1* mRNA levels were measured by Northern blot, normalized to *SCR1* and plotted as a function of time in galactose.

Figure 2.3

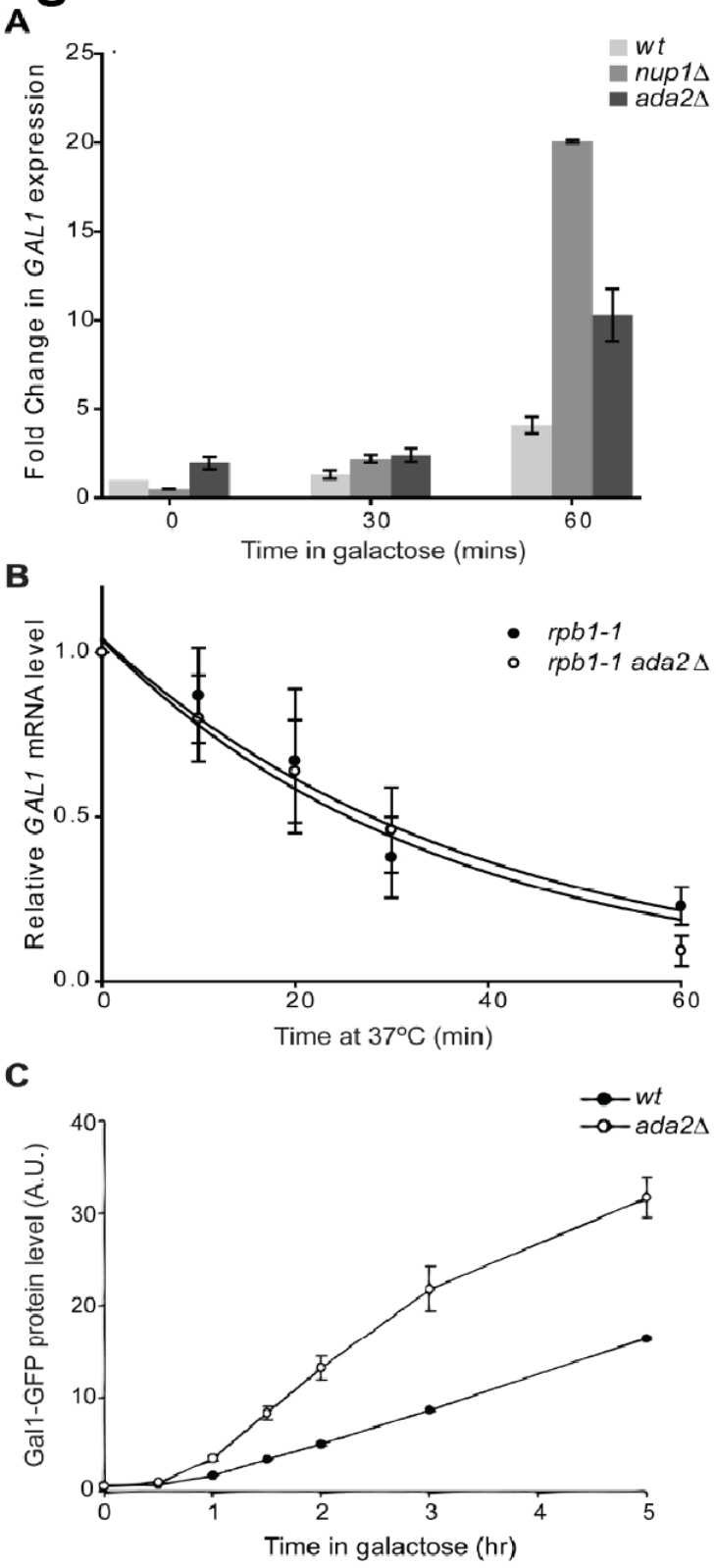
A
wt
nup1Δ
ada2Δ
Fold Change in GAL1 expression
25
20
15
10
5
0
0
30
60
Time in galactose (mins)
B
rpb1-1
rpb1-1 ada2Δ
Relative GAL1 mRNA level
1.0
0.5
0.0
0
20
40
60
Time at 37°C (min)
C
wt
ada2Δ
Gal1-GFP protein level (A.U.)
40
30
20
10
0
0
1
2
3
4
5
Time in galactose (hr)

Figure 2.3: The nuclear periphery inhibits *GAL1* mRNA expression.
A. Changes in *GAL1* mRNA expression in yeast with disrupted peripheral localization of the *GAL* locus. Wildtype, *ada2*Δ or *nup1*Δ mutant cells were grown in YP plus 2% glucose (YPD) to mid log phase. *GAL1* mRNA expression was induced by galactose. *GAL1* mRNA levels were measured at the indicated times by quantitative RT-PCR and normalized relative to *TFC1*. Error bars represent SEM for three independent experiments.
B. *GAL1* mRNA turnover in galactose in wildtype and *ada2* mutant cells. *rbp1-1* and *rbp1-1 ada2*Δ cells were grown in YPGal medium at 25ºC and then shifted to 37ºC to inactivate transcription. *GAL1* mRNA levels were measured at the indicated time points by qRT-PCR, normalized to RNA pol III transcript *SCR1* and plotted as a function of time following the shift to the non-permissive temperature.
C. Gal1 protein levels increase in *ada2*Δ cells. Cells were grown in raffinose medium and induced with 2% galactose for the indicated time and Gal1-GFP protein levels were analyzed using flow cell cytometry. Mean GFP intensity of the population (in arbitrary units) is plotted as a function of time in galactose.
Error bars represent SEM for three independent experiments.

The repressive effect of the nuclear periphery on the *GAL* locus

The *GAL* gene cluster contains two additional galactose-induced genes, *GAL7* and *GAL10*, which are flanked by neighboring genes *KAP104* and *FUR4* (**Fig 2.4A**). *KAP104* encodes for a nuclear transport factor that is constitutively expressed, whereas *FUR4* encodes for a uracil permease previously shown to be partially regulated by Gal4, the key regulator of genes required for galactose metabolism (Ren *et al.*, 2000). To determine the influence of the nuclear periphery on the expression patterns of the entire locus, we also monitored the expression levels of *FUR4, GAL7, GAL10,* and *KAP104* in addition to *GAL1* in wildtype, *nup1Δ* and *ada2Δ* cells by qRT-PCR. Similar to *GAL1*, we observed greatly increased levels of the galactose-regulated genes *GAL7* and *GAL10* in the *nup1Δ* and *ada2Δ* mutants (**Fig 2.4B**). However, we observed no changes for *KAP104* and only a very modest increase in the mRNA levels of *FUR4*.

If hyperactivation of the *GAL* genes in both *nup1Δ* and *ada2Δ* cells is indeed caused by the altered position of the gene within the nucleus, then constitutive tethering of the *GAL* locus to the nuclear periphery should rescue this defect in transcriptional regulation. To test this hypothesis, we constructed a gene-tethering system using the nucleoporin Nup2. The lac repressor (LacI) was fused to the C-terminus of Nup2 and expressed in yeast cells with LacO repeats integrated downstream of the *GAL* locus. The interaction between Nup2-LacI and the LacO repeats was sufficient to tether the *GAL* locus constitutively to the nuclear periphery in both glucose and galactose at a frequency higher than observed for wildtype cells in galactose (**Fig 2.5A**). We monitored the induction of *GAL1* over time in the presence and absence of the Nup2-LacI/LacO tether in cells shifted from glucose to galactose (**Fig 2.4C**). Expression of only Nup2-LacI did not alter transcript levels (**Fig 2.5B**) and *GAL1* hyperactivation was still observed in the presence of the LacO repeats alone in *nup1Δ* cells. Importantly, the kinetics of induction were slower in the presence of the full Nup2-LacI/LacO tether in *nup1Δ*, correlating with the restored peripheral localization of the gene in this strain background. These data show that constitutive tethering of the *GAL* locus to the nuclear periphery is sufficient to rescue the aberrant *GAL1* expression observed in *nup1Δ* cells.

To investigate whether the Nup2-LacI/LacO gene tether caused generalized transcriptional repression around the *GAL* locus or whether it was specific for the *GAL* genes, we also monitored expression of the galactose-induced genes *GAL7* and *GAL10* and the two surrounding genes *KAP104* and *FUR4*. mRNA levels of all genes were detected by qRT-PCR following treatment with galactose in both wildtype and *nup1Δ* strains with and without the Nup2-LacI/LacO gene tether (**Fig 2.4D**). As observed for *GAL1*, the Nup2-LacI/LacO gene tether rescued the hyperinduction phenotype of *GAL7* and *GAL10* detected in *nup1*□ cells. However, the Nup2-LacI/LacO gene tether did not repress *KAP104* or *FUR4* levels below the levels observed in untethered wildtype control cells. Overall, these data suggest that the negative transcriptional control at the nuclear periphery is specific for galactose-regulated genes and is not due to generalized repression of the locus or gene silencing at the nuclear periphery.

Figure 2.4

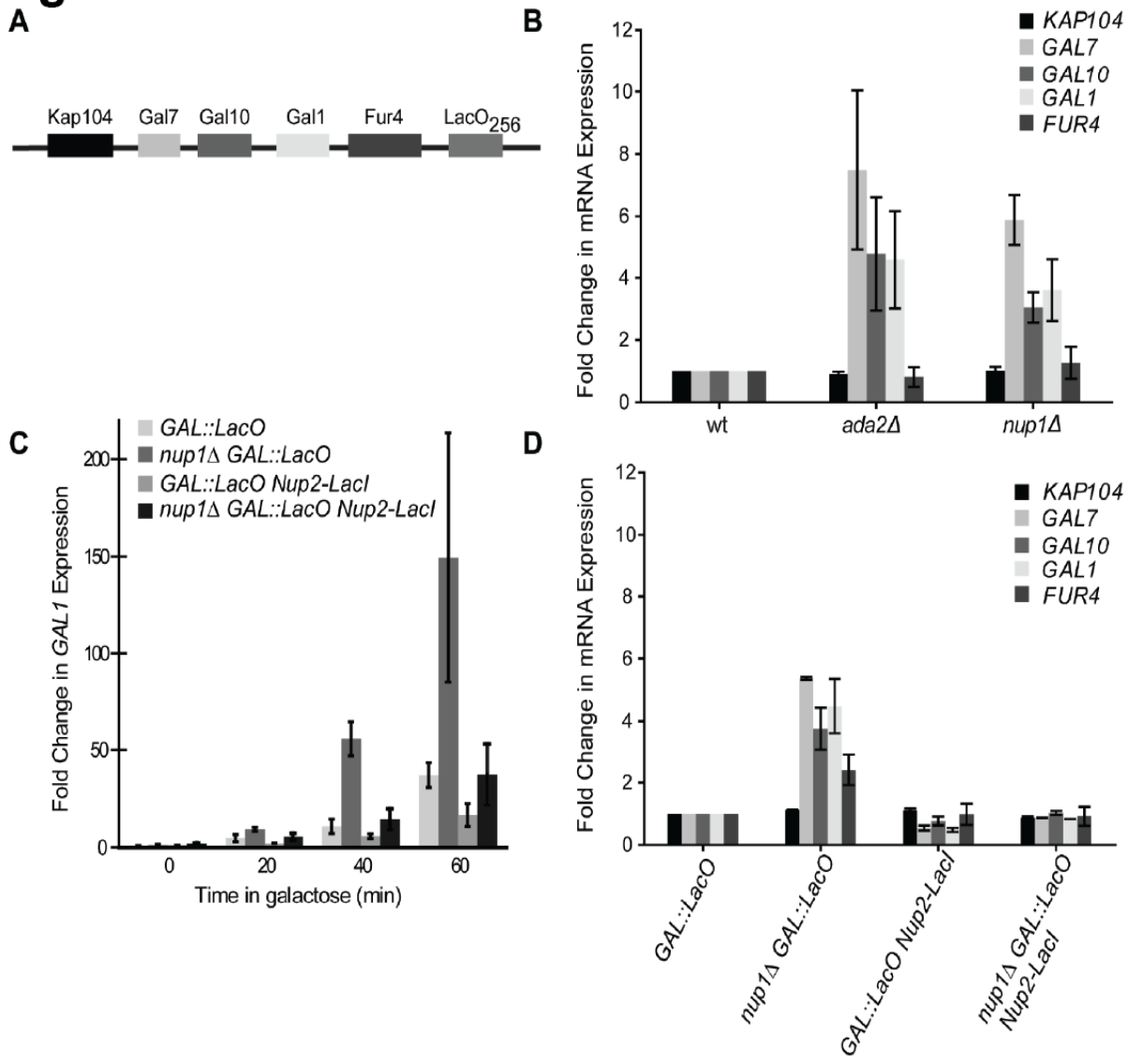
A
Kap104
Gal7
Gal10
Gal1
Fur4
LacO256
B
KAP104
GAL7
GAL10
GAL1
FUR4
Fold Change in mRNA Expression
wt
ada2Δ
nup1Δ
C
GAL::LacO
nup1Δ GAL::LacO
GAL::LacO Nup2-LacI
nup1Δ GAL::LacO Nup2-LacI
Fold Change in GAL1 Expression
Time in galactose (min)
D
KAP104
GAL7
GAL10
GAL1
FUR4
Fold Change in mRNA Expression
GAL::LacO
nup1Δ GAL::LacO
GAL::LacO Nup2-LacI
nup1Δ GAL::LacO Nup2-LacI

Figure 2.4: The nuclear periphery specifically regulates expression of galactose-induced genes.
A. Schematic of the *GAL* locus and adjacent genes on Chromosome II, including the integration site of 256 copies of the LacO repeats.
B. mRNA expression levels of *GAL* locus genes (*GAL1, GAL7*, *GAL10*) and neighboring genes (*FUR4* and *KAP104*) in yeast lacking the gene-periphery tether. Wildtype, *ada2*Δ or *nup1*Δ mutant cells were grown in YPD medium to mid log phase and shifted to YPGal medium for one hour. mRNA levels were measured by qRT–PCR and normalized relative to *TFC1*.
C. Kinetics of *GAL1* expression with constitutive peripheral tethering. *GAL1* gene expression, measured by qRT-PCR in wildtype and *nup1Δ* strains containing the LacO repeats integrated near the *GAL* locus with and without the Nup2-LacI gene tether. Cells were grown in YPD medium and *GAL1* expression was induced with 2% galactose for the indicated times.
D. mRNA expression levels of *GAL* locus genes and neighboring genes with the Nup2-LacI gene tether. mRNA levels were detected by qRT-PCR as described above following 1 hour induction with galactose. Error bars represent SEM.

Figure 2.5

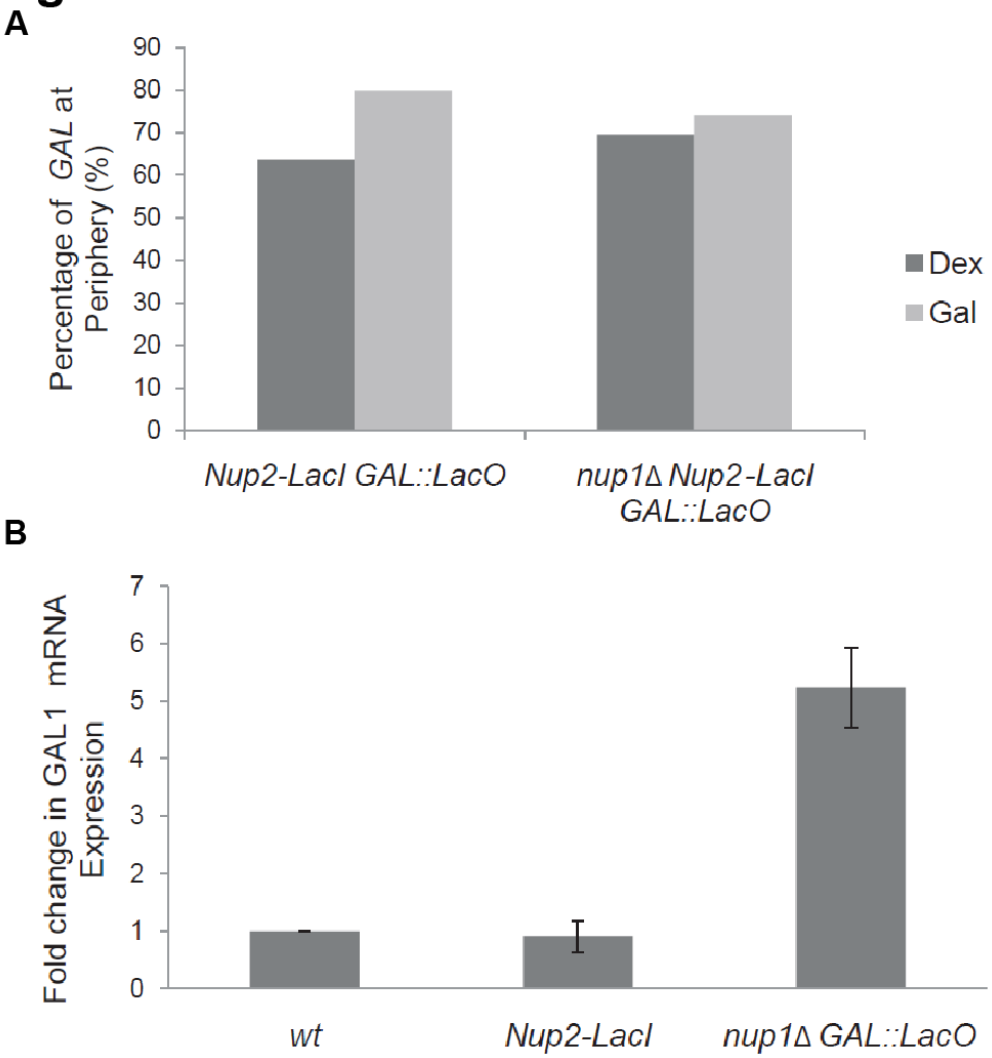

Figure 2.5: Constitutive peripheral tethering of the *GAL* locus through Nup2-LacI.
A. GAL nuclear position in the presence of the Nup2-LacI gene tether. A Nup2-LacI fusion protein which binds the LacO repeats integrated near the *GAL* locus was expressed in both wildtype and *nup1Δ* mutant strains. Cells were grown in synthetic medium containing 2% raffinose (SRaf) medium to mid log phase, then maintained in raffinose or shifted to 2% glucose (SGlu) or 2% galactose (SGal) for two hours prior to imaging. Percentage of cells with peripheral localization was scored as described in the Materials and Methods section. Approximately 50-100 cells were scored for each condition.
B. *GAL1* mRNA levels with the Nup2-LacI gene tether. Cells were grown in YPD medium to mid-log phase and shifted to YPGal medium for one hour. *GAL1* mRNA levels were measured by qRT–PCR and normalized relative to *TFC1*.

Efficient repression of *GAL1* requires interaction with the nuclear periphery

Our analysis of *GAL1* expression kinetics paradoxically shows that relocalization to the nuclear periphery, which is observed upon gene activation, leads to a repression of *GAL* gene induction. However, for yeast cells it is not only critical to rapidly induce appropriate amounts of galactose-responsive genes upon exposure to galactose but it is also very important to swiftly repress *GAL* genes in the presence of glucose, the preferred carbon source. We therefore analyzed whether the gene-periphery interaction also stimulates repression of *GAL1* upon glucose addition. Using qRT-PCR (**Fig 2.6**), we measured the amount of *GAL1* mRNA in wildtype, *nup1Δ* and *ada2Δ* cells that were grown in galactose and subsequently shifted to glucose. As expected (Johnston *et al.*, 1994) repression of galactose-induced genes occurs rapidly in the presence of glucose in wildtype cells. In contrast, the kinetics of repression following the shift to glucose were significantly delayed in both *nup1Δ* and *ada2Δ* mutants. These data show that disrupting the *GAL1*-nuclear periphery interaction delays the rate of repression of *GAL1* upon glucose addition, thereby limiting the cellular response to changes in carbon source.

Taken together, our experiments investigating the effects of gene position on *GAL1* activation and repression demonstrate that the nuclear periphery constitutes a repressive environment for *GAL* gene expression despite the fact that peripheral localization occurs concurrently with transcriptional activation. Furthermore, our results argue that disrupting the interaction between the periphery and the *GAL* locus prevents cells from rapidly repressing *GAL* gene expression upon return to the more favorable glucose conditions.

Discussion

The nuclear periphery represses *GAL* gene expression

The correlation between peripheral *GAL* locus position and transcriptional activation has encouraged the development of numerous models which suggest that the nuclear periphery is directly involved in transcriptional activation or promotes more efficient mRNA export from the nucleus (Blobel, 1985; Cabal *et al.*, 2006; Brickner *et al.*, 2007; Sarma *et al.*, 2007). Here, we monitor the position of the *GAL* locus in live yeast and first demonstrate that the *GAL* locus is positioned at the nuclear periphery both prior to and following transcriptional activation. Both of the pre-transcriptional and transcriptional gene-periphery tethers depend on components of the nuclear pore complex (Nup1) and the SAGA complex (Ada2), previously identified as required for association of *GAL1* with the nuclear periphery concomitant with transcriptional activation (Cabal *et al.*, 2006). The persistence of the *GAL* locus-nuclear periphery interaction in multiple environmental conditions suggests a complex interplay between active genes and the nuclear periphery, the function of which has yet to be elucidated.

To investigate the functional significance of the *GAL* locus-nuclear periphery interaction, we took advantage of yeast mutants in the nucleoporin *NUP1* or the SAGA component *ADA2* to disrupt the interaction between the *GAL* locus and the nuclear periphery. Surprisingly, in these mutants we observed a significant increase in *GAL*

Figure 2.6

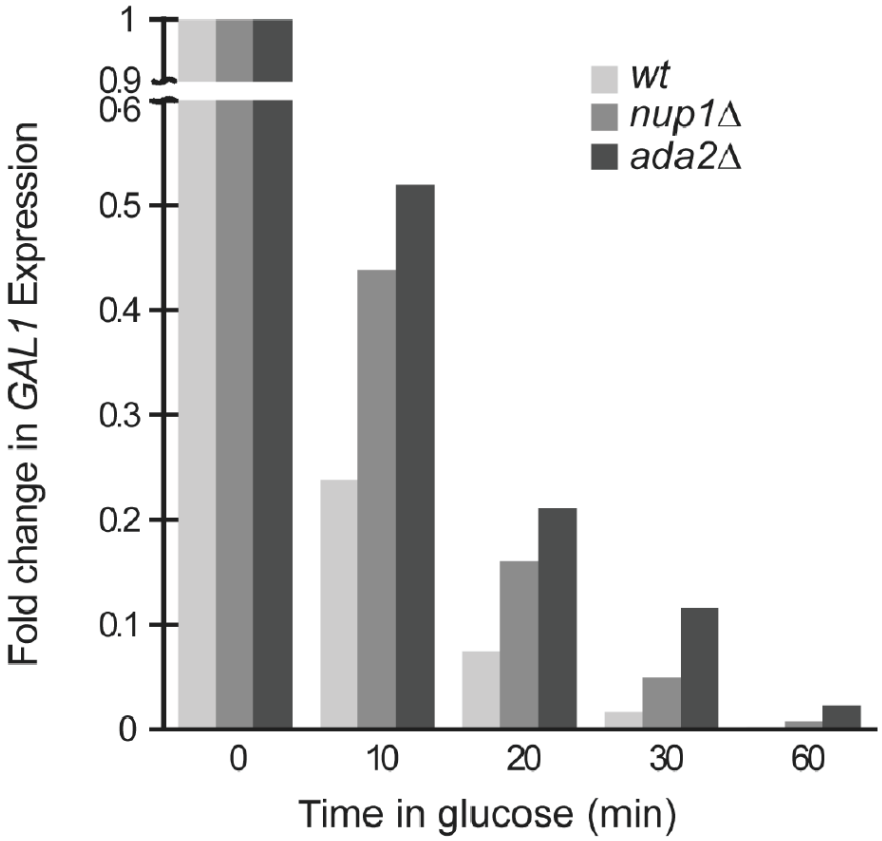

Figure 2.6: Repression of *GAL1* is delayed with a disrupted gene-periphery tether. Wildtype, *nup1Δ* and *ada2Δ* strains were grown at room temperature in YP plus 2% raffinose to mid log phase. *GAL1* mRNA expression was induced by galactose addition for 2 hours and then inhibited by the addition of glucose for the indicated time. *GAL1* mRNA levels were monitored by qRT-PCR and normalized to the control gene, *ACT1*. The fold change is calculated relative to the transcript levels for each strain at the zero timepoint, defined as 1.0.

gene expression kinetics compared to wildtype cells (**Fig 2.3A**). This hyperinduction seems to be primarily mediated by an increase in transcription (**Fig 2.3B**) and could be observed in all *GAL* genes tested (*GAL1*, *GAL7* and *GAL10*). By contrast, the peripheral localization had little or no effect on two neighboring genes *KAP104* and *FUR4* (**Fig 2.4B**). It is of note that our results do not contradict previous measurements of steady-state mRNA levels (Cabal *et al.*, 2006) in that we see little difference between wildtype, *nup1Δ* and *ada2Δ* mutants once expression levels have reached saturation (**Fig 2.2A).** These results also parallel recent work showing that disruption of peripheral positioning of actively-transcribing ribosomal protein genes results in their increased expression (Yoshida *et al.*, 2010).

Our observations demonstrate three important aspects of the gene-nuclear periphery interaction. First, although association of the *GAL* locus with the nuclear periphery *correlates* with gene activation, localization at the nuclear periphery itself is not required for transcriptional activation or gene expression, and in fact peripheral localization negatively regulates *GAL* gene expression. Second, our findings do not support the original gene gating hypothesis (Blobel, 1985) because mRNA processing and/or export of *GAL1* are not significantly delayed when the gene is not peripheral (**Fig 2.3C)**. This also suggests that, at least in yeast, the diffusion of mRNA from the site of transcription to the nuclear pore complex is not a rate-limiting step in gene expression. Third, our observations indicate that the spatial position of the *GAL* genes within the nucleus is important for regulating their activity. Similar increases in *GAL1* expression are observed in strains with deletions of either *ADA2* or *NUP1*, whose gene products function in separate nuclear complexes,. This is most likely explained by their shared phenotype: the disruption of the gene-periphery interaction and the mislocalization of the gene to the nuclear interior.

We further show that the nuclear periphery is not only necessary but also sufficient for establishing repressive conditions for modulating *GAL* gene expression levels, as we observed a decrease in *GAL1, GAL7* and *GAL10* expression in *nup1Δ* cells when the *GAL* locus is constitutively tethered to the nuclear pore complex (**Fig 2.4C** and **2.4D**). Since the aberrant *GAL* gene expression pattern in *nup1Δ* cells can be rescued by tethering the genes to the nuclear periphery, this indicates that the misregulation in these mutants can be attributed specifically to the disrupted gene-periphery interaction. Thus, the nuclear periphery likely plays a role in dampening the activation of the *GAL* genes to maintain the appropriate transcript levels for the cell's response to galactose, consistent with several previous studies linking the nuclear periphery with transcriptional repression and gene silencing (Andrulis *et al.*, 1998; Feuerbach *et al.*, 2002; Akhtar and Gasser, 2007).

Whether this repressive effect is specific to the *GAL* genes or whether the nuclear periphery and the nuclear pore also inhibits other dynamic gene loci is unclear. Here, we have only analyzed the effects of Nup1 but the nuclear pore complex provides a versatile platform that recruits components of multiple activities and it is very likely that the regulation of gene expression at the nuclear periphery is not only limited to repression (reviewed in Arib and Akhtar, 2011; Liang and Hetzer, 2011). Consistent with this, wide-ranging variability in results has been observed in several other gene tethering experiments that have been performed in both yeast (Andrulis *et al.*, 1998; Brickner and Walter, 2004; Taddei *et al.*, 2006; Brickner *et al.*, 2007) and metazoans

(Finlan *et al.*, 2008; Kumaran and Spector, 2008; Reddy *et al.*, 2008) using either reporter or endogenous genes. This suggests that there are gene-specific means of transcriptional control occurring at the nuclear periphery, in different peripheral subdomains, or at the nuclear pore. This would be in agreement with the differential effects on expression that we observe in the presence of the gene-periphery tether for the SAGA-dependent *GAL1*, *GAL7* and *GAL10* genes, and SAGA-independent genes such as *KAP104*. In this context, it is also intriguing that the *INO1* gene appears to rely on a distinct peripheral tethering mechanism since it requires *cis* acting DNA elements that promote either the initial localization to the periphery or a peripheral interaction that serves as a form of transcriptional memory. Interestingly, these DNA elements are not present at the *GAL* locus (Ahmed *et al*., 2010; Light *et al*., 2010).

A negative feedback loop governs gene expression at the nuclear periphery

In addition to modulating levels of *GAL* gene expression upon induction, we also identified a role for peripheral positioning of the *GAL* locus in facilitating rapid repression of *GAL1* following the shift from galactose to glucose. When *GAL1* is positioned in the nuclear interior, repression by the addition of glucose is slowed significantly when compared to peripherally positioned *GAL1* (**Figure 2.6**). The molecular mechanism of *GAL* gene repression at the periphery remains unclear. One plausible hypothesis is that re-positioning of the *GAL* locus towards the nuclear periphery upon activation may increase access to either a general or gene-specific repressive factor that modulates transcription. Interestingly, the glucose repressor Mig1 is enriched at the nuclear periphery (Sarma *et al.*, 2007) and is required for the movement of the *GAL* locus toward the nuclear envelope upon activation (Vodala *et al.*, 2008). While this manuscript was in revision, it was further shown that components of the nuclear pore are important for Mig1 recruitment to target promoters (Sarma *et al.*, 2011). It will now be interesting to investigate the role of Mig1 in *GAL* gene repression at the nuclear periphery described here.

What is the physiological relevance of *GAL* gene movement to the repressive environment of the nuclear periphery upon transcriptional activation? Our results suggest that *GAL* gene localization to the nuclear periphery is an important mechanism for cells to quickly respond to changing environmental conditions. This supports a model in which the nuclear periphery is part of a negative feedback loop that regulates *GAL* gene expression and provides yeast cells with a mechanism for adaptive plasticity in changing environmental conditions. A very rapid repression of *GAL* gene expression may be particularly important for yeast cells when they return to their preferred carbon source, glucose. Further investigations into the molecular mechanism of this novel feed-back loop in *GAL* gene regulation will provide important insight into how position-dependent gene expression patterns emerge in response to environmental stimuli.

Materials and methods

Yeast Strains

All *Saccharomyces cerevisiae* strains used in this study are listed in **Table 2A.** The KWY strain background is W303. Standard growth conditions and manipulations were utilized. All gene deletions and epitope tag integrations were performed using standard techniques (Longtine *et al.*, 1998). Plasmids containing *LacI-GFP::HIS3* and *$LacO_{256}$::LEU2* repeats for integration into yeast were gifts from A. Straight (Straight *et al.*, 1996) but the LacO-containing plasmid was modified to integrate at *YBR022w.* The integration plasmid allowing for expression of dsRED-HDEL was described previously (Madrid *et al.*, 2006). Yeast strains expressing the Nup2-LacI fusion protein were generated by integration of a PCR product amplified from plasmid pKW2139 (pFA6a*LacI::KanMX*) with flanking sequence to target the 3' end of the *NUP2* coding region to generate a C-terminal fusion. KWY1302 (*MATa rpb1*-1) was generated by backcrossing the *rpb1-1* allele (Morrissey et al., 1999) to KWY165. KWY2619 was constructed using the same strategy as described for KWY1622 but using KWY1302 as the initial strain for construct integration.

Microscopy

All microscopy experiments were performed using synthetic complete (SC) medium. Cells were grown to mid log phase (O.D.600 ~ 0.4-0.6) in SC plus either 2% glucose, 2% raffinose or 2% galactose. To score large numbers of yeast cells efficiently, live yeast were imaged and recorded using an epifluorescence microscope equipped with a Hamamatsu interline CCD camera. When overlap between the LacI-GFP signal in the green channel and the nuclear envelope signal in the red channel was observed, these cells were scored as having the gene locus at the nuclear periphery. To validate this method of scoring, we compared this approach to image analysis on a deconvolution microscope. In these experiments, position in the nucleus was determined by manually identifying the focal plane for the LacI-GFP spot and measuring the shortest distance from the center of the spot to the center of the nuclear rim using the Softworx program. If the distance was less than 200nm (the approximate resolution of this technique), the *GAL* locus was scored as peripheral. Both techniques yielded comparable changes in peripheral localization upon galactose induction.

RNA isolation

For analysis of mRNA levels of *GAL* locus genes (*GAL1, GAL7* and *GAL10*) and neighboring genes (*FUR4* and *KAP104*) following galactose induction, yeast were grown in YP (yeast extract, peptone) media plus 2% glucose at 25º C until mid-log phase. Cells were harvested, washed in YP two times and resuspended in YP plus 2% galactose. For analysis of *GAL1* mRNA following glucose repression, cells were grown to mid log phase in YP plus 2% raffinose at 25ºC, then shifted to YP plus 2% galactose for an additional two hours. Cells were harvested and resuspended in YP plus 2% glucose. For each timepoint analyzed, an aliquot of cells was harvested by centrifugation and frozen in liquid nitrogen. Total RNA was isolated using the RibopureTM-yeast kit (Ambion). RNA samples were treated with DNAse I (Ambion) to remove contaminating genomic DNA.

Table 2A. Yeast strains used in this study.

Strain #	Genotype	Source
KWY681	*MATa nup1Δ::HIS3*	(Zeitler and Weis, 2004)
KWY1695	*MATα ada2Δ::KANMX*	this study
KWY1622	*MATα ybr022w::LacO::LEU2 his3::LacI-GFP::HIS3 trp1::dsRED-HDEL::TRP1*	this study
KWY1758	*MATα ybr022w::LacO::LEU2 his3::LacI-GFP::HIS3 trp1::dsRED-HDEL::TRP1 ada2Δ::KANMX*	this study
KWY1823	*MATα ybr022w::LacO::LEU2 his3::LacI-GFP::HIS3 trp1::dsRED-HDEL::TRP1 nup1Δ::NATMX*	this study
KWY2348	*MATa gal1::GAL1-GFP::KANMX*	this study
	MATα ada2Δ::NATMX gal1::GAL1-GFP::KANMX	this study
KWY2082	*MATa ybr022w::LacO::LEU2 his3::LacI-GFP::HIS3 trp1::dsRED-HDEL::TRP1 nup2::Nup2-LacI::KANMX*	this study
KWY2079	*MATa ybr022w::LacO::LEU2 trp1::dsRED-HDEL::TRP1 nup2::Nup2-LacI::KANMX*	this study
KWY2117	*MATa ybr022w::LacO::LEU2 trp1::dsRED-HDEL::TRP1 nup2::Nup2-LacI::KANMX nup1Δ::HIS3*	this study
KWY1302	*MATa rpb1-1*	this study; (Morrissey et al., 1999)
KWY2551	*MATa rpb1-1 nup1Δ::HIS3*	this study
KWY2552	*MATa rpb1-1 ada2Δ::KANMX*	this study
KWY2619	*MATa rpb1-1 ybr022w::LacO::LEU2 his3::LacI-GFP::HIS3 trp1::dsRED-HDEL::TRP1*	this study

qRT-PCR

An oligo dT_{20} was used for first strand synthesis for all mRNA expression experiments except for the *GAL1* mRNA decay experiment (**Fig 2.3B**), in which random primers (Invitrogen) were used. Superscript SS III reverse transcriptase (Invitrogen) was used to make cDNA from 2 µg total RNA for each sample. qRT-PCR was performed in an Applied Biosystems 7300 Real Time PCR machine using Taqman Universal PCR Mastermix (Applied Biosystems) with 5'FAM/3'-BHQ-1 Taqman probes, or in an Applied Biosystems StepOne Plus Real Time PCR using Absolute Blue QRT-PCR SYBR Green ROX Mix (Thermo Fisher Scientific) supplemented with gene-specific primers (described in **Table 2B**).

Northern blotting

Cells were harvested and frozen in liquid nitrogen immediately. Total RNA was isolated using a RibopureTM-yeast kit (Ambion). A 300bp *GAL1* probe was amplified by primer UC3219 and primer UC3220 (**Table 2B**) using wild type yeast genomic DNA as a template and labeled using a random primed DNA labeling kit (Roche). *SCR1* probe UC3187 was labeled by a T4 polynucleotide kinase kit (Roche). Blots were imaged using a Molecular Dynamics phosphoimager, scanned by Typhoon TRIO and quantified using ImageQuant 5.0.

Flow Cell Cytometry

To monitor the expression levels of Gal1-GFP after induction, yeast were grown to early-mid log phase (OD_{600} ~ 0.4) in SC medium containing additional adenine and 2% raffinose. Cells were then diluted to an OD_{600} ~0.2 and simultaneously induced in SC medium containing 2% galactose and adenine. Timepoints 0, 30, 60, 90, 120, and 180 min were treated with 10ug/mL cycloheximide and held on ice for 2-4 hours to allow all translated Gal1-GFP protein to properly fold before sorting. The 300 min timepoint was immediately sorted without cycloheximide treatment. Analysis was performed on an EPICS XL-MCL (Beckman-Coulter) flow cytometer. Measurements from flow-cytometry were plotted as a histogram (Y-Axis number of cells; X-Axis Log GFP Intensity). Threshold GFP intensities were gated such that only 0-2% of a glucose-grown wildtype culture would sort as GFP-positive. Gal1-GFP expression levels were determined by taking the geometric mean of GFP intensity for the population of cells.

Acknowledgements

The authors are grateful to Matt Welch, Zain Dossani, Elisa Dultz, Johanna Carroll and Benjamen Montpetit for input, discussions, and comments on the manuscript. The authors would like to thank Denise Schichnes and Steve Ruzin of the UC Berkeley College of Natural Resources Biological Imaging Facility for microscopy support and Hector Nolla for help with flow cytometry. The authors also thank Christiane Brune for expert technical assistance. This work was supported by NIH grant GM58065 (to K.W.).

Table 2B. Primers and probes used for qRT-PCR and RT-PCR.

Primer #	Primer Name	Sequence
UC2955	Act1F	TCCATTGCTTTGTCAAATGG
UC2956	Act1R	CCTGGAACCAAGTGAACAGT
	FAM-Act1-BHQ	AGCCAGCTCCGGTCAAACGG
UC2997	Gal1F	TGGATTCCGGTGATGGTGTT
UC2998	Gal1R	TCAAAATGGCGTGAGGTAGAGA
	FAM-Gal1-BHQ	CTCACGTCGTTCCAATTTACGCTGGTTT
UC3304	Fur4F	GCATATCTATGTGGGGTGGCT
UC3305	Fur4R	ATCGACATTGGCCCATCTTT
UC3306	Kap104F	TCCAACTGGTCTTCAAATGCT
UC3307	Kap104R	GGTCGTTTTCGTCGTTTTGT
UC3219	Gal1probeF	CCGTTTAAATTTCCGCAATTAAAAAAC
UC3220	Gal1probeR	CTAGCATCTTTGTTAACCGTTCGAT
UC3187	Scr1probe	CCTCGCAGAGAGACGGATTCCTCACGCCTCCTGCCAACG

Chapter 3:

Correlations of the three-dimensional motion of chromosomal loci

Note: The work presented in the following chapter was performed in collaboration with W.E. Moerner and Mikael Backlund (primary author, analysis, and experimentation). My specific contributions include secondary authorship, project conception and experimental design, as well as experimentation.

Background

In recent decades the application of fluorescence microscopy to the imaging and tracking of chromatin has revealed a wealth of dynamics in both eukaryotic and prokaryotic cells. While the importance of chromatin positioning and movement during cell division was documented long ago, the formerly static picture of chromatin during interphase has undergone extensive revision. Studies have consistently shown that loci of chromatin undergo constant random motion during interphase that is best described as subdiffusive within some finite volume of confinement (Albert et al., 2012; Marshall et al., 1997; Vazquez et al., 2001; Huen et al., 2001). At the same time, there is increasing evidence that the positioning of genes and the chromosomes they comprise within the three-dimensional (3D) volume of the nucleus (in eukaryotes) is in fact nonrandom. Chromosomes in higher order eukaryotes are segregated into distinct sub-nuclear sections called “chromosome territories” (Cremer et al., 2006). Analogous units seem to persist even in the relatively small nucleus of the model organism budding yeast (*Saccharomyces cerevisiae*) (Berger et al., 2008). Chromosome conformation capture techniques have shown that gene loci that are distantly positioned in linear genetic space can often be clustered in real 3D space (Duan et al., 2010; Lieberman-Aiden, et al., 2009). Inter-gene proximity may in some cases be tied to the fact that certain sets of genes exhibit common transcriptional control. For instance, genes that are silenced together may be positioned near shared silencing factors (Gasser et al., 2004). Conversely, genes that are activated together may cluster near common “transcription factories”, i.e. foci of active RNA polymerases (Sutherland et al., 2009).

Furthermore, the positioning and motion of certain loci have been found to change in response to factors such as transcriptional status. One notable example is the cluster of *GAL* genes in budding yeast (i.e. the *GAL* locus), consisting of three genes (*GAL*7, *GAL*10, and *GAL*1) along Chromosome II. The *GAL* genes code for various enzymes necessary for the metabolism of galactose. When the supply of the preferred carbon source dextrose is ample, the *GAL* genes are repressed and the locus is more often found near the center of the nucleus, away from the nuclear envelope (in ~70% of cells). When dextrose is scarce but galactose is available, the genes become activated and are more often found at the nuclear periphery associated with factors of the Nuclear Pore Complex (in ~60% of cells) (Casolari et al., 2004). The character of the motion of the *GAL* locus changes dramatically in conjunction with this repositioning as its subdiffusive movements become constrained to sliding along the inner membrane of the nuclear envelope, effectively reducing the dimensionality of the motion (Cabal et al., 2006). While a naïve assessment of these findings may suggest a gene-gating hypothesis (Blobel et al., 1985) for the basis of this repositioning, a recent study from the Weis group demonstrated a more nuanced relationship (Green et al., 2012). Specifically, the tethering of the *GAL* locus to the periphery diminishes initial induction of the genes and is required for rapid repression after gene inactivation, effectively establishing a negative feedback mechanism (Green et al., 2012; Texari et al., 2013). This result is consistent with the traditional view of the nuclear periphery as a generally repressive environment (Akhtar and Gasser, 2007; Ahmed and Brickner, 2007).

Results and Discussion

In the current study, we applied wide-field 3D fluorescence microscopy to simultaneously track both copies of the *GAL* locus in G1 diploid yeast cells in order to assess the presence of correlations between two loci located on separate chromosomes under both activating and repressive conditions. Because association with common transcriptional machinery has been implicated in distant genomic correlations, we hypothesized that the two *GAL* loci of diploid yeast may exhibit transcription-dependent correlated movements, especially since its motions and positioning are already known to correlate so strongly with its transcriptional status. Therefore, to conduct simultaneous tracking we labeled one copy of *GAL* with the LacO/LacI-GFP system and the other with the TetO/TetR-mCherry system. We collectively refer to this Dual-Label Dual-Chromosome scheme as DLDC. As a negative control, we also conducted experiments in which we simultaneously tracked only one copy of the *GAL* locus along with one copy of the gene *PES4* located on Chromosome VI, since both the nuclear positioning and transcriptional regulation of *PES4* is unaffected by growth in galactose (Taddei et al., 2006). As a positive control we simultaneously labeled two loci at different locations along the same copy of Chromosome II, with TetO repeats integrated at the same region near *GAL* and LacO repeats integrated at various distances away. We imaged three such Dual-Label Single-Chromosome (DLSC) strains with label separations of 3 kbp, 12 kbp, and 97 kbp, respectively. Finally, as an ultimate positive control on the magnitude of estimated correlations we were capable of measuring in the presence of limiting factors such as localization noise and registration error, we imaged the single copy of the *GAL* locus in haploid cells (the MATa parent of the DLDC strain) labeled with LacO/LacI-GFP in both the green and red color channels. This was made possible by the observation that in the absence of red protein to swamp the signal, the red tail of the GFP emission spectrum was significant enough to track the GFP-labeled locus in the red channel, given sufficiently increased laser intensity. All controls described here were grown and imaged in dextrose. These conditions and labeling schemes are summarized in **Fig 3.1**.

To carry out 3D wide-field tracking we employed the Double-Helix Point Spread Function (DH-PSF) microscope (Pavani et al., 2009; Thompson et al., 2010). Briefly, the DH-PSF microscope enables 3D position estimation from a single image by forcing the light emitted from a single point into two closely spaced lobes in the image. The lobes assume different angles between the line connecting their center points and the vertical as a function of z-position relative to the focal plane (**Fig 3.2A**). Thus, as a tracked locus moves in z the two lobes in its image revolve around one another effectively tracing out a double-helix shape. From a single snapshot we first fit a double-Gaussian function (i.e. the sum of two 2D Gaussians plus a constant offset) using least-squares. The midpoint between the positions of the Gaussians gives the lateral position, while comparison of the angle of revolution to a calibration curve gives the z-position, all to within sub-diffraction (~10-40 nm) precision. Previous studies of 3D chromatin tracking in yeast have often employed confocal scanning methods (Cabal et al., 2006; Bystricky et al., 2005; Neumann et al., 2012; Gartenberg et al., 2004) which is excellent for time-lapse tracking over longer periods of time, but limits the attainable temporal resolution and throughput. Our wide-field/non-scanning approach allows for improved temporal

Figure 3.1

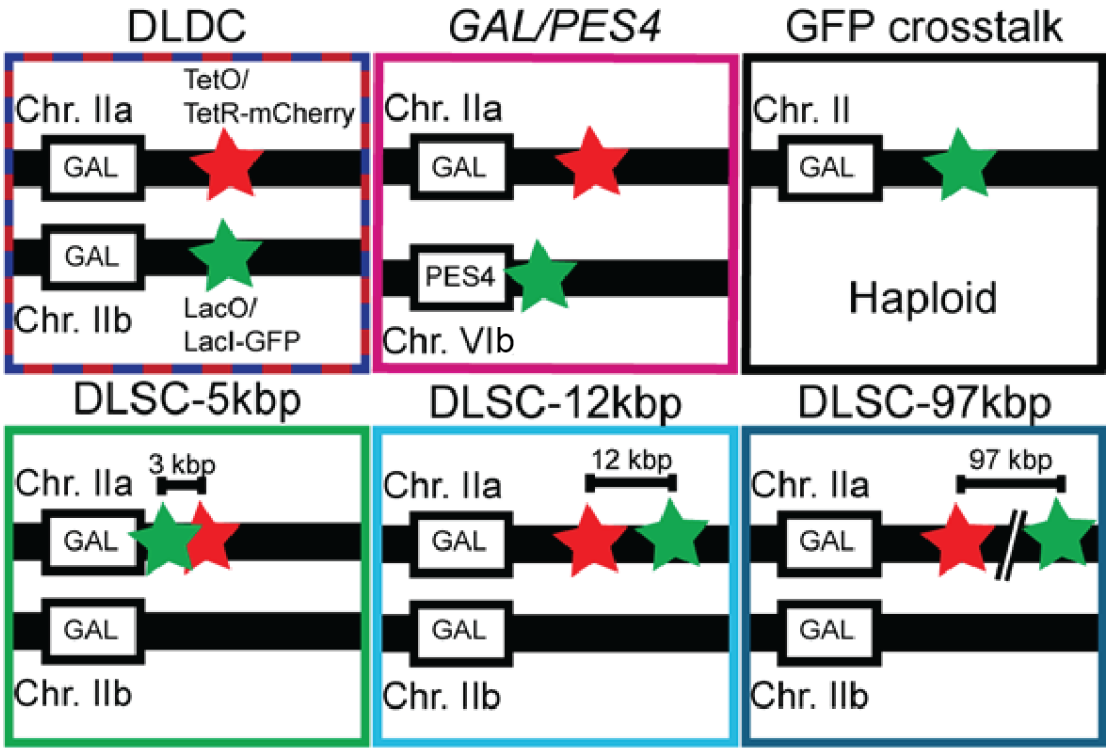

Figure 3.1: Labeling scheme for each condition imaged.
Green star corresponds to LacO/LacI-GFP label and red star corresponds to TetO/TetR-mCherry label. TetO repeats were integrated at the same position relative to the *GAL* locus (<3 kbp from *GAL1*) wherever present. LacO repeats were integrated in the same position (i.e. <3 kbp from *GAL1*) for the DLDC and GFP crosstalk experiments. LacO repeats are immediately adjacent to the 5' end of PES4 for the *GAL/PES4* experiment.

resolution (10 Hz imaging rate) and throughput (~100 cells). Another wide-field/non-scanning technique based on V-shaped micro-mirrors has also been previously utilized for yeast chromatin tracking (Hajjoul et al., 2009).

Fig 3.2B depicts images from each fluorescence channel of a single example cell at different times during the trajectories. In each image we see the two lobes of the DH-PSF on top of a slightly larger circular background, likely due to unbound fluorescent proteins dispersed throughout the nucleus. Once we fit the two trajectories of a pair we registered the tracks in 3D by transforming the red channel data into the coordinates of the green channel using a recently published method (Gahlmann et al., 2013). The 3D target registration errors of the transformation were in the range 10-20 nm, though an additional bias due to refractive index mismatch also had to be treated. **Fig 3.2C** shows a 2D projection of the registered tracks from **Fig 3.2B** overlaid on the white light image of the cell.

After fitting and filtering as described in the **Materials and Methods** section we obtained the following numbers of analyzed track pairs in each condition: $N_{DLDC\text{-}dextrose}$ = 110, $N_{DLDC\text{-}galactose}$ = 104, $N_{GAL/PES4}$ = 40, $N_{DLSC\text{-}3kbp}$ = 28, $N_{DLSC\text{-}12kbp}$ = 35, $N_{DLSC\text{-}97kbp}$ = 47, $N_{crosstalk}$ = 122. DLDC-dextrose data was collected in three separate sets (N_1 = 53, N_2 = 37, N_3 = 20) and the DLDC-galactose data was recorded in two sets (N_1 = 31, N_2 = 73). The mean track pair length across all conditions was 291 frames (29.1 s) with a standard deviation of 146 frames (14.6 s). The track lengths were mostly limited by the bleaching of mCherry, which generally gave lower signal-to-background ratios than the GFP. This is reflected in the estimated approximate values of localization precision we obtained: $[\sigma_x, \sigma_y, \sigma_z]$ = [12 nm, 12 nm, 22 nm] for green and [23 nm, 27 nm, 41 nm] for red. These estimates were obtained by calculating the time-averaged mean square displacement (TAMSD) for each trajectory and finding the TAMSD-intercept obtained by tracing back the line connecting the first two points of the TAMSD. Inversion of a well-known equation (Savin and Doyle, 2005) gives an expression for the localization precision in terms of this intercept. We stress that these values are only approximate since this treatment only holds for pure Brownian motion. These reported values are the averages of the distributions of errors calculated from each individual TAMSD.

Inter-Locus Distances

Cis-acting regulatory elements were recently reported to induce clustering of distinct gene loci in yeast (Brickner et al., 2012). We therefore hypothesized that transcriptional activation of the *GAL* loci may induce a similar change in the 3D distance between the two loci. To explore this possibility we computed the time average of the 3D inter-locus distance over the first 10 frames (when signal is highest) of each track pair. These values were then binned to produce the distributions shown in **Fig 3.3**. **Fig 3.3A** shows the Probability Density Functions (PDFs) and **Fig 3.3B** shows the associated Cumulative Distribution Functions (CDFs) under each condition. The narrowly peaked PDF of the crosstalk experiment gives the lower limit for our estimates of inter-locus distance set by localization and registration errors. The mean of this distribution is $\langle R_{crosstalk} \rangle$ = 48 ± 2 nm (mean ± SE determined from 100 bootstrapped samples), which is on the order of what is expected from the approximate localization errors given in the previous section. The three DLSC cases each peak to the right of

Figure 3.2

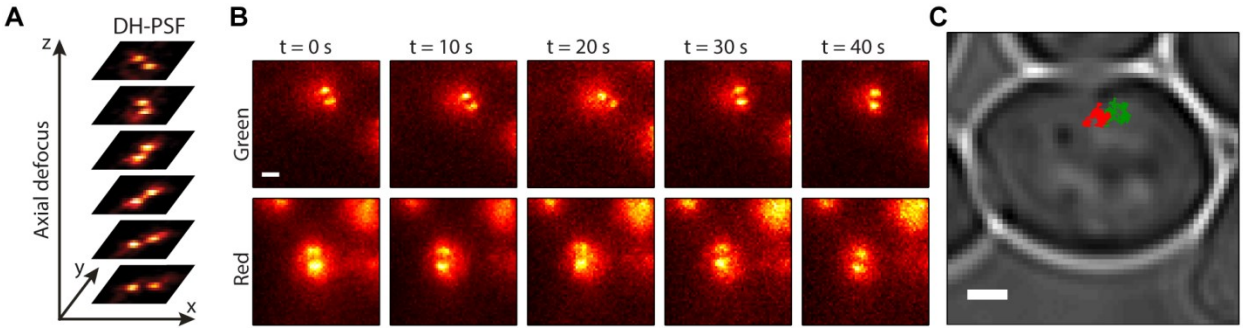

Figure 3.2: DH-PSF imaging of gene loci.
A. Behavior of the DH-PSF as a function of axial defocus (z).
B. Fluorescent images from the green (top) and red (bottom) channels at 10-s intervals of one example track pair. Scale bar = 1 μm.
C. 2D projection of trajectories from (**B**) overlaid on white light image of whole cell. Scale bar = 1μm.

this limit, in the expected order: $\langle R_{DLSC\text{-}3kbp} \rangle$ = 243 ± 19 nm, $\langle R_{DLSC\text{-}12kbp} \rangle$ = 302 ± 20 nm, and $\langle R_{DLSC\text{-}97kbp} \rangle$ = 432 ± 38 nm. A previous study using fluorescence *in situ* hybridization (FISH) found results similar to our DLSC-97kbp case for yeast loci separated by a similar genomic distance along Chromosome VI (436 nm for 103 kbp separation) (Bystricky et al., 2004). However, the smallest genomic distance they studied, 14 kbp in haploid cells and 30 kbp in diploids, gave average Euclidian distances of 60 nm and ~160-190 nm, respectively, significantly smaller than either the DLSC-3kbp or -12kbp cases we found here. Possible reasons for this discrepancy are several fold: for one, the FISH portion of their study reported distances from a single 2D confocal section. This procedure could cause deflation of the true value since the z-extent of a confocal section is nonzero due to diffraction. Second, our method employs an empirical correction for index mismatch based on apparent distances measured for the crosstalk data. Since the crosstalk data was acquired on a different day (with a slightly different alignment of the optics) and samples z-space stochastically at only particular points, it may not correct the entirety of the bias for the other experiments. Finally, the difference may in part be explained by heterogeneity of chromatin compaction. This portion of their study only dealt with Chromosomes V, VI, and XIV while we looked at Chromosome II. It is worth noting that the absolute expected upper bound for the Euclidean distance between loci separated by 3 kbp on a completely uncompacted strand of DNA is ~1.02 μm, based on the classic 3.4 Å/bp. In any case, it is interesting to note that the distribution of $R_{DLSC\text{-}97kbp}$ is noticeably broader than those of $R_{DLSC\text{-}3kbp}$ and $R_{DLSC\text{-}12kbp}$.

Notably, in contrast to the DLSC strains, the inter-locus distributions of the DLDC and *GAL/PES4* cases are significantly more uniform over the range ~200 nm to ~1.5 μm, the upper bound of which corresponds roughly to the average radius of the diploid nucleus (Marshall et al., 1997). This uniformity is seen in the broadness of the PDFs (**Fig 3.3A**) and the linearity of the CDFs (**Fig 3.3B**). Moreover, there does not appear to be a very clear difference among the three of them and the average values of each distribution are remarkably similar: $\langle R_{DLDC\text{-}dextrose} \rangle$ = 749 ± 29 nm, $\langle R_{DLDC\text{-}galactose} \rangle$ = 746 ± 41 nm, and $\langle R_{GAL/PES4} \rangle$ = 752 ± 38 nm. These results suggest that on average there is not a strong preference for the colocalization of both copies of the *GAL* locus, regardless of transcriptional status. However, the mean value of 750 nm is about half the mean separation one would expect from two uncorrelated points distributed uniformly throughout a sphere of radius 1.5 μm, indicating a propensity for the two copies of each of the *GAL* locus and *PES4* to be within the same nuclear subvolume.

Velocity Cross-Correlations

Although transcriptional activation of the *GAL* loci (in galactose) did not seem to augment the likelihood of colocalization, we yet hypothesized that the same condition may drive an increase in correlated movements, perhaps through shared sites of transcription (Fraser and Bickmore, 2007). To test this hypothesis, we first developed a robust methodology to analyze the correlated movements of the distinctly-labeled loci in our various strains. When tracking with discrete time steps, one does not have access

Figure 3.3

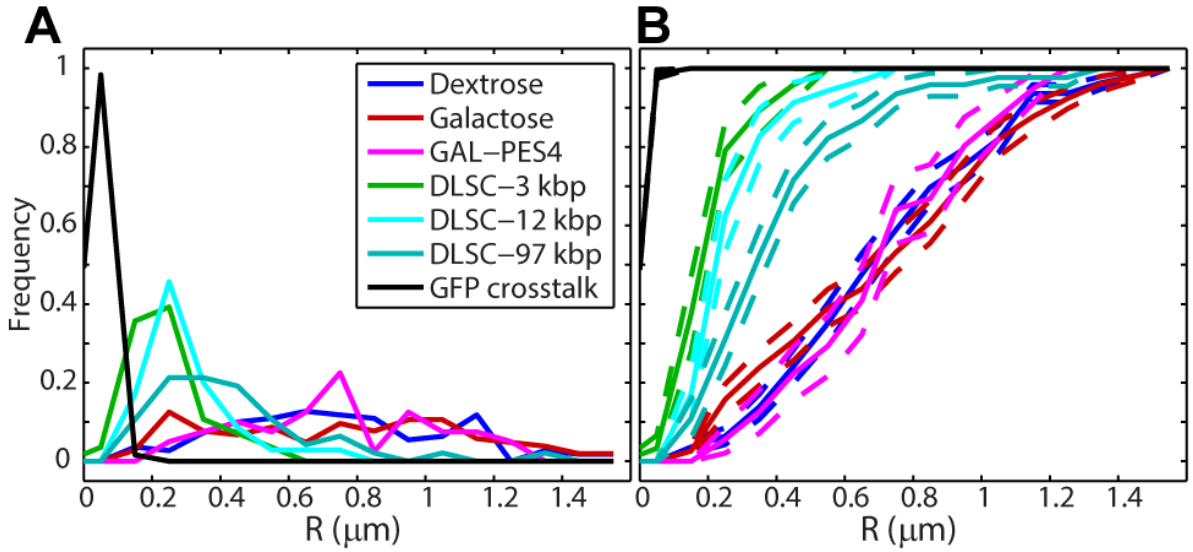

Figure 3.3: Distributions of inter-locus distances for each condition.
A. PDFs with 100-nm binning.
B. CDFs with 100-nm binning. Dashed lines give ± SE for each bin as determined from 100 bootstrapped samples.

to the true velocities of the particles, but rather the average velocities over a given time interval. The smallest such time interval possible δ_{min} is given by the inverse of the frame rate (δ_{min} = 0.1 s in our case). However, it is useful to define velocity more generally since more interesting information may emerge by looking at displacements over integer multiples of δ_{min}. Thus we define velocity parametrically by Eq. 1:

$$v_x^{(\delta)}(t_{i_n}) = \frac{x(t_{i_n}+\delta) - x(t_{i_n})}{\delta} \quad (1)$$

where t_{i_n} is the time of the i_nth frame of the nth track pair, and corresponding equations hold for the y and z dimensions. With this definition of velocity, we can define the components of the average velocity cross-correlation between the green (g) and red (r) channels as a time-dependent Pearson correlation coefficient via Eq. 2:

$$\rho_{v_x}(\delta,\tau) = \frac{\left\langle v_{x,g}^{(\delta)}(t_{i_n}) v_{x,r}^{(\delta)}(t_{i_n}+\tau)\right\rangle - \left\langle v_{x,g}^{(\delta)}(t_{i_n})\right\rangle \left\langle v_{x,r}^{(\delta)}(t_{i_n})\right\rangle}{SD\left(v_{x,g}^{(\delta)}(t_{i_n})\right) SD\left(v_{x,r}^{(\delta)}(t_{i_n})\right)} \quad (2)$$

where SD denotes the standard deviation of the variable in parentheses and corresponding equations hold for y and z. We equate the total velocity cross-correlation ρ_v as the average value of those of the three individual dimensions. Note that we have a choice in calculating the averages denoted by the angle brackets and implicit in the SDs of Eq. 2. If we simply average over i_n separately for each individual track pair n, then we obtain the full distribution of the ensemble of time-averaged velocity cross-correlations (TAVCC). If we instead sum over all i_n *and* all n before dividing by the total number of terms we get a time-ensemble-averaged velocity cross-correlation (T-EAVCC), which can have superior statistics due to increased averaging but does not allow access to the full distribution. We address both the TAVCC and the T-EAVCC here. Note that given sufficient averaging, the subtracted term in the numerator of Eq. 2 should evaluate to 0. However, we chose to leave it in our calculation since for short tracks a large random step in one channel could falsely inflate the correlation otherwise. Note that the denominator of Eq. 2 is proportional to the geometric mean of the mean square displacements (MSDs) in the two channels. We include this factor in order to scale away any differences in the calculated cross-correlation between different conditions that might arise simply because the loci are more mobile in one condition than in another. For instance, since the MSD of the *GAL* locus in dextrose is larger than that in galactose (Cabal et al., 2006), not including the denominator in Eq. 2 would automatically inflate ρ_v in dextrose relative to that in galactose. Whether or not to include this effect in our calculation of ρ_v is somewhat subjective. Note that ρ_v as defined in Eq. 2 lies in the interval [-1,1]. However, the denominator of Eq. 2 contains extra terms due to finite localization error (see MSD and Velocity Autocorrelation section) and so the maximum ρ_v calculated will actually be less than 1.

We first consider the T-EAVCC version and its time-dependence. **Fig 3.4A & B** shows the time-ensemble-averaged version of ρ_v as a function of time lag τ for fixed values of δ = 1 s and δ = 5 s, respectively, for all conditions studied. Note that each plot consists of a positive peak at τ = 0 and a decay to near-zero on either side. This indicates that on average the velocity step occurring in the green channel at a given time is positively correlated with the velocity step occurring in the red channel at the same time. The discernable negative-going peaks at $\tau = \pm\delta$ in the crosstalk data is likely

Figure 3.4

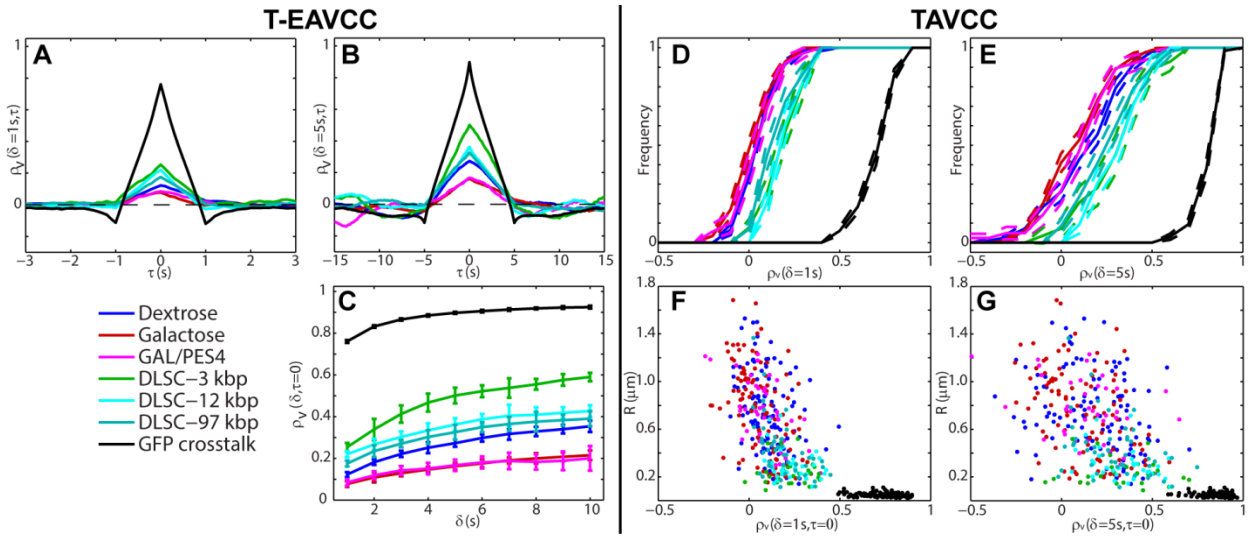

Figure 3.4: Statistics of ρ_v as calculated from both time-ensemble averaging (left of dividing line) and time averaging (right of dividing line).
A-B. ρ_v as a function of τ for fixed δ = 1 s (A) and δ = 5 s (B).
C. ρ_v as a function of δ for fixed τ = 0, calculated at 1-s intervals. Error bars indicate ± SE calculated from 10 bootstrapped samples of N track pairs.
D-E. CDFs of $\rho_v(\tau=0)$ for each condition for δ = 1 s (D) and δ = 5 s (E). Dashed lines give ± SE for each bin as determined from 100 bootstrapped samples.
F-G. Scatter plots depicting relationship between inter-locus distance and $\rho_v(\tau=0)$.

a consequence of the elasticity of the medium, which has been a well-documented effect for bacterial chromosomal loci (Weber et al., 2010). The deviations from zero at large $|\tau|$ for the other conditions in **Fig 3.4B** are due to diminished averaging at these points. Thus the most interesting point to focus on is at $\tau = 0$.

After careful inspection of the data, the first question to address is why each condition displays a positive peak at $\tau = 0$, even in the case of *GAL/PES4*. For one thing, it seems intuitively more reasonable to justify a persistent positive value than it is to justify a negative one. Positive correlations of chromatin movement have been in shown to persist in mammalian nuclei across 4-5 μm over the course of several seconds (Zidovska et al., 2013), and between opposite telomeres of certain budding yeast chromosomes (Bystricky et al., 2005). One can imagine a mechanism related to the entanglement of chromosome polymers or, perhaps, through force generation from the cytoskeleton (Heun et al., 2001; Koszul et al., 2008). On the other hand, persistent negative correlations would imply pulling apart of the chromosomes, an active and more exotic mechanism that to our knowledge has not been observed during interphase. Thus even a few track pairs that exhibit real positive correlation will not likely be opposed by a subpopulation exhibiting real negative correlations, resulting in a net positive correlation for the ensemble.

While positive correlations seem intuitively explicable by the above logic, we must also consider the possible effects of nuclear motion. During the time scale we studied (up to ~30 s), a previous report concluded that nuclear rotation was insignificant based on Fluorescence Recovery after Photobleaching (FRAP) data (Bystricky et al., 2005). However, many yeast chromatin tracking studies account for nuclear translations by staining the whole nucleus or nuclear envelope and subtracting its movements (Marshall et al., 1997; Cabal et al., 2006; Sage, 2005). We did not do so here since our two color channels were occupied by signal from the loci themselves. While we feel that nuclear translation should be less significant on our time scale than on the time scales typically employed in time lapse studies (>10 min), we cannot rule out its effects completely. Thus we emphasize that the main conclusions drawn from this study should rely on the *differences* between correlations across the conditions. Still, we think it's unlikely that nuclear motion can account for all of the positive correlations observed in even the *GAL/PES4* case since we observe individual track pairs whose TAVCC curves peak away from $\tau = 0$. This type of behavior seems to indicate a response time of the correlated movement that is not explicable by the global translation of the nucleus alone. We give an example of such behavior and explain the implications in more depth in the next section.

Notably, another striking feature of the plot in **Fig 3.4A** is the large separation between the upper limit set by the crosstalk data and the DLSC-3kbp case. This difference underscores the flexibility of the chromatin polymer. The discrepancy is reduced for larger δ (**Fig 3.4B**), since this segment of the polymer likely moves more like its center of mass over longer time intervals. In general, each case displays larger $\rho_v(\tau=0)$ for larger δ as the coordinated displacements become larger relative to the localization error. This is shown for δ between 1s and 10s in **Fig 3.4C**. There is also an apparent gulf between DLSC-3kbp and both DLSC-12kbp and DLSC-97kbp. This seems counterintuitive since DLSC-12kbp consists of loci that have genomic separation more similar to that in DLSC-3kbp than in DLSC-97kbp. This result may indicate that the

degree of compaction is highly heterogeneous even along this segment of a single chromosome, or that the locus separation in the DLSC-3kbp case is comparable to the fiber persistence length while that in the DLSC-12kbp is sufficiently large relative to this length. In any case, the ordering of ρ_v values makes sense in that among the DLSC cases, closer genomic and spatial separation means higher correlations, and that all the DLSC cases display higher correlations than the cases in which the loci are on separate chromosomes.

Importantly, biological implications of the preceding data include that the considerable flexibility of the chromatin fiber suggests that genes positioned in adjacent linear space may yet concurrently access distinct subnuclear domains, consistent with gene looping (de Laat and Grosveld, 2003; Fraser and Bickmore, 2007) and HiC data (Duan et al., 2010; Lieberman-Aiden et al., 2009). The same flexibility may also enhance or augment boundary activity by permitting genes to elude the spreading of proximal transcriptional activation or silencing (Meneghini et al., 2003; Ishii et al., 2002). Thus, *cis* or *trans* regulatory factors may alter the flexibility of the chromatin fiber in order to elicit the appropriate transcriptional response (Neumann et al., 2012).

Strikingly, parsing the DLDC and *GAL/PES4* data more closely reveals further interesting results. We see that the average DLDC-galactose correlations are essentially indistinguishable from our negative control, while the DLDC-dextrose correlations become more like those of the DLSC-97kbp case at larger δ, thus demonstrating a significant difference between the DLDC-dextrose and DLDC-galactose cases. Pulling numbers from **Fig 3.4B & C** we see that indeed at δ = 5 s and τ = 0, $\rho_{v,\text{DLDC-dextrose}} = 0.27 \pm 0.02$ is comparable to $\rho_{v,\text{DLSC-97kbp}} = 0.33 \pm 0.04$, and $\rho_{v,\text{DLDC-galactose}} = 0.16 \pm 0.02$ is in turn more similar to $\rho_{v,\textit{GAL/PES4}} = 0.16 \pm 0.03$ (mean ± SE calculated from 10 bootstrapped samples of N track pairs). To get an indication of the repeatability of these values we can inspect the T-EAVCC values of the three sets of DLDC-dextrose and two sets of DLDC-galactose separately. For δ = 2 s and τ = 0 we have $[\rho_{v1}, \rho_{v2}, \rho_{v3}] = [0.19 \pm 0.04, 0.17 \pm 0.02, 0.18 \pm 0.02]$ for the DLDC-dextrose case and $[\rho_{v1}, \rho_{v2}] = [0.11 \pm 0.02, 0.11 \pm 0.02]$ for DLDC-galactose, indicating excellent repeatability despite only a modest disparity between the conditions for this smaller δ. For δ = 5 s and τ = 0 we have $[\rho_{v1}, \rho_{v2}, \rho_{v3}] = [0.27 \pm 0.03, 0.28 \pm 0.03, 0.23 \pm 0.07]$ for the DLDC-dextrose case and $[\rho_{v1}, \rho_{v2}] = [0.13 \pm 0.04, 0.17 \pm 0.02]$ for DLDC-galactose, indicating reasonable repeatability in each. Note that for δ = 5 s the DLDC-dextrose set with the lowest ρ_v is also the set with the lowest N (= 20) value overall and thus the highest error in the mean. **Fig 3.4C** shows that the gap between DLDC-dextrose and DLDC-galactose widens as δ increases. However, the agreement among sets within each case becomes less convincing at larger δ due to insufficient averaging.

Consequently, although we originally hypothesized that transcriptional activation would confer heightened correlative motion, our data instead suggests, at least for the *GAL* locus, that repression (in dextrose) increases such movements relative to activating conditions (in galactose). This increase in correlative motion could be induced through shared factors responsible for transcriptional repression of the *GAL* loci, including Gal80 and Mig1 (Johnston et al., 1994). Conversely, if the correlative motion in dextrose represents the actual baseline of such motion between the two *GAL* loci, this would indicate that activation in galactose impedes correlative movement. This would be supported, for instance, if the individual *GAL* loci associate with distinct

nuclear pores upon transcriptional activation (Casolari et al., 2004; Cabal et al., 2006; Green et al., 2012). More experiments are necessary, however, to elucidate the true drivers and impediments of correlative motion.

Next, we consider the time-averaged version of ρ_v (TAVCC), which allows us to access the ensemble distributions of correlations for each condition. The resulting CDFs for δ = 1 s and 5 s are given in **Fig 3.4D & E**, respectively. Again we see a significant gap between the crosstalk data and the DLSC data, and between the DLSC data and the separate chromosome data. The difference between DLDC-dextrose and DLDC-galactose is less readily apparent than in the T-EAVCC. This is likely due to the fact that by only time-averaging each track pair and then binning the results, we are placing equal weight on shorter, noisier tracks as we are on longer, less noisy tracks. Noisy tracks will tend to have lower ρ_v since the denominator in Eq. 2 is larger. Thus the center of these distributions are deflated, which condenses the gap between the conditions. Shorter tracks will broaden these distributions, which also diminishes the gap between conditions.

Calculating the TAVCC for each track pair also allows us to examine the relationship between ρ_v and inter-locus distance R. This is illustrated in the scatter plots in **Fig 3.4F & G** for δ = 1 s and 5 s, respectively. Disregarding the crosstalk data, which is bunched at low R, we see the data seems to fall along a line with negative slope. We can quantify this apparent correlation by pooling the cases together and calculating the Pearson correlation coefficient (PCC) between the variables ρ_v and R. For δ = 1 s we get PCC = -0.57 ± 0.03 (mean ± SE determined from 100 bootstrapped samples); for δ = 5 s we get PCC = -0.46 ± 0.04. The presence of a negative correlation may arise due to an increased predisposition of loci that are closer together to become entangled with one another and pull each other around. This also speaks to the fact that our main results are likely not artifacts of nuclear translation, since a translation of the whole nucleus should translate all points within it by the same amount, at least by the same assumptions that allow one to subtract the motion of the nuclear center of mass as in other studies.

Interesting Single Track Pair Examples

During the course of our expiments we observed instances of fascinating behavior shared between distinct chromosomal loci. We therefore set out to further evalulate such notable examples. Importantly, our single-particle tracking approach allows us to highlight prominent track pairs that exhibit either high or low ρ_v. Data from one such highly correlated DLDC-dextrose example is shown in **Fig 3.5 A-D**. **Fig 3.5 A-C** show the x-, y-, and z-projections of the velocity trajectories in the green and red channel as calculated for δ = 5 s. The x- and z-projections of both loci appear to exhibit notable pseudo-oscillatory behavior (Pliss et al., 2013). Interestingly, however, there seems to be a phase lag between the pseudo-oscillations of the loci, as in this particular case the red-tagged locus leads the green-tagged locus. This fact is further demonstrated by calculating the TAVCC, which is plotted in **Fig 3.5D**. Here we see a large peak (>0.5) centered near τ = 2 s, indicating a ~2-s response time between the leading red locus and the lagging green locus. Of course, there is no biological reason why the red should always lead the green, and so the ensemble contains track pairs

Figure 3.5

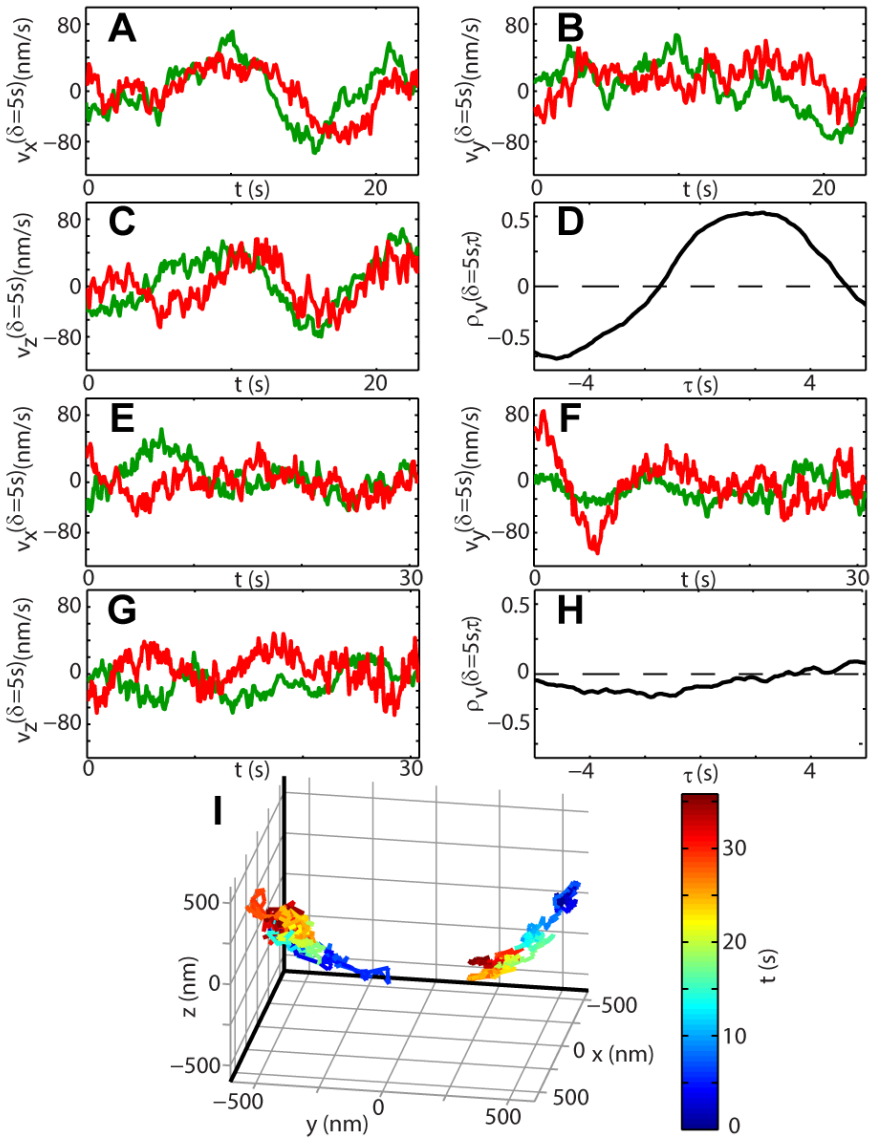

Figure 3.5: Data from two example track pairs.
A-C. Velocity trajectories of a highly correlated example from the DLDC-dextrose case in each dimension, for δ = 5 s. Green lines correspond to track from green fluorescence channel and red lines to track from red fluorescence channel.
D. The time-average velocity cross correlation of the same track pair as in (**A-C**).
E-G. Same as in (**A-C**) but for a different track pair from the DLDC-galactose case, which exhibits low correlations.
H. Same as in (**D**) but for the track pair addressed in (**E-G**).
I. 3D position trajectories of loci from (E-H), color coded in time.

which show the reverse relation just as often, giving rise to the symmetric T-EAVCC shown in **Fig 3.4A & B**.

Fig 3.5 E-I depicts an example track pair from the DLDC-galactose condition with particularly low correlations. No obvious qualitative relation between the velocity trajectories is apparent in **Fig 3.5 E-G** as it was for the previous example. This is quantified by the relatively flat TAVCC curve in **Fig 3.5H**. **Fig 3.5I** shows the 3D position trajectories traced by this locus pair color coded with time. The plot is rotated to a particularly suggestive vantage from which the two loci appear as though they follow the curvature of the nucleus, as has been reported previously when the *GAL* locus becomes associated with factors of the NPC (Cabal et al., 2006). Strikingly, the two loci appear to be associated at distinct regions of the envelope. We also saw examples of locus pairs that qualitatively seemed to associate at overlapping regions of the envelope, and some in which one locus seemed to associate with the periphery while the other did not. However, the identification of peripheral association by track curvature is admittedly subjective, and more careful quantitation must be done by labeling the periphery in a third color, for example, before any strong conclusions can be made on this observation.

In conclusion, by using the DH-PSF microscope we were able to simultaneously track pairs of fluorescenctly labeled chromosomal loci in diploid budding yeast with high precision in 3D on a time scale of ~0.1 s-30 s. This technique also gave access to the correlations in motion between loci: for one, correlations between loci located on the same chromosome demonstrated considerable flexibility of the chromosome fiber. Furthermore, the two copies of the *GAL* locus exhibited higher correlations when in a repressive environment than when in an activating one. Under repressive conditions, the correlations between *GAL* loci resembled those of two loci separated by 97 kbp along the same chromosome, while under activating conditions *GAL* loci correlations were equivalent to those evinced by distinct gene loci located on different chromosomes. Inspection of individual track pairs suggests a wealth of interesting behavior, such as finite response times of correlative motion and the interplay between association with the nuclear envelope and the degree of correlations. However, more quantitation is needed to fully elucidate these observations. Our results highlight the utility of single-pair tracking as a complementary tool to static imaging, conformation capture techniques, and single-particle tracking for the study of epigenetics. Future studies should conduct pair tracking with concurrent colocalization to nuclear landmarks, since these may play a role in sequestering groups of genes and exerting forces on them. Future studies should also examine correlations between multitudes of pairs of loci spanning the full range of genomic distances. While our wide-field technique did allow for a considerable improvement in throughput over confocal scanning methods (from tens to hundreds of cells), further automation of the analysis will allow for truly high-throughput studies.

Materials and Methods

Strain Construction and Growth

All strains utilized in this study are of the S288c (BY4743) background (**Table 3A**). Cells were grown at room temperature (~22ºC) to early-to-mid log phase in synthetic complete (SC) media containing 2% Dextrose or 2% Galactose where indicated. Care was taken to maintain the cells in early-to-mid log phase for an extended period before imaging.

Microscopy

Cells were spun down and mixed with a diluted solution (~100x from stock into either dextrose or galactose/cell media solution) of multi-color 0.1-μm fluorescent fiducial beads (TetraSpeck, Invitrogen, Carlsbad, CA) before being mounted on a 1% agarose (Sigma-Aldrich, St. Lousi, MO) pad. The bead stock contained some amount of azide, a known decoupler (Heun et al., 2001). However, the final concentration of azide was ≤ 10^{-4} %, roughly two orders of magnitude lower than typically administered lethal amounts. The cells appeared to grow normally overnight when left in the presence of this final dilution of bead solution. Once on the agarose pads, the cells were sandwiched with another coverslip and the edges were sealed with wax. Slides were then mounted on a modified inverted microscope stand (Nikon Diaphot 200) in which the internally mounted tube lens had been removed and replaced with a lens just outside the body of the stand. Cells were illuminated with a 488 nm laser (CrystaLaser, Reno, NV) at ~45 W/cm^2 and a 561 nm laser (Sapphire, Coherent, Inc., Santa Clara, CA) at ~25 W/cm^2. Fluorescence was collected using one of two microscope objectives: an NA-1.40 oil-immersion objective (UPlanSApo 100X/1.40NA Oil, Olympus, Tokyo, Japan) and a super-corrected objective (PlanoApoN 60X/1.40NA Oil SC, Olympus, Tokyo, Japan). The super-corrected objective was used in some later data sets in an attempt to improve registration accuracy, but it did not seem to make a noticeable difference. In order to maintain the magnification of the original system, the tube lens was replaced with a designed train of lenses once the super-corrected objective was installed. Collected fluorescence traveled through a multi-bandpass dichroic mirror (zt405/488/561rpc, Chroma Technology, Rockingham, VT) within the microscope stand. After the tube lens/es, the light was passed through a dual-channel 4*f* optical processing system which served to convolve the standard PSF with the DH-PSF as described in detail elsewhere (Gahlmann et al., 2013). The fluorescence was filtered through a 561 notch filter (NF03-561E, Semrock, Rochester, NY) and a dual-bandpass filter (Brightline Multiband 523/610, Semrock, Rochester, NY) before being split into two color channels by a 560 nm dichroic beam splitter (FF560-FDi01, Semrock, Rochester, NY). The red channel was further filtered through a 600 nm long pass filter (E600LP, Chroma Technology, Rockingham, VT) in order to reduce GFP crosstalk. This long pass was removed for the haploid crosstalk tracking experiments. The DH-PSF in each color channel was produced through the use of quartz transmission phase masks designed for the yellow and red regions, respectively. The color channels were imaged simultaneously onto separate regions of an EMCCD camera (Ixon DU-897E, Andor

Table 3A: Yeast strains used in this study.

Strain #	Genotype	Source
KWY 3915	*MATα ybr022w::112TetO::URA3 leu2::TetR-3XmCherry::LEU2*	This Study
KWY 3926 (Crosstalk)	*MATa ybr022w::256LacO::LEU2 his3::LacI-GFP::HIS3*	This Study
KWY 3940 (DLDC)	*MATa/α his3::LacI-GFP::HIS3/his3Δ1 leu2Δ0/leu2::TetR-3XmCherry::LEU2 ybr022w::256LacO::LEU2/ybr022w::112TetO::URA3*	This Study
KWY 4339 (*GAL*/*PES4*)	*MATa/α his3::LacI-GFP::HIS3/his3Δ1 leu2Δ0/leu2::TetR-3XmCherry::LEU2 YBR022W/ybr022w::112TetO::URA3 yfr023w::256LacO::LEU2 /YR023W*	This Study
KWY 4089 (DLSC1)	*MATa/α ybr022w::112TetO::URA3/YBR022W his3::LacI-GFP_TetR-3XmCherry::HIS3/his3Δ1 ybr021w::256LacO::LEU2/YBR021W*	This Study
KWY 4087 (DLSC2)	*MATa/α ybr022w::112TetO::URA3/YBR022W his3::LacI-GFP_TetR-3XmCherry::HIS3/his3Δ1 ybr028c::256LacO::LEU2/YBR028C*	This Study
KWY 4772 (DLSC3)	*MATa/α ybr022w::112TetO::URA3/YBR022W his3::LacI-GFP_TetR-3XmCherry::HIS3/his3Δ1 ybr071w::256LacO::LEU2/YBR071W*	This Study

All strains are of the S288c (BY4743) background with genotype:

*MAT*a/α *his3Δ1/his3Δ1 leu2Δ0/leu2Δ0 LYS2/lys2Δ0 met15Δ0/MET15 ura3Δ0/ura3Δ0*

Technology, Belfast, Northern Ireland) operating at a maximal gain level of 300. An appropriate field-of-view for dual-color tracking was found by searching for a region of cells in which the GFP-labeled loci were within the same depth-of-focus (~2 μm) as the fiducial beads located at the coverslip Then image stacks were recorded at 10 Hz according to the following procedure: record a few seconds with only the 488 nm laser on to assess the degree of GFP crosstalk before dual-color tracking, perform dual-color tracking with both lasers on until the red signal bleached into the background, then again record a few seconds with only the 488 nm laser on to assess the degree of GFP crosstalk after the bleaching of the red fluorophores. This procedure allowed us to throw out tracks for which GFP crosstalk might cause obvious artifacts, and to carefully bound the effect in more subtle cases. The lasers were then both turned off and a white light image stack of the field was taken to make sure the cells were stationary on the relevant time scale and to identify cell cycle phase of each analyzed cell. Only loci from cells identified as being in G1 phase were included in the final analysis.

Analysis

Each image stack was analyzed by identifying loci and fiducial beads by hand. Custom MATLAB (MathWorks, Natick, MA) tracking software was then used to estimate position of each identified object in each frame by least-squares fitting to a sum of two 2D Gaussian functions plus a constant offset. The amplitudes and widths of each Gaussian and the constant offset were the parameters of the fit. Fiducial trajectories were smoothed by convolving with a 15-frame temporal boxcar function in order to suppress the propagation of bead localization error in later drift compensation. Locus trajectories were then filtered by having the user inspect each resulting position and velocity trajectory individually and resetting thresholds and/or rejecting frames in which clear fitting artifacts were present. After this step, the user visually compared each fitted double-Gaussian to the raw images of the locus through the first and last 50 frames in order to reject any persisting fitting artifacts (e.g. fitting of the background in cells with high nuclear background). We then transformed the locus trajectories from the red channel in to the coordinates of the green channel. The transformation map was found by scanning a sample of 0.1-μm orange fluorescent beads (Fluospheres, Invitrogen, Carlsbad, CA) immobilized at an interface in 1% polyvinyl alcohol (Polysciences, Inc., Warrington, PA) through a 3D volume and then using the algorithm detailed in reference (Gahlmann et al., 2013). In order to best approximate the media of the cell imaging, the fluorescent bead sample of the registration method was topped with either water or an agarose pad. Still, since the beads could not be scanned away from the interface, the media mimicry was only approximate, resulting in a residual z-dependent registration error for which we compensated empirically. No additional compensation for index of refraction mismatch was applied since the subdiffusion parameters of the z component of the mean square displacements (MSDs) did not seem to differ from those of the x and y components in any repeatable way, likely because the z-distance traversed during the time scale studied was not large enough on average to make the apparent z-distortion very significant. After transformation, the locus trajectories were corrected for stage drift as inferred from fiducial tracks.

Acknowledgements

We thank Tom Lampo and Prof. Andrew Spakowitz for helpful discussions and Nate Krefman for the TetR-3XmCherry construct. M. P. B. was supported by a Robert and Marvel Kirby Stanford Graduate Fellowship. This work was supported by the National Institute of General Medical Sciences grant 2R01GM085437 (to W. E. M.) and the National Institute of Health grant R01GM058065 (to K. W.).

Chapter 4:

A conserved starvation response confines the mobility of chromatin and other macromolecules

Background

Eukaryotic cells expend a significant amount of energy to establish and maintain a high degree of intracellular organization to regulate and orchestrate their complex metabolism. This includes the active enrichment of macromolecules into organelles, which in turn allows for the separation of biochemical pathways and enhances their efficiency by increasing local concentrations of enzymes and metabolites. Similarly, active transport by motor proteins on the cytoskeleton enables large eukaryotic cells to overcome the limits of Brownian motion in which the diffusion time scales with the square of the distance. Nevertheless, many cellular pathways and biochemical interactions are critically dependent on thermal diffusion. Much research has therefore been performed to characterize diffusional processes that occur within eukaryotic cells. These studies have revealed that the very complex and extremely crowded cytosol of eukaryotic cells cannot be simply viewed as an ideal liquid but, instead, can be modeled as a polymer gel (Luby-Phelps, 2000; Clegg, 1984; Knull and Minton, 1996) or soft colloidal glass (Fabry et al., 2001; Mandadapu et al., 2008; Luby-Phelps, 2000). Still, a comprehensive understanding of the biophysical properties of eukaryotic cells is lacking and it remains poorly understood how these characteristics influence macromolecular movement. Furthermore, little is known about the biological determinants of intracellular diffusion including whether cells functionally regulate their diffusional properties in response to changes in growth conditions or the environment.

A particularly well-studied model of intracellular movement is the motion of chromatin in the nucleus. Various groups have analyzed chromatin mobility but a coherent mechanistic understanding of this process has yet to emerge (reviewed in Hübner and Spector, 2010). For example, it was shown that chromosomes wiggle in a manner consistent with constrained diffusion and it was proposed that chromosome movement results from Brownian motion rather than from active motility (Marshall et al., 1997). In contrast, other studies have suggested that chromatin movement is ATP dependent (Heun et al., 2001), and it was hypothesized that chromatin movement is driven by a multitude of ATP-dependent processes along the length of the chromosome (Neumann et al., 2012). Similarly, the role of the cytoskeleton in chromatin movement has remained controversial, and both microtubule-dependent and –independent movement was reported (Heun et al., 2001, Marshall et al., 1997). Several recent studies have also implicated the actin cytoskeleton in chromatin mobility (Chuang et al., 2006; Koszul et al., 2008; Spagnol and Dahl, 2014).

To better characterize the diffusional properties of eukaryotic cells, we have analyzed here the movement of chromatin and mRNPs in budding yeast under changing growth conditions. Interestingly, our results demonstrate that cells fundamentally change their biophysical properties in response to glucose starvation, which leads to a dramatic confinement of large macromolecules. This effect cannot be explained by changes in ATP levels but is brought about by an intracellular phase transition induced by molecular crowding through a loss of cell volume. This response seems to be evolutionarily conserved, as bacteria similarly restrict macromolecular mobility in response to starvation (Parry et al., 2014), and we show here that starvation also induces a volume loss in bacterial cells. Our results suggest a novel mechanism by

which cells regulate their biophysical properties in order to adapt to environmental stress.

Results

Glucose starvation limits macromolecular mobility in the nucleus and cytoplasm

To better characterize nuclear chromatin dynamics in budding yeast we analyzed the movement of various gene loci in changing growth conditions. LacO repeats were integrated at the *POA1* locus on chromosome II, the *URA3* locus on chromosome V, and on a centromeric plasmid (pLacO). Co-expression of LacI-GFP allowed us to visualize these three distinct loci and track their mobility over minute-long sequences. Whereas several changes in growth conditions had no obvious effect on chromatin mobility (data not shown), acute glucose starvation induced a dramatic cessation of chromatin movement. Cumulative track projections demonstrated a significant reduction in the volume explored by all three loci in cells acutely starved for glucose (**Fig 4.1A**). This suggests that chromatin mobility is regulated by the presence of glucose.

To quantify the dramatic changes in chromatin mobility, we calculated ensemble averaged mean squared displacements (MSDs) for all chromatin loci (n = ~200-1000 trajectories each). These express the magnitude of diffusion for a given particle, quantifying the average displacement per unit time and are used to compute diffusion coefficients (Qian et al., 1991). We find that the massive confinement of chromatin upon glucose starvation (**Fig 4.1B & C; Fig 4.2A**) leads to an approximately fourfold reduction of the diffusion coefficient (D): for instance, D_{POA1} decreased from 0.0059 $\mu m^2/s$ to 0.0015 $\mu m^2/s$ upon starvation.

To analyze whether glucose starvation uniquely affects chromatin dynamics in the nucleus, or whether it also influences the mobility of other macromolecules, we imaged the movement of cytoplasmic mRNPs, which can be conveniently tracked as single particles (Shav-Tal et al., 2004). 24-PP7 stem-loops were integrated into the 3' UTR of *GFA1* and *FBA1*, essential genes involved in distinct processes (Lagorce et al., 2002; Schwelberger et al., 1989), and the movement of individual mRNPs was examined upon co-expression of the coat-binding protein, CP-PP7-3XYFP. Cumulative track projections revealed substantially higher mobility for mRNPs than chromosomal loci in glucose, which is expected given the significantly smaller size of mRNPs compared to chromosome fibers (**Fig 4.1D**) (Thompson et al. 2010; Zarnack and Feldbrügge, 2007). Yet, upon glucose starvation *GFA1* and *FBA1* mRNPs also exhibited a dramatic reduction in their mobility (**Fig 4.1E & F**). Removal of glucose led to a 3 to 4-fold decrease in the diffusion coefficient of both *GFA1* (D_{GFA1} reduced from 0.0296 $\mu m^2/s$ to 0.0101 $\mu m^2/s$) and *FBA1* (D_{FBA1} reduced from 0.0323 $\mu m^2/s$ to 0.00779 $\mu m^2/s$) mRNPs, a value which is similar to the relative change that we had observed in the diffusion of chromatin. These effects were not a consequence of extensive washes as a depletion of glucose through growth into quiescence also confined the mobility of mRNPs (**Fig 4.2B & C**). Thus, glucose starvation prompts a dramatic confinement of macromolecules in the nucleus as well as the cytoplasm.

Figure 4.1

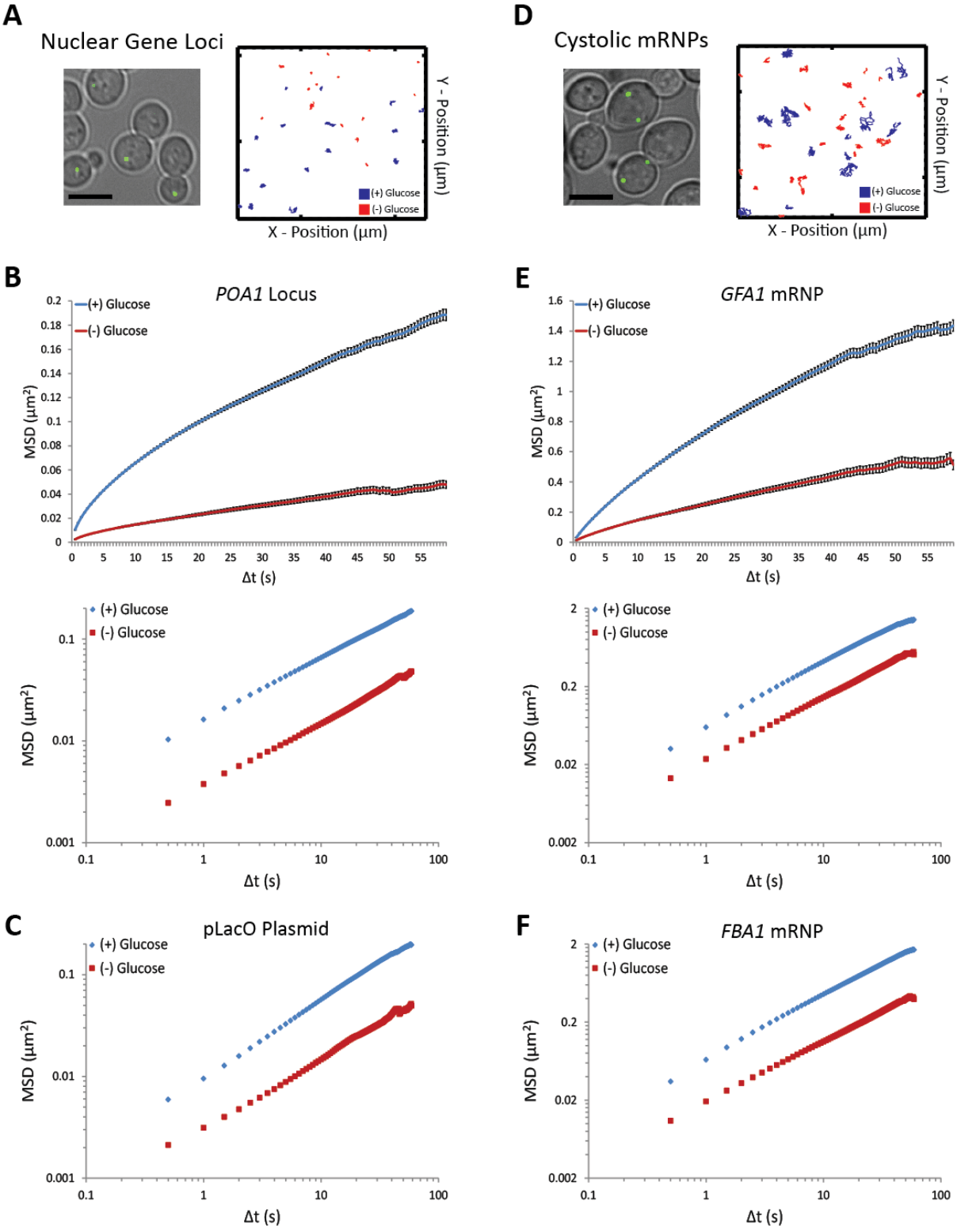
A
Nuclear Gene Loci
Y - Position (µm)
X - Position (µm)
(+) Glucose
(-) Glucose
D
Cystolic mRNPs
B
POA1 Locus
MSD (µm²)
Δt (s)
E
GFA1 mRNP
C
pLacO Plasmid
F
FBA1 mRNP

Figure 4.1: Glucose starvation confines macromolecular mobility in the nucleus and cytoplasm.
A. Chromatin mobility was analyzed in strains harboring 256-LacO repeats at *POA1* (shown), *URA3*, or on a centromeric plasmid (pLacO) and LacI-GFP. Left panel: Typical LacI-GFP signal superimposed on a phase image. Scale bar is 6μm. Right panel: Minute-long trajectories (0.5 second frame rate) of the *POA1* locus from both (+) glucose (blue) and (-) glucose (red) conditions projected in the same frame for direct comparison. Log-growing cells were acutely starved for glucose and imaged after thirty-minutes.
B. Quantification of *POA1* mobility into a mean squared displacement (MSD). Upper panel: Individual MSDs (n=~200-1000) were compiled and ensemble-averaged into an aggregate MSD for each condition. Error bars represent SEM. Lower panel: Log-log plot of aggregate MSDs revealing the parallel temporal evolution of the MSDs despite the confinement of mobility in the (-) glucose condition.
C. Quantification of pLacO mobility during log-growth and after thirty minutes of acute starvation displayed as a log-log MSD plot.
D. mRNP mobility was analyzed in strains harboring integrations of 24-PP7 stem-loops into the 3'UTR of *GFA1* (shown) or *FBA1* and expressing 3xYFP-CP-PP7. Left panel: Typical 3xYFP-CP-PP7 signal superimposed on a phase image. Scale bar is 6μm. Right panel: Minute-long trajectories (0.5 second frame rate) of the *GFA1* mRNP from both (+) glucose (blue) and (-) glucose (red) conditions projected in the same frame for direct comparison. Log-growing cells were acutely starved for glucose and imaged after thirty-minutes.
E. Quantification of *GFA1* mRNP mobility into a mean squared displacement (MSD). Upper panel: Individual MSDs (n=~200-1000) were compiled and ensemble-averaged into an aggregate MSD. Error bars represent SEM. Lower panel: Log-log plot of aggregate MSDs revealing the parallel temporal evolution of the MSDs despite the confinement of mobility in the (-) glucose condition.
F. Quantification of *FBA1* mRNP mobility during log-growth and after thirty minutes of acute starvation displayed as a log-log MSD plot.

Figure 4.2

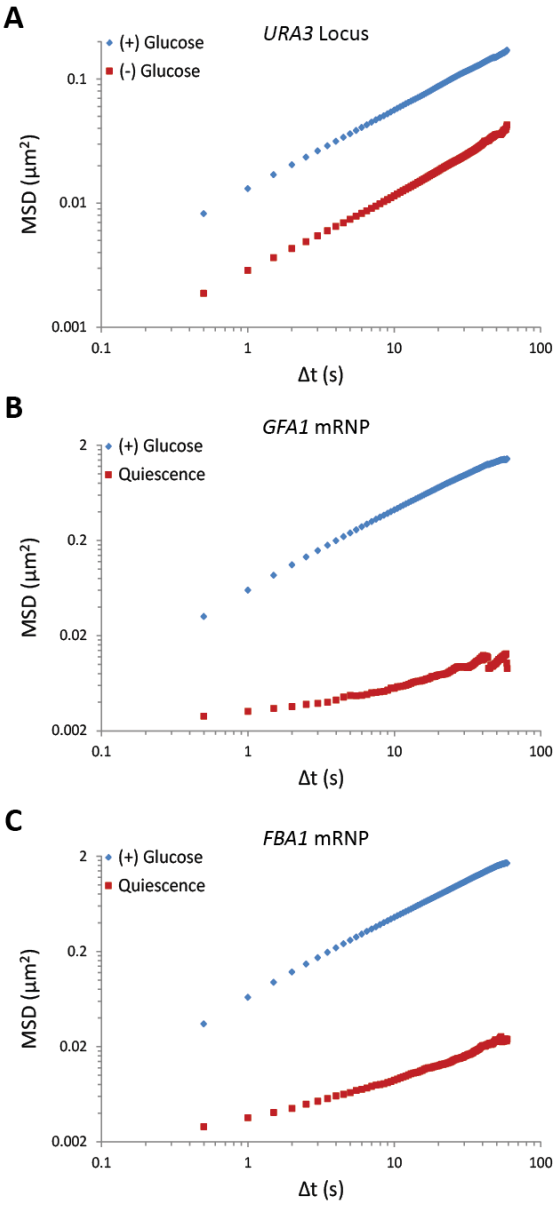

Figure 4.2: Starvation confines macromolecular mobility.
A. Quantification of *URA3* mobility during log-growth and after thirty minutes of acute starvation displayed as a log-log MSD plot.
B. Quantification of *GFA1* mRNP mobility during log-growth and quiescence (see **Materials and Methods)** displayed as a log-log MSD plot.
C. Quantification of *FBA1* mRNP mobility during log-growth and quiescence displayed as a log-log MSD plot.

Starvation arrests cytoskeletal dynamics, which constrains chromatin mobility but has little effect on mRNPs

mRNPs can be actively transported by motor proteins along the cytoskeleton and both the actin cytoskeleton and microtubules were reported to influence chromatin dynamics (Thompson et al., 2010; Heun et al., 2001; Koszul et al., 2008; Spagnol and Dahl, 2014). Interestingly, actin filaments were also shown to rapidly depolymerize upon starvation (Uesono et al., 2004; Sagot et al., 2006). We therefore wanted to explore whether the starvation-induced confinement of macromolecular mobility resulted from changes in cytoskeletal dynamics. Indeed, phalloidin staining of yeast cells starved for glucose demonstrated that actin filaments are ablated in nearly all cells, and the actin distribution instead appeared dotted indicating an abundance of actin patches (**Figure 4.3A**).

If the changes in the mobility of chromatin or mRNPs upon glucose withdrawal were due to the observed effects on cytoskeletal dynamics, we would predict that drug-induced inhibition of actin should mimic the starvation response. In order to test this hypothesis, we treated cells with the actin depolymerizer, Latrunculin-A (LatA) (Ayscough et al., 1997). Indeed, treatment with Latrunculin-A reduced chromatin movement, although the effect was insufficient to mimic the confinement of chromatin during starvation (**Fig 4.3B**; **Fig4.4B & C**). However, because chromatin mobility is reported to be affected by microtubule dynamics (Heun et al., 2001), we also treated cells with the microtubule depolymerizing drug, nocodazole (Jacobs et al., 1988). Astonishingly, treatment with nocodazole reduced chromatin movement in an additive manner to LatA and concurrent addition of LatA and nocodazole substantially reduced chromatin mobility (**Fig 4.3B**; **Fig4.4B & C**). Moreover, log-log MSD plots indicate that the effect of inhibiting the cytoskeleton is most apparent at later time points and, in addition, may augment the anomalous behavior of chromatin motion (**Fig 4.3B**; **Fig4.4B & C**).

The actin and microtubule cytoskeleton could either act on chromatin itself or affect chromatin mobility indirectly by influencing overall nuclear motion. To differentiate between these two possibilities, we next imaged a strain in which two chromosomal loci (*POA1*, chromosome II and *PES4*, chromosome VI) were labeled simultaneously, and tracked the distance between the two loci over time (**Fig 4.4D**). This approach allows for the exclusive quantification of intranuclear movements because translational changes in the positioning of the nucleus affect both loci identically and thus do not influence intranuclear distance measurements (Marshall et al., 1997). This two-locus analysis confirmed the LatA and nocodazole-induced reduction in chromatin mobility as the interchromosomal distance between the two loci, compiled as mean-squared displacements, still decreased considerably with simultaneous drug treatment (**Fig 4.4E & F**). Of note, however, this result cannot differentiate between cytoplasmic or nuclear cytoskeletal dynamics in modulating chromatin mobility. We conclude that the mobility of yeast chromatin is markedly affected by the dynamics of the cytoskeleton and that the actin and microtubule cytoskeleton independently contribute to the movement of chromatin.

Notably, in contrast to chromatin, the two inhibitors of cytoskeletal dynamics had little effect on mRNP mobility when utilized individually and only a moderate effect when

Figure 4.3

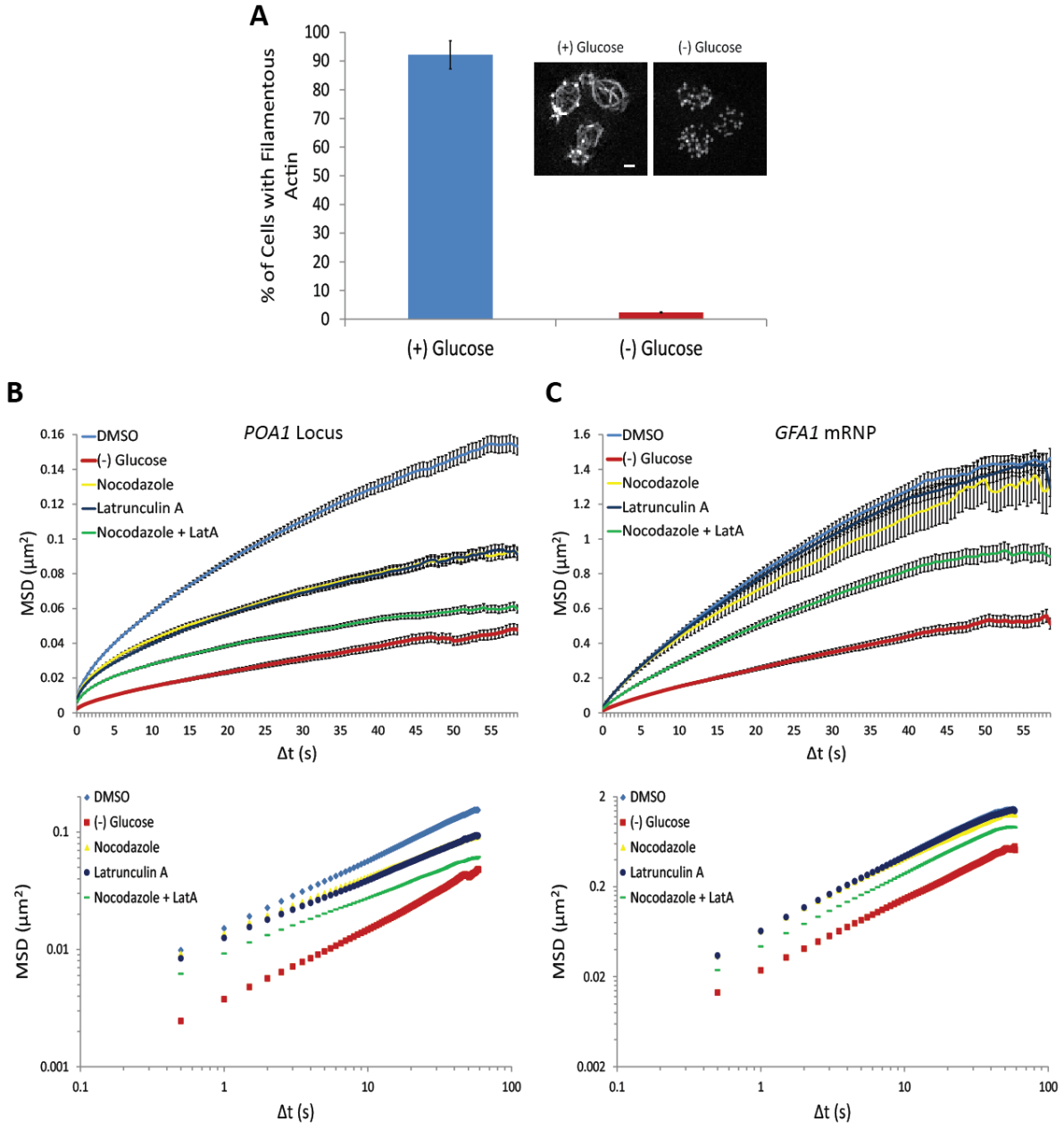

Figure 4.3: Starvation confines cytoskeleton-independent mobility as well as mobility influenced by the cytoskeleton.
A. Quantification of filamentous actin during log-growth, (+) glucose, and after acute starvation, (-) glucose. Cells were fixed and stained with phalloidin. Z-stack projections were then processed and blinded and cells classified based on the presence or absence of filamentous actin. Insert contains representative images after processing. Scale bar is 1µm. Error bars are SEM for 3 biological replicates (n = 350-800 cells).

B. Mobility of the *POA1* locus is significantly dampened after inhibition of the cytoskeleton. Cells were treated with nocodazole and/or Latrunculin-A (LatA) for 20 minutes prior to imaging. Upper panel: Quantification of *POA1* mobility into MSDs. Error bars represent SEM. Lower panel: Log-log MSD plot revealing a dissimilar slope of the (-) glucose MSD compared to the MSDs of the drug treatments.
C. The mobility of the *GFA1* mRNP is only moderately reduced upon concurrent treatment with nocodazole and LatA. Cells were treated as described in (**B**). Upper panel: Quantification of *GFA1* mRNP mobility into MSDs. Error bars represent SEM. Lower panel: Log-log MSD plot of the same data. Drug treatments do not affect the slope of the *GFA1* mRNP MSD.

Figure 4.4

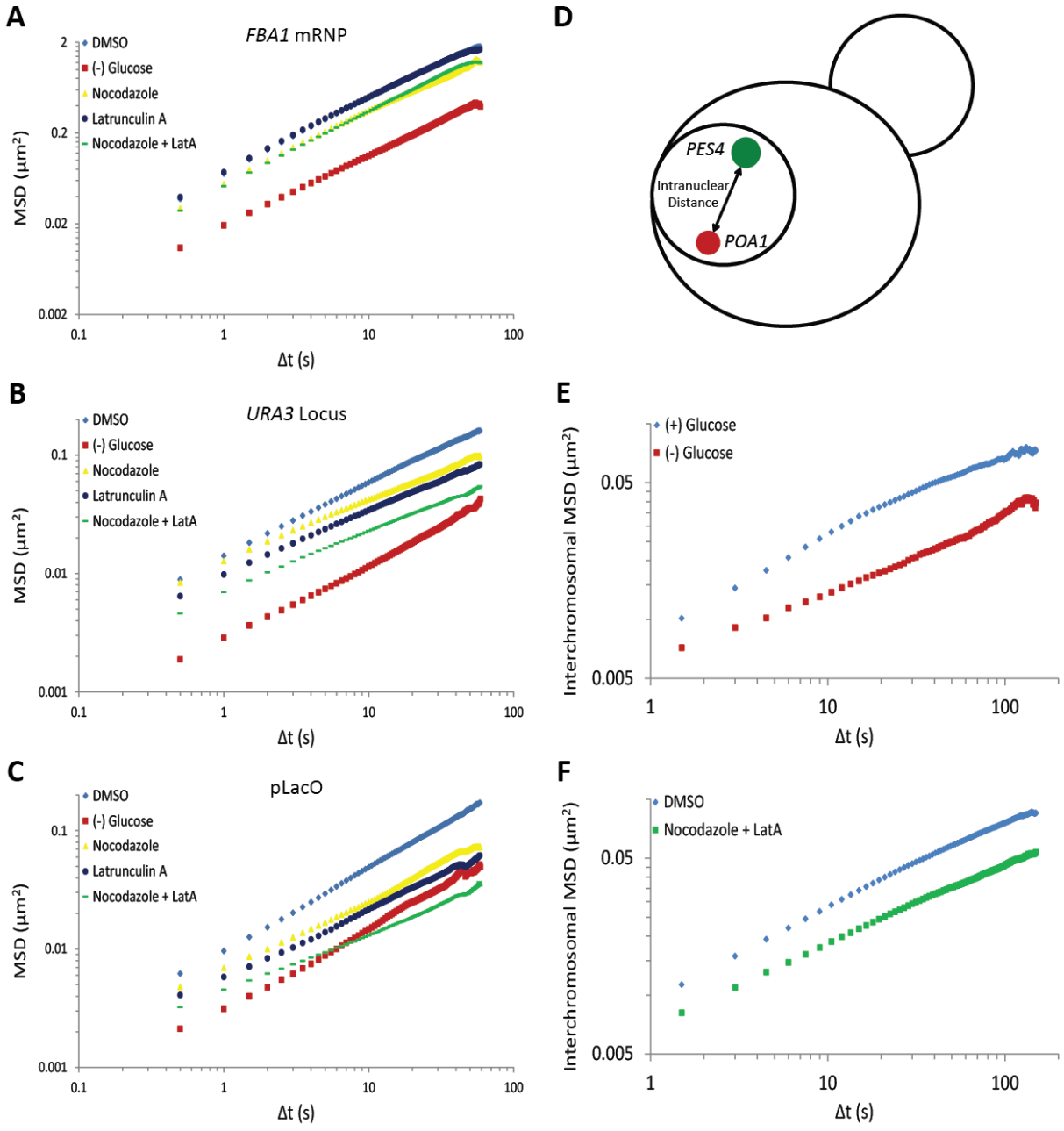

Figure 4.4: Starvation confines the cytoskeleton-independent mobility of mRNPs and the cytoskeleton-influenced mobility of chromatin.
A. The mobility of the *FBA1* mRNP is only slightly reduced upon concurrent treatment with nocodazole and LatA. Cells were treated as described in (**Fig 4.3B**) and the mobility of the *FBA1* mRNP was quantified and displayed as a log-log MSD. Drug treatments do not affect the slope of the *FBA1* mRNP MSD.
B. Mobility of the *URA3* locus is significantly decreased after inhibition of the cytoskeleton. Cells were treated as described in (**Fig 4.3B**) and the mobility of the

URA3 locus was quantified and displayed as a log-log MSD. The plot indicates a dissimilar slope of the (-) glucose MSD compared to the MSDs of the drug treatments.
C. Mobility of pLacO is substantially decreased after inhibition of the cytoskeleton. Cells were treated as described in (**Fig 4.3B**) and the mobility of pLacO was quantified and displayed as a log-log MSD. The plot indicates a remarkably dissimilar slope of the (-) glucose MSD compared to the MSDs of the drug treatments.
D. Graphic depicting the quantification of specifically intranuclear movements by tracking the displacement between the *POA1* locus (red) and the *PES4* locus (green).
E. Log-log interchromosomal MSDs quantifying the displacement between *POA1* and *PES4* during log-growth, (+) glucose, and after thirty minutes of acute starvation, (-) glucose. Sequential excitations/emissions of LacI-GFP and TetR-3xmCherry were acquired every 1.5 seconds for a total of 150 seconds. The time-lapsed displacement between the two loci was then compiled into an MSD.
F. Log-log interchromosomal MSDs quantifying the displacement between *POA1* and *PES4* after inhibition of the cytoskeleton (Nocodazole + LatA) and in the DMSO control. Cells were treated as described in (**Fig 4.3B**).

used concurrently (**Fig 4.3C**; **Fig 4.4A**). As both drugs did inhibit chromatin dynamics (**Fig 4.3B**; **Fig4.4B & C**) and growth (data not shown), this result demonstrated that the mobility of the *GFA1* and *FBA1* mRNPs is largely independent of the cytoskeleton. Our results, therefore, could be explained by two alternative models: 1) starvation confines macromolecular mobility through multiple, distinct mechanisms, or 2) a singular, starvation-induced pathway restricts the mobility of both classes of macromolecules. Consistent with this, although inhibition of the cytoskeleton substantially reduces chromatin mobility, the remaining motion is, nevertheless, dissimilar to that of glucose-starved cells, suggesting an additional mechanism of confinement during starvation (**Fig 4.3B**; **Fig4.4B & C**). Thus, because both mRNP and chromatin movement is confined during starvation, we conclude that glucose starvation restricts cytoskeleton-independent mobility as well as the mobility of macromolecules influenced by the cytoskeleton.

Reduction of ATP is insufficient to explain the macromolecular confinement

Since the acute withdrawal of glucose in fermenting yeast cells is expected to have a significant impact on intracellular ATP levels, we investigated the effects of the cellular energy status on the observed changes in macromolecular mobility. To quantify the reduction of ATP upon glucose starvation, cells were washed into SC media and either diluted back into media containing 2% Dextrose or maintained in SC. Aliquots of each culture were taken at 0, 10, 30, and 60 minutes and ATP concentrations were measured using a luciferase-based ATP assay (Ashe et al., 2000). Values were corrected for the optical density of the culture, and compared relative to pre-wash ATP concentrations and to defined standard curves. Upon glucose starvation ATP levels rapidly decreased by ~75% from ~6 mM in pre-starved cells to ~1.5 mM. Remarkably, after this initial drop ATP levels were relatively stable at ~1.5 mM for the remainder of the experiment (**Fig 4.5A**). Of note, the maintenance of this reduced ATP level required oxidative phosphorylation as the cellular ATP concentration quickly dropped to undetectable levels in mutant cells deficient in mitochondrial function (*cbp2*Δ; **Fig 4.6**) (Shaw and Lewin, 1997). Similar to acute starvation, a reduction of intracellular ATP levels to ~1.5 mM was observed in quiescent cells (**Fig 4.5B**; data not shown). In contrast, when cells were back diluted into media containing glucose, ATP levels recovered to ~6 mM (100% of initial value) within 30 minutes. Thus, glucose starvation induces a rapid, ~ 75% reduction of intracellular ATP levels to a concentration of ~1.5 mM, in agreement with previously published results (Özalp et al., 2010).

To determine whether a ~75% reduction in intracellular ATP levels is sufficient to confine cytoskeleton-independent macromolecular mobility as well as mobility influenced by the cytoskeleton, we searched for conditions that would recapitulate such an ATP decrease in the presence of glucose. When cells were first washed with SC media and back diluted into 2% Dextrose media containing 0.02% sodium azide (NaN_3), an inhibitor of oxidative phosphorylation, cellular ATP dropped by 75% to ~1.5mM accurately mimicking the ATP concentration of glucose starved cells (**Fig 4.5A**). Notably, however, this treatment failed to recapitulate the starvation-induced confinement of both chromatin and mRNPs, as their mobility was greater than that of glucose-starved cells (**Fig 4.5B &C**). We therefore conclude that a 75% reduction

Figure 4.5

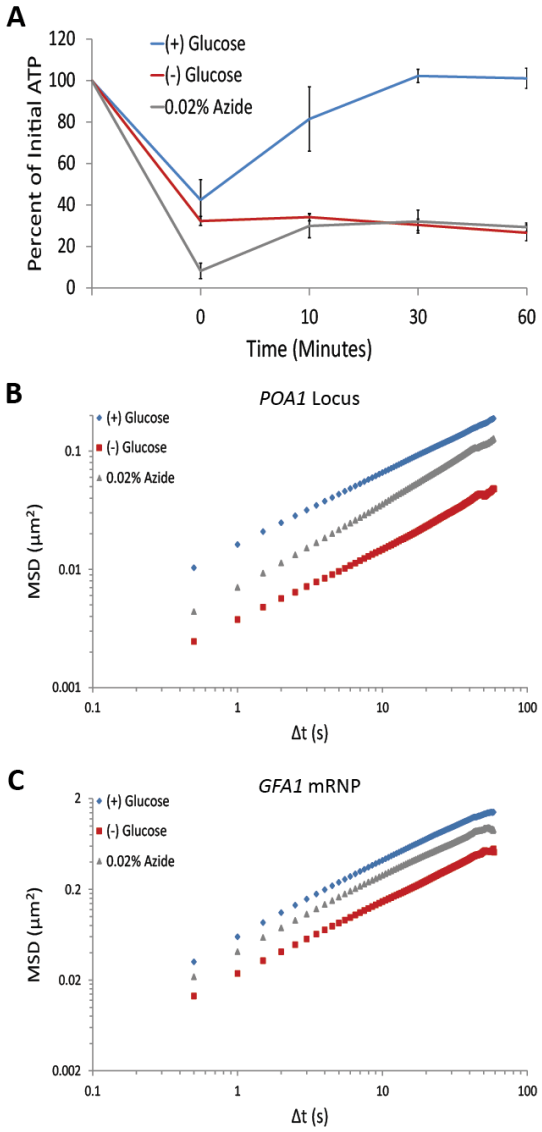

Figure 4.5: A ~75% reduction of intracellular ATP is insufficient to replicate the macromolecular confinement of glucose starvation.
A. Intracellular ATP concentrations. Log-growing cells were acutely starved of glucose and back diluted into media containing 2% Dextrose, 2% Dextrose + 0.02% Azide, or maintained in (-) glucose media. Intracellular ATP concentrations were determined using a luciferase-based ATP assay (Ashe et al., 2000) and normalized to pre-treatment levels (Initial ATP). The 0 minute time point was taken immediately after back dilution into the described media. Error bars represent SD.
B. Quantification of *POA1* mobility. Cells were treated as described in (**A**) and imaged after thirty minutes. The azide treatment fails to replicate the confinement in (-) glucose.
C. Quantification of *GFA1* mRNP mobility. Cells were treated as described in (**A**) and imaged after thirty minutes. The azide treatment fails to replicate the confinement in (-) glucose.

Figure 4.6

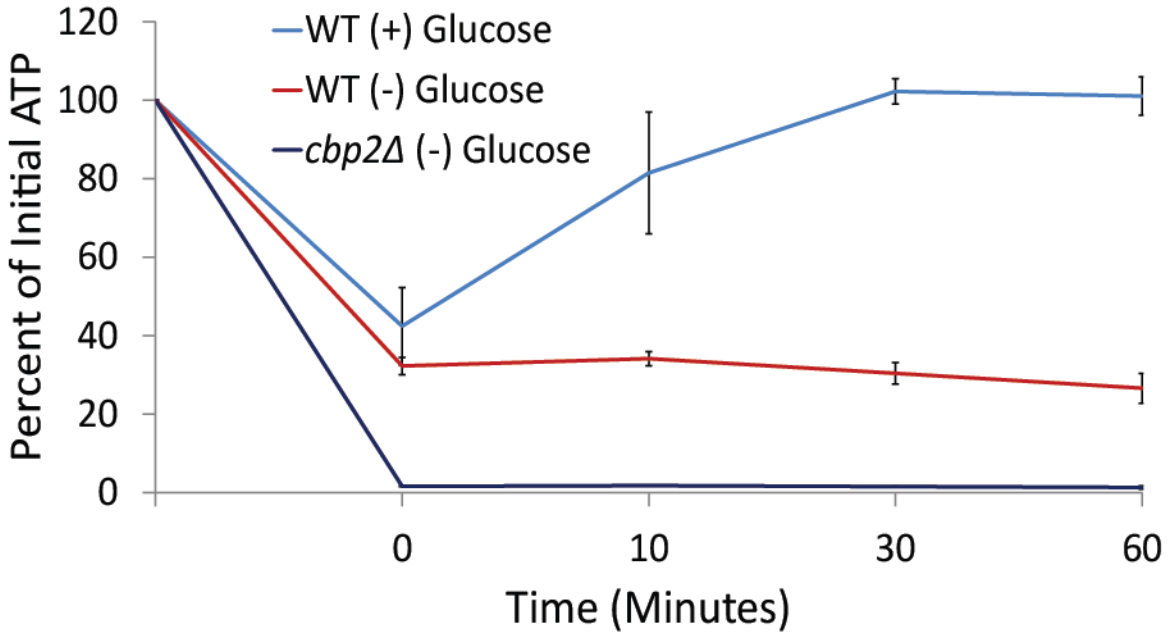

Figure 4.6: Respiration maintains intracellular ATP concentrations after acute glucose starvation. Log-growing WT and *cbp2*Δ cells were acutely starved for glucose and back diluted into media containing 2% Dextrose or maintained in (-) glucose media. Intracellular ATP concentrations were determined using a luciferase-based ATP assay and normalized to pre-treatment levels (Initial ATP). The 0 minute time point was taken immediately after back dilution into the described media. Error bars represent SD.

of intracellular ATP, as observed in glucose-depleted cells, is insufficient to explain the drastic confinement of macromolecular mobility during glucose starvation.

Reduction of intracellular pH titrates macromolecular mobility but cannot explain starvation-induced macromolecular confinement

If a singular, starvation-induced mechanism restricts the mobility of chromatin and mRNPs, such a pathway should induce a rapid and global change in the fundamental properties of the cell. Intriguingly, upon starvation, the intracellular pH (pH_i) of budding yeast was reported to decrease from pH ~7.3 to pH ~6.4 in a time frame consistent with our observed confinement of mobility (Orij et al., 2009; Young et al., 2010). We therefore tested whether a change in pH_i might be involved in the observed macromolecular confinement. Using the pH-sensitive GFP analog, pHlourin, as a pH_i biosensor (Miesenböck et al., 1998), we confirmed that glucose starvation indeed causes a reduction in pH_i from ~7.2 to ~6.4 in our experimental conditions (**Fig 4.7A**). We then manipulated intracellular proton concentrations by the addition of the weak acid potassium sorbate (K^+Sorbate). When protonated, K^+Sorbate traverses the plasma membrane, releases a proton, and reduces pH_i in a concentration-dependent manner (Bracey et al., 1998; Piper et al., 2001). Varying the extracellular concentration of K^+Sorbate from 0 mM to 8 mM enabled us to titrate pH_i from pH 7.2 to pH 5.9 thus covering more than the pH_i range observed in cells grown either in (+)glucose or (-)glucose conditions (**Fig 4.7A**). Remarkably, exposing cells to increasing concentrations of K^+Sorbate induced macromolecular confinement, and both chromatin and mRNP mobility could be titrated with decreasing pH_i (**Fig 4.7B & C**; **Fig 4.8 B-D**). In addition, the actin cytoskeleton was also strongly affected by a decrease in pH_i (**Fig 4.7D**).

Importantly, however, treatment with the highest concentration of K^+Sorbate (8mM) was necessary to fully recapitulate the various starvation-induced phenotypes, including the starvation-induced confinement of both chromatin and mRNPs (**Fig 4.7B & C**). Under these conditions, pH_i dropped to 5.9, which is significantly below the physiologically observed pH_i of 6.4 in glucose-starved cells. Conversely, when pH_i was lowered to 6.4 (by the addition of 2 mM K^+Sorbate) the movement of both chromatin and mRNPs was only moderately reduced and actin filaments were still detectable in many cells (**Fig 4.7D**). Thus, the starvation-induced reduction of pH_i alone cannot mimic the confinement of macromolecular mobility. However, because pH_i 5.9 perfectly recapitulated many starvation-induced phenotypes, it remained possible that a pH_i reduction to 5.9 triggered a similar cellular response as starvation which is sufficient to confine macromolecular mobility.

Starvation induces a constriction in cell size confining macromolecular mobility

In the course of our experiments, we discovered a decrease in the nuclear volume upon glucose withdrawal (**Fig 4.9A**). Since nuclear volume and cellular volume are generally tightly linked (Neumann and Nurse, 2007; Jorgenesen et al., 2002) we utilized a Coulter Counter to examine whether cell size changes upon glucose starvation. Indeed, histograms of 50,000 cells revealed a distinct starvation-induced

Figure 4.7

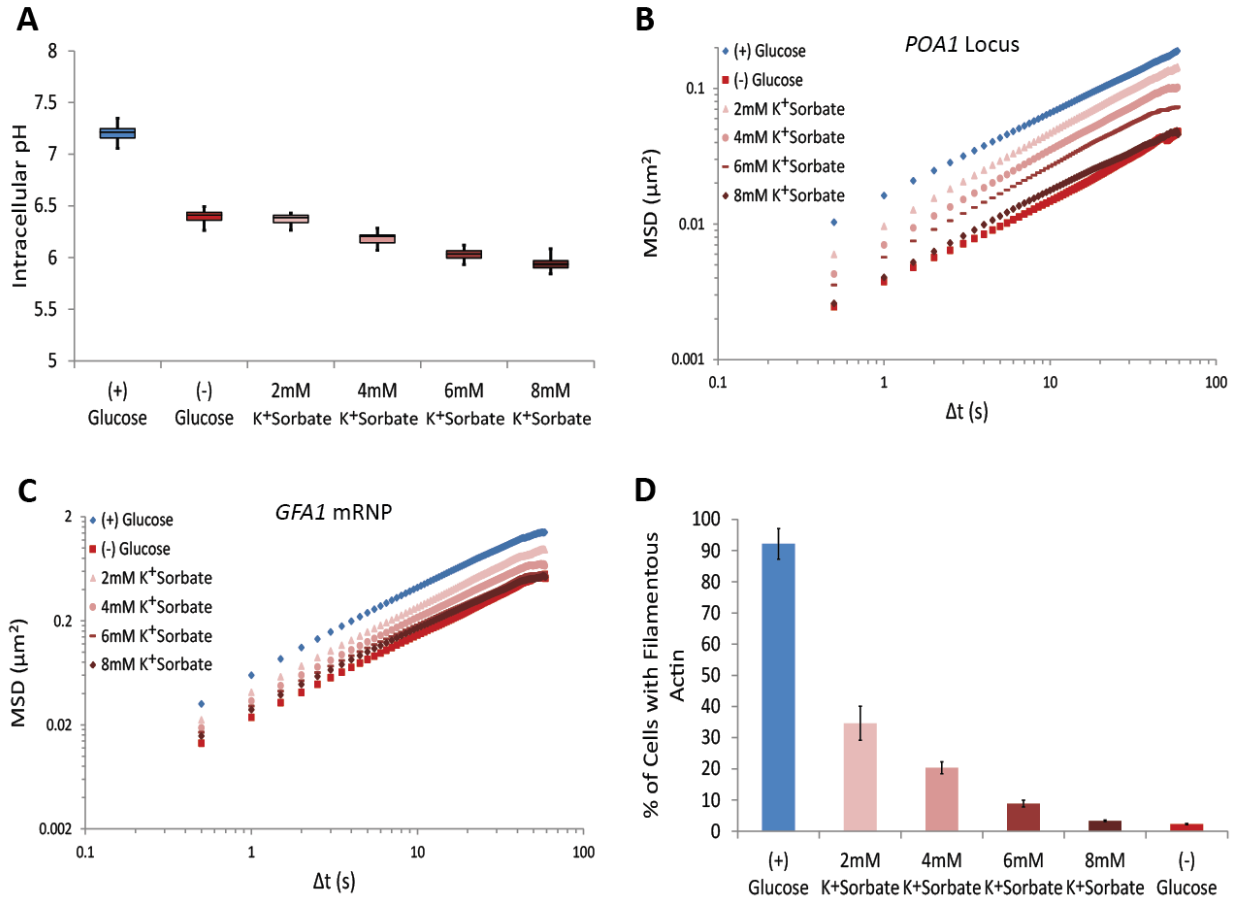

Figure 4.7: A drop in intracellular pH (pH_i) is sufficient to confine macromolecular mobility but cannot explain the confinement observed in glucose-starved cells.
A. pH_i of cells acutely starved for glucose or treated with varying concentrations of potassium sorbate (K^+Sorbate). Log-growing cells expressing pHlourin (Miesenböck et al., 1998) were acutely starved of glucose or treated with K^+Sorbate for thirty minutes prior to ratiometric imaging. Intracellular pH was then estimated from a calibration curve (see **Materials and Methods**; **Fig 4.8A**). Values from biological replicates were pooled and compiled into boxplots. Note that treatment with 2mM K^+Sorbate is sufficient to replicate the pH_i of glucose-starved cells at pH ~6.4.
B. Mobility of the *POA1* locus. Cells were treated as described in (**A**) and imaged after thirty minutes. Decreasing pH_i titrates chromatin mobility but an intracellular pH of ~5.9 (8mM K^+Sorbate) is necessary to replicate the confinement of glucose-starved cells.
C. Mobility of the *GFA1* mRNP. Cells were treated as described in (**A**) and imaged after thirty minutes. Decreasing pH_i titrates mRNP mobility but an intracellular pH of ~5.9 (8mM K^+Sorbate) is necessary to replicate the confinement in glucose-starvation.
D. Quantification of filamentous actin upon treatment with K^+Sorbate. Cells were treated as in (**A**) and stained with phalloidin. Filamentous actin was quantified as described in (**Fig 4.3A**). Error bars are SEM for 3 biological replicates (n = 350-800 cells). Note that 8mM K^+Sorbate treatment approximately replicates glucose starvation.

Figure 4.8

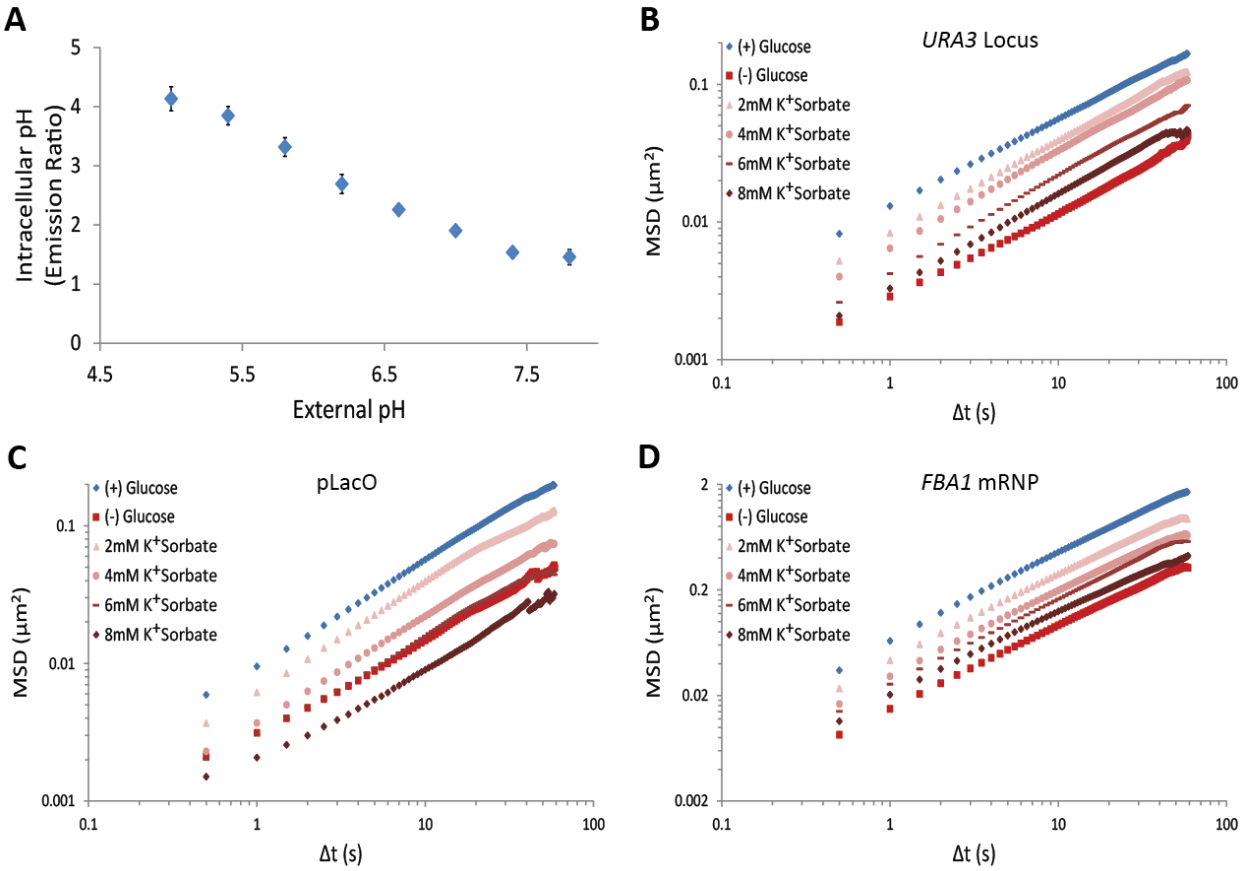

Figure 4.8: A drop in intracellular pH (pH_i) titrates macromolecular mobility.
A. Intracellular pH calibration curve (Orij et al., 2009) (see **Materials and Methods**).
B. Quantification of the mobility of the *URA3* locus. Cells were treated as described in (**Fig 4.7A**) and imaged after thirty minutes.
C. Quantification of the mobility of pLacO. Cells were treated as described in (**Fig 4.7A**) and imaged after thirty minutes.
D. Mobility of the *FBA1* mRNP. Cells were treated as described in (**Fig 4.7A**) and imaged after thirty minutes.

volume reduction, as the median cell volume condensed from 88fL (σ = 47) in glucose to 75fL (σ = 38) in starved cells, corresponding to a volume reduction of ~15% (**Fig 4.9B**). We subsequently hypothesized that such a large volume reduction may be sufficient to induce the observed macromolecular confinement, e.g. by an increase in crowding or changes in cellular viscosity (Luby-Phelps, 2000).

Because high concentrations of potassium sorbate replicate the confinement of both chromatin and mRNPs during starvation, if the hypothesis was correct that a loss of cell volume was the singular response that confines macromolecular mobility, two predictions could be made: (1) lowering of pH_i by the addition of K^+Sorbate might induce a loss of cellular volume explaining the effects that we had seen upon addition of high concentrations of K^+Sorbate, and (2) manipulation of cellular volumes, for example, by changes in osmolarity should recapitulate the effects of glucose starvation on cytoskeleton-independent mobility (mRNPs), on mobility influenced by the cytoskeleton (chromatin), and on the actin cytoskeleton itself.

To test our first prediction, we explored the effect of pH_i changes on cell volume. Remarkably, lowering pH_i by the addition of K^+Sorbate also induced an increasing reduction in cell volume (**Fig 4.9B**; **Fig 4.10**), and addition of 8mM K^+Sorbate (corresponding to pH_i 5.9) condensed the median cell volume by ~14% (median = 76; σ = 41), a level virtually identical to that of glucose-starved cells (**Fig 4.9B**). This data suggested a strong relationship between cell size and macromolecular mobility, given the increasing confinement of mobility with decreasing cell volume. Indeed, we note a remarkable linear correlation between cell volume and the mean radius of gyration (a metric quantifying the space explored by a particle) of the *FBA1* mRNP in our distinct conditions (R^2=0.97) (**Fig 4.9C**; **Fig 4.10**) (Latulippe and Zydney, 2010). Thus, there is a strong overall correlation between the reduction of cellular volume and the effects on macromolecular mobility, as two independent treatments (glucose starvation and lowering of pH_i) had identical effects on cell volume (**Fig 4.9B**), the cytoskeleton (**Fig 4.7D**), chromatin dynamics (**Fig 4.7B**) and mRNP mobility (**Fig 4.7C**).

To test prediction (2) and further validate our model, we treated cells with increasing concentrations of NaCl and monitored the effects on chromatin, mRNPs and the cytoskeleton. Notably, addition of NaCl had no effects on pH_i, allowing us to completely uncouple the effects of cell volume from intracellular pH (**Fig 4.9D**). As expected, both chromatin and mRNP mobility were progressively confined by increasing the magnitude of osmotic shock (**Fig 4.9E & F**) (Babazadeh et al., 2013; Miermont et al., 2013). Osmotic shock was also sufficient to prevent the formation of actin cables and filaments (**Fig 4.11C**), consistent with prior observations (Chowdhury et al., 1992). Therefore, a reduction of cell volume is sufficient to fully phenocopy the starvation-induced effect on macromolecular mobility. This strongly suggests that cellular volume loss is the underlying mechanism for the confinement of macromolecular mobility upon glucose starvation.

Starvation-induced crowding impedes the diffusion of macromolecules

We next wanted to explore how the loss in cell volume impedes the movement of macromolecules. In principle, the volume loss triggered by glucose-starvation could lead to an increase in intracellular viscosity, which in turn would slow down macromolecular

Figure 4.9

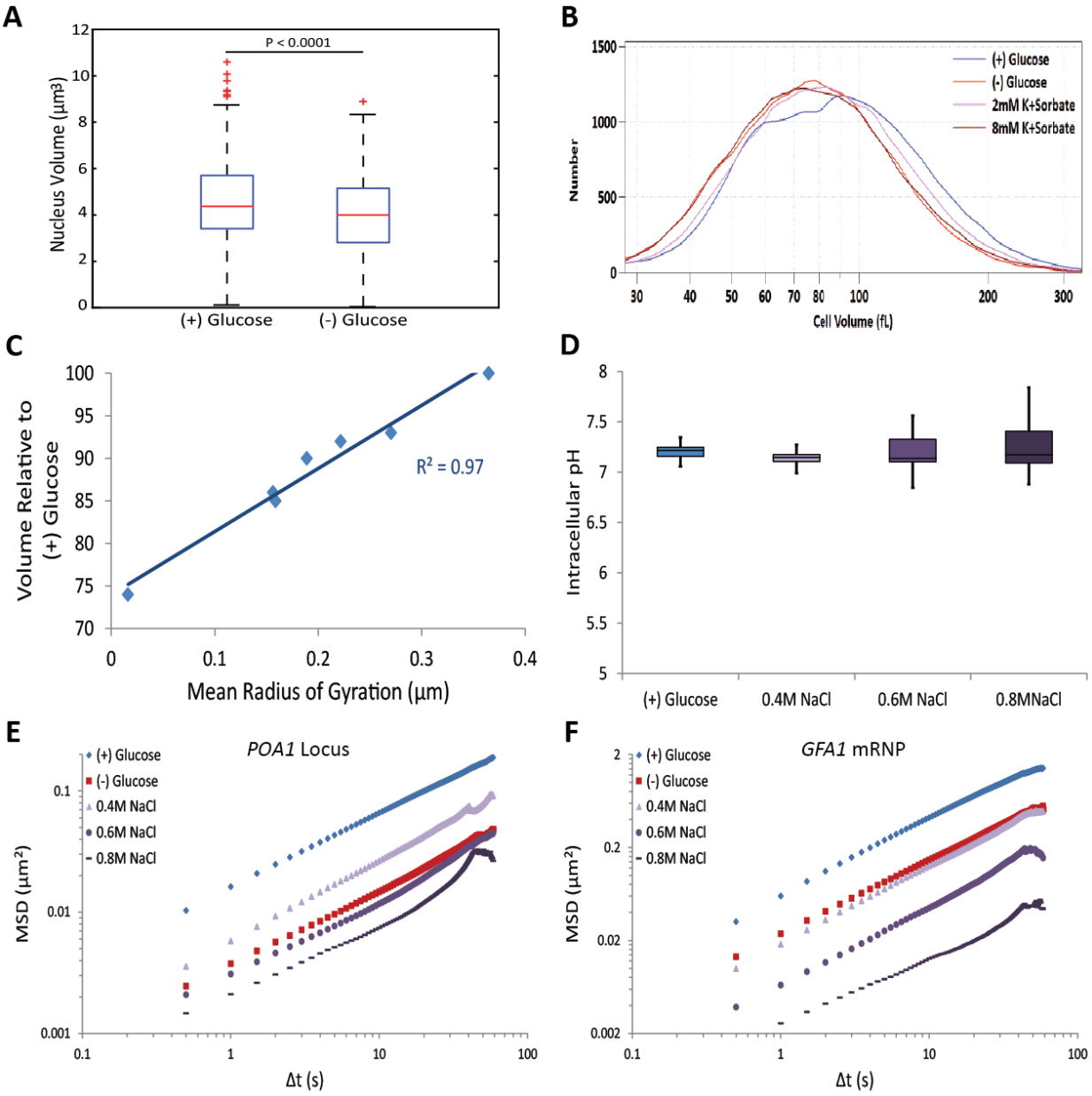

Figure 4.9: Starvation induces a constriction in cell size which confines macromolecular mobility.

A. Nuclear volume after acute glucose starvation. Nuclear volume was measured by reconstruction from three-dimensional stacks using Imaris. Results are plotted as boxplots. Outliers (red crosses) as defined as points further from the quartile-box than 1.5 times the length of the quartile box. *P*-values shown are for a two-tailed t-test for unpaired values assuming equal variance.

B. Cell volume after acute glucose starvation or treatment with K^+Sorbate. Cells were treated as described in (**Fig 4.7A**) and the volume of approximately 50,000 cells was measured in each condition using a Beckman Coulter Multisizer 3 (see **Materials and**

Methods). Smoothing was set to 5. Note the overlap in the distributions of cells acutely starved for glucose and those treated with 8mM K^+Sorbate.
C. Correlation between median cell volume (**Fig 4.10**) and the mean radius of gyration of the *FBA1* mRNP in each condition.
D. pH_i of cells after osmotic shock. Log-growing cells expressing pHlourin were treated with varying concentrations of NaCl for 10 minutes prior to ratiometric imaging. Values from biological replicates were pooled and compiled into boxplots.
E. Quantification of the mobility of the *POA1* locus. Cells were treated as described in (**D**) and imaged after 10 minutes. Increasing the magnitude of the osmotic shock increases the confinement of the *POA1* locus.
F. Quantification of the mobility of the *GFA1* mRNP. Cells were treated as described in (**D**) and imaged after 10 minutes. Increasing the magnitude of the osmotic shock increases the confinement of the *GFA1* mRNP.

Figure 4.10

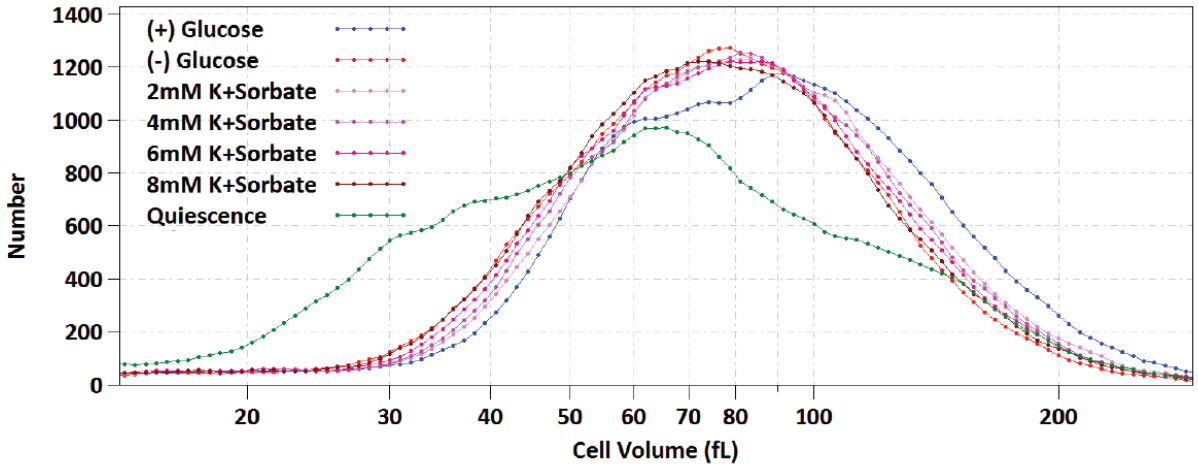

Figure 4.10: Volume distributions of cells in various conditions. Cells were treated as described and cell volume measured using a Beckman Coulter Multisizer 3 (see **Materials and Methods**). The volume of approximately 50,000 cells was measured in each condition and smoothing set to 5. Note the decrease in cell volume with increasing concentrations of K^+Sorbate.

Figure 4.11

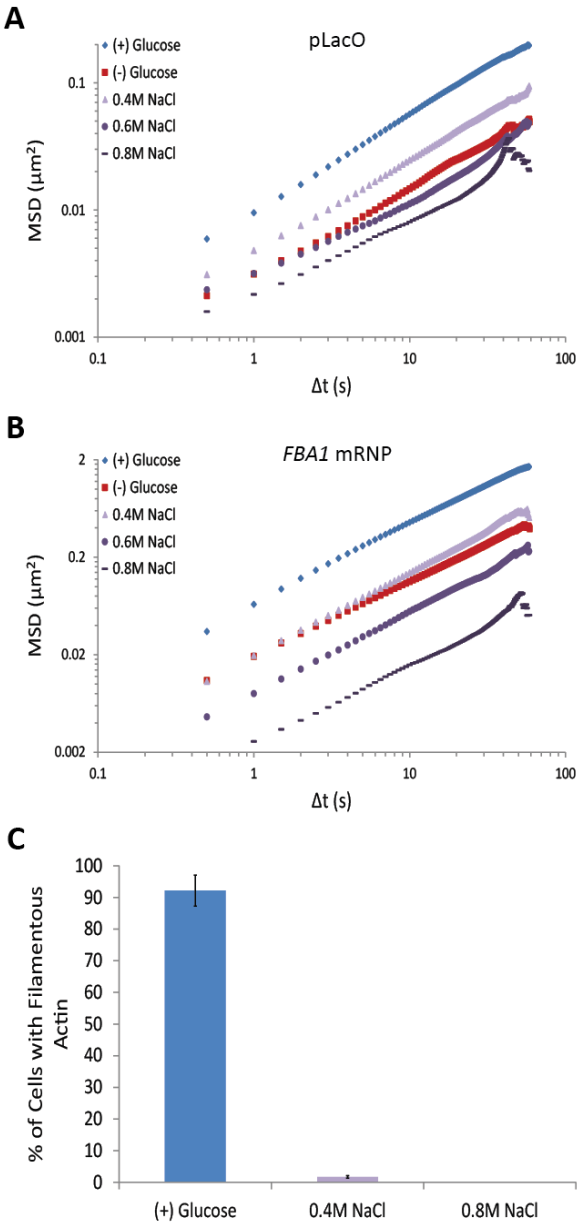

Figure 4.11: Osmotic shock increasingly confines macromolecular mobility.
A. Mobility of pLacO. Cells were treated as described in (**Fig 4.9D**) and imaged after 10 minutes. Increasing the magnitude of the osmotic shock increases the confinement of pLacO.
B. Mobility of the *FBA1* mRNP. Cells were treated as described in (**Fig 4.9D**) and imaged after 10 minutes. Increasing the magnitude of the osmotic shock increases the confinement of the *FBA1* mRNP.
C. Quantification of filamentous actin after osmotic shock. Cells were treated as in (**Fig 4.9D**) and stained with phalloidin. Filamentous actin was quantified as described in (**Fig 4.3A**). Error bars are SEM for 3 biological replicates (n = ~125-275 cells per replicate).

diffusion (Luby-Phelps, 2000). Alternatively, crowding could induce complex phase transitions in the very densely packed environment of the cell (Doliwa and Heurer, 1998; Weeks et al., 2000). Whereas changes in cellular viscosity should affect the diffusion of molecules independent of size, liquid-to-solid-like transitions due to crowding and caging might preferentially affect large macromolecular complexes (Doliwa and Heurer, 1998; Weeks et al., 2000). To differentiate between these two possibilities, we employed Fluorescence Correlation Spectroscopy (FCS) and monitored the effects of glucose-starvation on the cellular diffusion of free GFP and a larger variant, TetR-GFP (**Fig 4.12A**). Under starvation conditions, we were unable to detect any statistically significant difference in the diffusive behavior of GFP compared to log growing cells. In contrast, however, we observed a substantial increase in the diffusion time of TetR-GFP (**Fig 4.12A**). Together, this argued against a global change in cellular viscosity as the diffusion rates of the two distinct molecules were not similarly affected by starvation. Instead, this supports a hypothesis that the starvation-induced reduction in intracellular diffusion exhibits size-dependent heterogeneity that preferentially affects larger macromolecules. Our observations are therefore consistent with constriction-induced crowding which confines macromolecular mobility while simultaneously permitting the unperturbed diffusion of smaller particles (**Fig 4.12A**) (Luby-Phelps, 2000).

Cellular volume reduction is a conserved starvation response

Interestingly, it was recently reported that the bacterial cytoplasm has glass-like properties and can undergo liquid-like to solid-like transitions upon starvation or treatment with 2,4-Dinitrophenol (DNP), an uncoupler of oxidative phosphorylation (Parry et al., 2014). This results in confinement of macromolecules disproportionally affecting large particles above ~30 nm (Parry et al., 2014). The underlying mechanism for this cytoplasmic transition into a solid-like state in bacteria remained unexplored, but Parry et al. (2014) suggested that metabolic activity is needed to keep the bacterial cytoplasm fluid. Whereas the cytoplasmic organization of prokaryotic and eukaryotic cells have dramatic differences, the startling similarity between these observations in bacteria and our findings in yeast prompted us to test whether there is a common underlying mechanism and whether bacteria also use a reduction in cell volume to increase crowding and confine macromolecular mobility. To directly compare our results with those of Parry et al. (2014) we repeated their protocol and treated *E. coli* with 2mM DNP. Strikingly, a 30 minute treatment with DNP caused a significant reduction in the volume of *E.coli*, inducing a ~10% volume contraction by median (**Fig 4.12B**). This suggests that the reported liquid- to solid-like phase transition of the bacterial cytoplasm is also triggered by cellular volume loss and demonstrates that the starvation-induced reduction of cell size is an evolutionarily ancient and highly conserved starvation response (Parry et al., 2014).

Discussion and Future Directions

Our results identify a novel, conserved cellular pathway that restricts intracellular diffusion in response to glucose starvation. The dramatic macromolecular confinement that we observed upon starvation cannot be explained by a reduction of intracellular

Figure 4.12

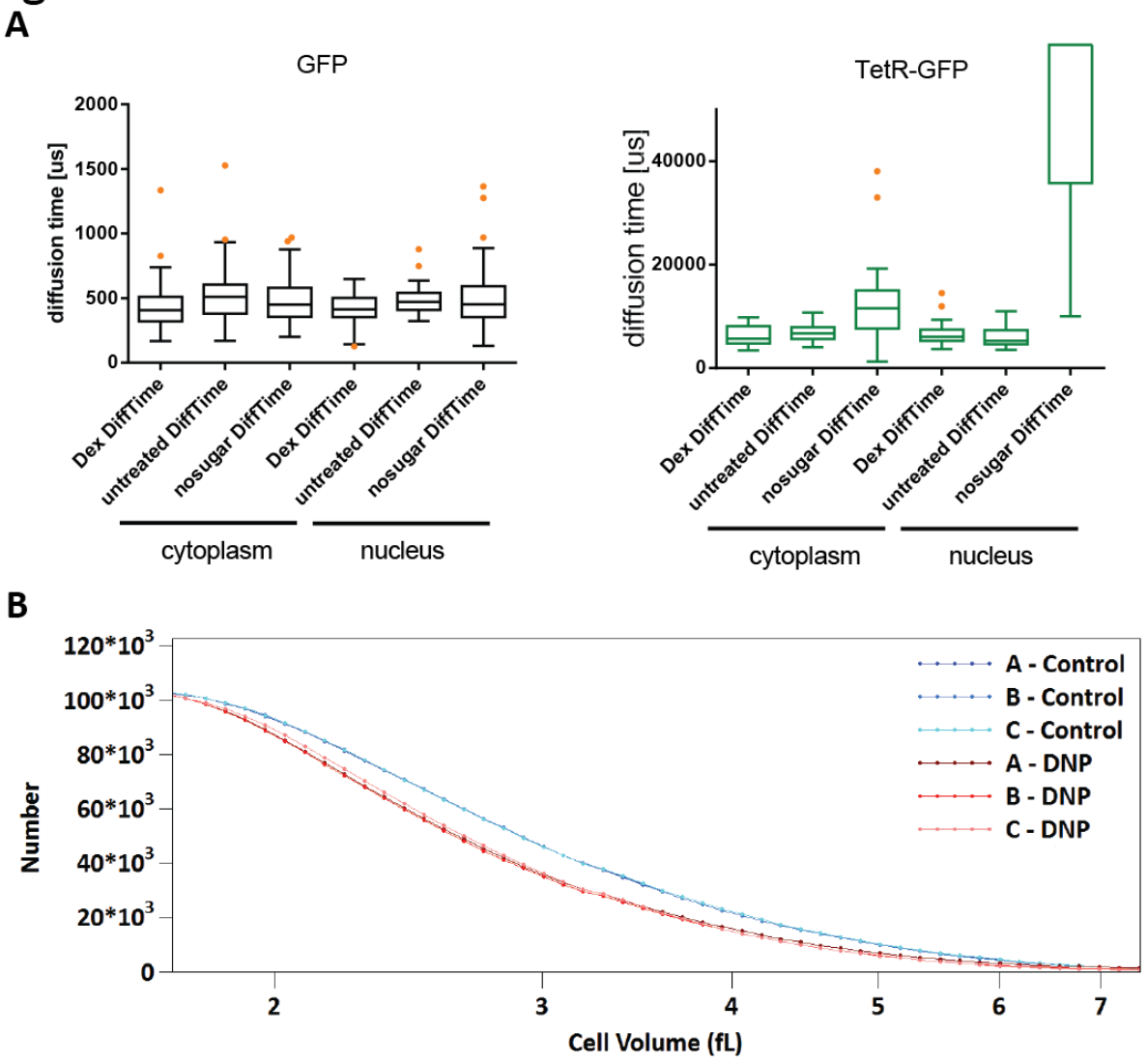

Figure 4.12: A conserved starvation response of cell constriction impedes the diffusion of macromolecules.
A. Diffusion rates of GFP (left) and TetR-GFP (right) in the nucleus and cytoplasm as determined by fluorescence correlation spectroscopy (FCS) (see **Materials and Methods**). Acute starvation slows the diffusion of TetR-GFP but has no statistically significant effect on the rate of diffusion of GFP.
B. Inverse cumulative histograms of wild type *E.coli* treated with 2mM DNP. Log-growing cells were treated with 2mM DNP or the vehicle control (EtOH, 1% final conc.) for 30 minutes before cell volume was measured using a Beckman Coulter Multisizer 3 (see **Materials and Methods**). The volume of approximately 100,000 cells was measured in each condition. DNP induces a volume reduction of ~10% by median compared to the control. Three biological replicates are shown.

ATP (**Fig 4.5**) or inhibition of global metabolism, as respiration persists upon glucose depletion (**Fig 4.6**). Instead, we propose that that macromolecular crowding induced by an acute volume loss is the cause of the macromolecular confinement. Whereas the cytosolic acidification that occurs in yeast cells might contribute to macromolecular confinement during starvation, possibly by changing the protein charge density and repulsive electrostatic forces within the cell (Fels et al., 2009), this pH drop alone is not sufficient to recapitulate the macromolecular confinement or the corresponding volume loss of starved cells (**Fig 4.7 & 4.9**). Therefore, more work is needed to elucidate the signaling pathways and mechanisms of how glucose starvation causes cell size contraction.

Our data also identify a novel mechanism of chromatin mobility in which the movement of yeast chromatin is strongly influenced by the joint dynamics of both actin and microtubules. Precedence for such a mechanism is evidenced by previous work describing similar microtubule-dependent motion and the known functional interactions between microtubules, spindle pole bodies, and centromeres throughout the cell cycle (Heun et al., 2001; Tanaka and Tanaka, 2009). Moreover, the actin cytoskeleton is known to propel the movement of meiotic chromosomes, suggesting a central function throughout the life cycle of yeast, and influence the diffusion of large macromolecules (Koszul et al., 2008; Zhou et al., 2011; Brangwynne et al., 2009). The long-range directional movement of chromosomal loci is also reported to be dependent on the actin cytoskeleton (Chuang et al., 2006). This is consistent with our data, as the cytoskeletal inhibitors latrunculin-A and nocodozale appeared to more strongly affect the mobility of chromatin at longer timescales versus the fast movements at shorter ones (**Fig 4.3; Fig 4.4**). Finally, recent work detailing the existence of actin filaments in the nucleus substantiates the possibility of a robust network of nuclear actin (Baarlink et al., 2013). However, our work cannot currently differentiate between cytoplasmic and nuclear actin in modulating chromatin mobility.

Paradoxically, previous experiments exploring the ATP-dependence of chromatin mobility reached opposing conclusions in that treatment with sodium azide had only minor effects on the mobility of chromosomes in one study (Marshall et al., 1997) but drastically reduced their mobility in another (Heun et al., 2001). To explore this discrepancy we tracked both chromatin and mRNPs in conditions that replicated the perceived differences in the two published protocols (Marshall et al., 1997; Heun et al., 2001). By varying the treatments, we were indeed able to duplicate the distinct results such that one azide protocol had only moderate effects on macromolecular mobility whereas the other led to a substantial confinement of both macromolecules (**Fig 4.13**). Importantly, however, we also observed that azide treatment lowered pH_i and that the distinct treatments reduced intracellular pH to dramatically different extents (**Fig 4.13**), consistent with the reduction of pH_i reported with treatment of CCCP (Peters et al., 2013). In fact, both the intracellular pH and levels of macromolecular confinement of the different azide protocols closely matched that of the lowest and highest levels of potassium sorbate, respectively (2mM and 8mM; **Fig 4.13**). Thus, a pleiotropic effect of azide treatment on pH_i might be sufficient to reconcile the observed differences in the confinement of macromolecules. These results also show that the azide treatment used here (**Fig 4.5**; Wash; **Fig 4.13**) replicates both the decrease in intracellular ATP concentrations and the drop in pH_i in glucose-starved cells. This indicates that changes

Figure 4.13

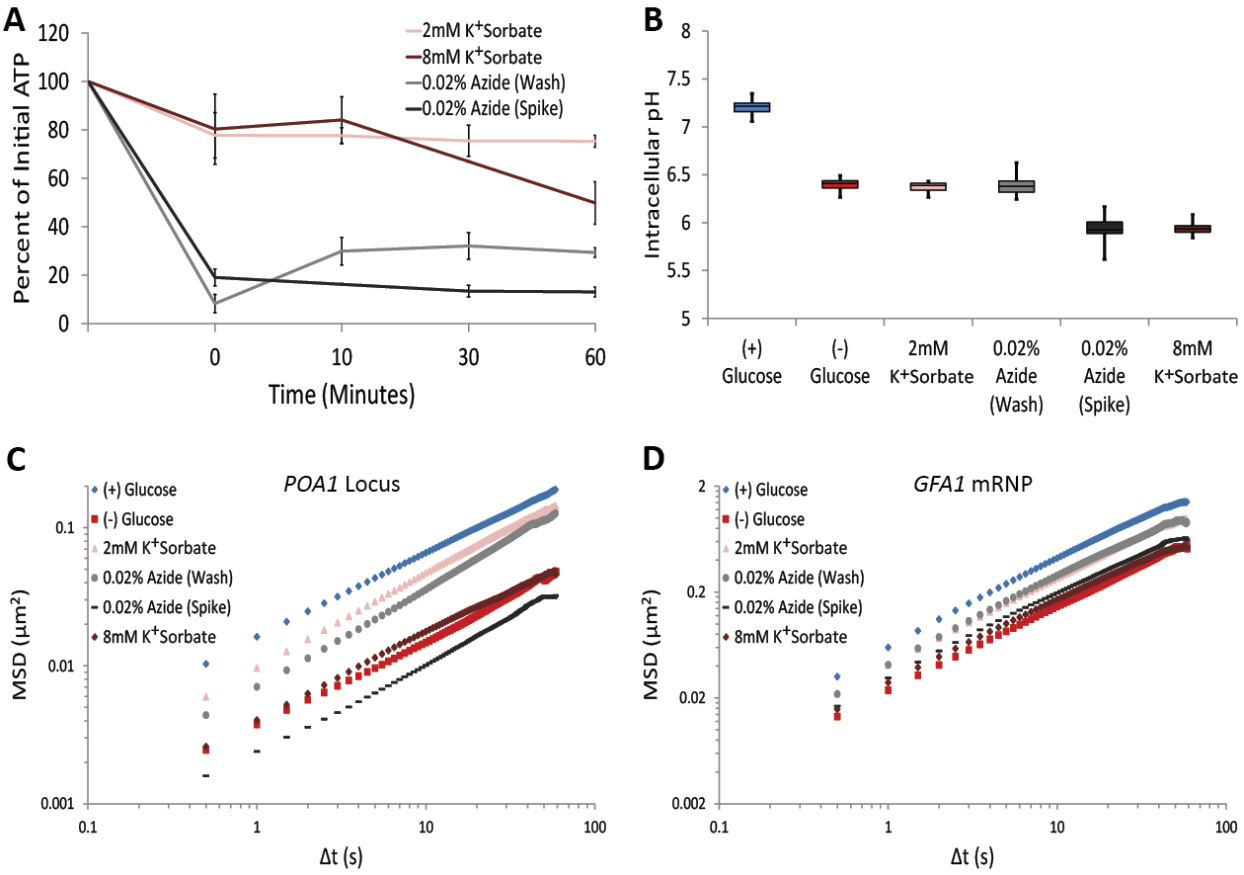

Figure 4.13: Sodium azide induces a pleiotropic reduction in pH_i which may explain the subsequent confinement of macromolecular mobility.
A. Intracellular ATP concentrations after treatment with K^+Sorbate or distinct treatments with 0.02% sodium azide (Wash and Spike) (see **Materials and Methods**). Intracellular ATP concentrations were determined using a luciferase-based ATP assay and normalized to pre-treatment levels (Initial ATP). The 0 minute time point was taken immediately after each treatment. Error bars represent SD.
B. Intracellular pH (pH_i) of cells treated as in (**A**). Log-growing cells expressing pHlourin were treated as described for 30 minutes prior to ratiometric imaging. Values from biological replicates were pooled and compiled into boxplots.
C. Mobility of the *POA1* locus after 30 minutes of each treatment described in (**A**). Note the close overlap between (-) glucose, 0.02% Azide (Spike), and 8mM K^+Sorbate and, separately, between 0.02% Azide (Wash) and 2mM K^+Sorbate.
D. Mobility of the *GFA1* mRNP after 30 minutes of each treatment described in (**A**). Note the close overlap between (-) glucose, 0.02% Azide (Spike), and 8mM K^+Sorbate and, separately, between 0.02% Azide (Wash) and 2mM K^+Sorbate.

in ATP and pH_i do not have additive effects and are neither alone nor in combination sufficient to explain the effects on macromolecular mobility.

Upon starvation, the cytoplasm of yeast undertakes an astonishing transition to inhibit the movement of large molecules with little or no effects on small proteins (**Fig 4.12**). This is remarkably similar to a recently published observation in bacteria describing a glassy liquid-to-solid transition upon glucose starvation (Parry et al., 2014). In agreement, we demonstrate that bacteria undergo a volume loss similar to starved-yeast (**Fig 4.12**) which suggests that molecular crowding might trigger the reported phase transition in bacteria in addition to our observations. Notably, this modulation of intracellular diffusion represents a profound mechanism to globally and pervasively regulate intracellular biochemistry. As described for bacteria (Parry et al., 2014), we envision glucose starvation as a "frozen"-state in which cells essentially hibernate until provisions in the environment improve. Consequently, we propose that cells functionally regulate intracellular diffusion in order to establish a cellular organization which is restrictive to unwarranted molecular interactions while simultaneously permissive to essential biochemistry (Parry et al., 2014).

The evolutionary conservation of cell contraction strongly suggests a vital function during starvation. On the one hand, the reduction in macromolecular mobility may allow for the rapid inhibition of excessive energy expenditure by diminishing unnecessary molecular interactions. This is consistent with previous observations describing the rapid inhibition of principal ATP consumers upon starvation. For example Pma1p, required for regulation of intracellular pH and thought to use upwards of 60% of cellular ATP, is immediately inhibited upon glucose starvation (Bracey et al., 1998). Ribosomes also disengage from mRNA, resulting in a global collapse of polysome profiles (Ashe et al., 2000). Additionally, we found that depolymerization of the actin cytoskeleton may function, in part, to conserve ATP, as treatment with Latrunculin-A rapidly increases intracellular ATP concentrations (**Fig 4.14**). Because osmotic shock promptly inhibits translation initiation and depolymerizes the actin cytoskeleton, it is conceivable that the starvation-induced cytoskeletal breakdown and collapse of polysome profiles, as well as other starvation-associated phenotypes, could be partly driven by molecular crowding (Chowdhury et al., 1992; Ueseono et al., 2004; Ashe et al., 2000; Uesono and Toh-e, 2002). Therefore, the confinement of intracellular diffusion may prove vital for economical biochemistry and represent a very upstream event upon carbon starvation.

On the other hand, confined macromolecular mobility may also promote sustained functional interactions between key complexes during starvation. In agreement with this hypothesis, starvation is known to induce the formation of compartmentalized biochemistry and potential pockets of liquid-liquid unmixing (Narayanaswamy et al., 2009; Brangwynne et al., 2009). For example, P-bodies, macromolecular complexes composed of mRNPs and mRNA decay machinery, form in the absence of glucose and potentially aggregate through unstructured regions of the component proteins (Ramachandran et al., 2011). Moreover, stationary phase induces the formation of foci for a host of proteins, hypothesized to enhance interactions between members of the same pathway and initiate more efficient biochemistry (Narayanaswamy et al., 2009). As a consequence, prolonged starvation and confinement of macromolecular mobility may also pose unique challenges to cells, as

Figure 4.14

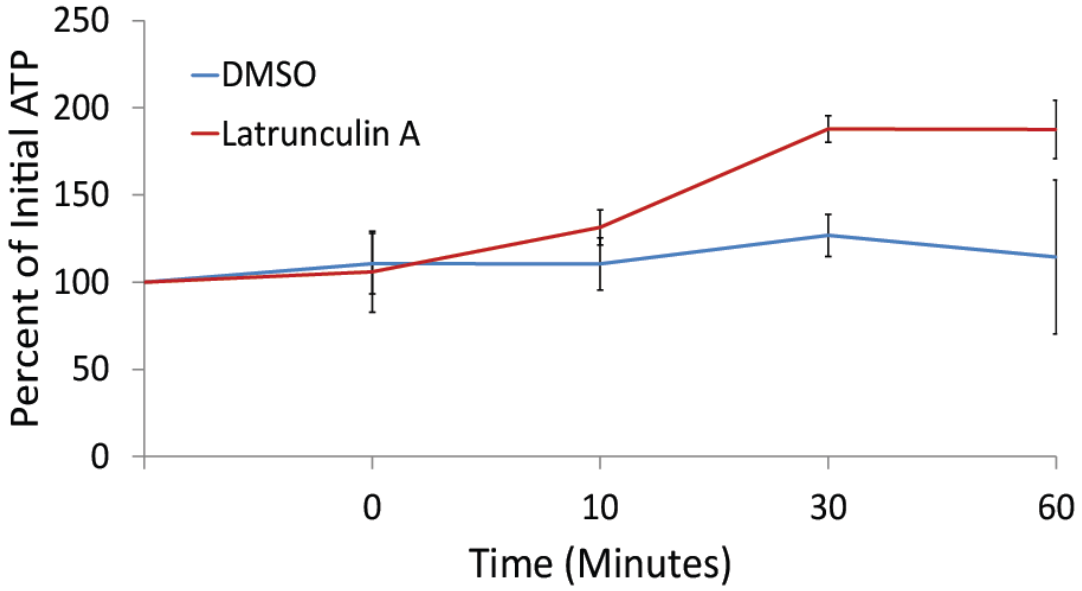

Figure 4.14: Treatment with Latrunculin A dramatically increases intracellular ATP concentrations. Log-growing cells were treated with Latrunculin A or the vehicle control (DMSO). Intracellular ATP concentrations were determined using a luciferase-based ATP assay and normalized to pre-treatment levels (Initial ATP). The 0 minute time point was taken immediately after each treatment. Error bars represent standard deviation from four biological replicates. *P*-values from a two-tailed t-test for unpaired values assuming equal variance are as follows: $p = 0.0003$ for the 30 minute time point and $p = 0.0363$ for the 60 minute time point.

complexes with elongated stretches of unstructured regions may prove more prone to extensive aggregation. It will now be interesting to explore whether other cell types, including metazoan cells, respond similarly to starvation or growth factor depletion and if limited diffusion indeed stimulates aberrant protein aggregation, a process which has been implicated in a wide variety of human diseases (Ross and Poirier, 2004).

Materials and Methods

Strains and Growth

Yeast strains used in this study are of the W303 strain-background, except for strains containing labelled mRNPs which are heterozygous diploids of W303 and S288c backgrounds. The *E. coli* strain utilized for volume measurements is wild type BW25113. Genotypes for every strain are listed in **Table 4A**; plasmids are described in **Table 4B**. Unless otherwise indicated, cells were grown at room temperature (22ºC) in synthetic complete (SC) media at pH 5.0 (titrated with 1M HCl) containing 2% Dextrose (SCD). Specific dropout media was used to maintain plasmids when necessary.

Imaging and Particle Tracking

Time-lapse fluorescence imaging was performed using an inverted Nikon TE2000 microscope equipped with an Andor CCD camera, a motorized stage (ASI), 60X/1.49NA APO TIRF oil immersion objective, and controlled with Metamorph® software. Cells were stabilized by coating the glass-bottom of MatTek dishes (MatTek Corporation, PG35G-1.5-14-C) with 0.2% Concanavalin A and aspirating the solution prior to adding 300µL of OD_{600} 0.2-0.3 cells. All imaging was performed at room temperature (22ºC). Images were analyzed and particles tracked using custom MatLab (The MathWorks, Inc.) scripts based on the 2D feature finding and particle tracking software made available by Maria Kinfoil (Pelletier et al., 2009; http://people.umass.edu/kilfoil/downloads.html).

Ensemble averaged MSDs were calculated for each condition using the equation:

$$MSD\tau = \langle \left(r_{(t+\tau)} - r_t\right)^2 \rangle$$

Diffusion coefficients were then computed by finding the slope of the best fit line between the third and eleventh time intervals of the MSD (1.5 - 5.5sec).

The Radius of Gyration (R_g) was calculated in one-dimension to the 80th observation using the equation:

$$R_g = \sqrt{\sum_{i=0}^{m} \frac{1}{m} (x(t_i) - x_0)^2}$$

Where x_0 is the average coordinate of the particle and $x(t_i)$ the coordinate at the i-th observation, with total number of observations m (Latulippe and Zydney, 2010).

Acute Starvation

Table 4A: Yeast strains used in this study.

Strain #	Genotype	Source
KWY 165	*W303 MATa* ura3-*1 leu2-3 his3-11,15 trp1-1 ade2-1*	This Study
KWY 1622	*W303 MATα ybr022w::256LacO::LEU2 his3::LacI-GFP::HIS3 trp1::dsRED-HDEL::TRP1*	Green et al., 2012
KWY 3541	*KWY 1622, cbp2Δ::KANMX*	This Study
KWY 3538	*W303 MATα his3::LacI-GFP::HIS3 trp1::dsRED-HDEL::TRP1 256LacO::URA3*	This Study
KWY 2344	*W303 MATα his3::LacI-GFP::HIS3 trp1::dsRED-HDEL::TRP1 yel021w::128LacO::URA3*	This Study
KWY 4586	*W303 MATa ybr022w::112TetO::URA3 yfr023w::256LacO::LEU2 his3::LacI-GFP_TetR-3XmCherry::HIS3*	This Study
KWY 3661	*W303 MATa pHlourin::URA3*	This Study
KWY 4796	*W303 MATα trp1::dsRED-HDEL::TRP1 leu2::TetR-GFP::LEU2*	This Study
KWY 4343	*W303 MATa ura3::GFP$_{ACT1\text{-}Intron}$::URA3 trp1::dsRED-HDEL::TRP1::URA3*	This Study
KWY 4736	*W303 MATa/S288c MATα NDC1/ndc1::NDC1-tdTomato::KANMX GFA1/gfa1::GFA1-24PP7 3xYFP-PP7-CFP::HIS3*	This Study
KWY 4737	*W303 MATa/S288c MATα NDC1/ndc1::NDC1-tdTomato::KANMX FBA1/fba1::FBA1-24PP7 3xYFP-PP7-CFP::HIS3*	This Study

W303 Background:
*MAT*a/*MAT*α *leu2-3,112 trp1-1 can1-100 ura3-1 ade2-1 his3-11, 15*

S288c (BY4743) Background:
*MAT*a/α *his3Δ1/his3Δ1 leu2Δ0/leu2Δ0 LYS2/lys2Δ0 met15Δ0/MET15 ura3Δ0/ura3Δ0*

Table 4B: Plasmids used in this study.

Plasmid	Description	Source
pKW 2734	pHMX-256LacO (CEN, URA3)	This Study
pKW 2957	pYES2-PACT1-pHluorin (CEN, URA3)	Orij et al., 2009
pKW 2544	$MET25_{pro}$-PP7-CP-3xYFP (CEN, HIS3)	This Study

5mL of cells grown in SCD media (OD_{600}=0.4-0.7) were collected by centrifugation (3000rpm) for 2min. The supernatant was then removed and cells resuspended in 1mL of SC media. Four additional wash steps followed, with two 2min spins (6000rpm) succeeded by two 1min spins. The OD_{600} of the final cell suspension was determined and cells diluted into fresh SC or SCD media for analysis.

Potassium Sorbate Treatments

Mid-log cells growing in SCD media (pH 5.0) were incubated for thirty minutes with an appropriate concentration of stock 20mM K^+Sorbate in SCD (pH 5.0) to give rise to the corresponding final concentration of K^+Sorbate.

Sodium Azide Treatments

All experiments involving sodium azide (NaN_3) took place in SC or SCD media at pH ~5.8. Cells were treated with a final concentration of 0.02% NaN_3 (in water) by two distinct protocols. In one treatment, sodium azide was directly added, or "spiked", into a logarithmic culture. In the other, cells were first washed (via the acute starvation method) in SC media before being resuspended into SCD media containing NaN_3. This treatment is referred to as "wash".

Cytoskeleton Perturbations

Cells were treated with either 15µg/mL nocodazole (from a 1.5mg/mL stock in DMSO; Sigma-Aldrich), and/or 200µM latrunculin-A (from a 10mM stock in DMSO; Sigma-Aldrich) for 20min before imaging. This results in 3% DMSO as the control for the concurrent nocodazole/latrunculin-A treatment.

Osmotic Shock

Cells grown in SCD media (OD_{600}=0.4-0.7) were collected by centrifugation (3000rpm) for 2min and resuspended in SCD media containing the appropriate concentration of NaCl (0.4, 0.6, or 0.8M). Cells were imaged after 10 minutes of incubation in the appropriate osmotic shock media.

ATP Measurements

The protocol employed was only marginally modified from Ashe et al. (2000). Briefly, 20µL of sample (KWY 1622 cells in culture) was added to 20µL of 10% TCA and immediately vortexed for 1min. 10µL of the 40µL solution was then added to 990µL of ATP reaction buffer (25 mM HEPES, 2 mM EDTA, pH 7.75). After the time course, 50µL of a luciferin/luciferase kit (ATP Determination Kit, Sensitive Assay - B-Bridge International, Inc.) was directly added to 50µL of the buffered-ATP solutions and briefly mixed by pipetting the solutions in a Corning® 96-well opaque white plate. Reactions were allowed to transpire in the dark for 10min at room temperature. Luminescence was then measured using a Tecan Infinite® 200 Pro microplatereader, which was set for

a 10sec integration time and no attenuation. Sample aliquots were taken at 0, 10, 30, and 60 minutes and standardized to a pre-treatment control. ATP concentrations were also corrected for OD_{600} at the beginning and end of each time course. ATP standards were used to generate a standard curve to insure linearity and estimate intracellular ATP concentrations.

CellASIC ONIX™ Imaging

We utilized a CellASIC ONIX™ microfluidic profusion platform and accompanying microfluidic plates (Y04C) to track particles in quiescent cells. Quiescence was established by allowing cells to grow within the same SCD media for 7 days (Laporte et al., 2011). 7-day old SC media, collected from the culture by centrifuging 1mL of cells and harvesting the supernatant, was used as perfusion media in the microfluidic plate at a rate of 2psi.

Cell Volume Measurements

Cell volume measurements were performed as described in Goranov et al. (2009). In short, 1mL of cells (KWY 4736) were briefly sonicated (1sec, 2X) and diluted (1:100) into Isoton II Solution (Beckman) such that saturation levels fluctuated between 1-3% during measurements on a Beckman Coulter Multisizer 3. If oversaturation triggered warnings at any point, the run was terminated and sample repeated. The aperture was also cleaned and flushed between each run. For yeast, the particle count was set to 50,000 and for bacteria, 100,000 and smoothing set to 5. Volume counts were gated between 20 and 380 fL for statistical analysis of yeast. Median volumes in yeast biological replicates varied no more than $\pm$ 3% when standardized to logarithmic growing cells in SCD media; median volumes in bacteria varied no more than $\pm$ 0.5%.

Filamentous Actin Quantification

To quantify filamentous actin, KWY 165 cells were fixed with formaldehyde at a final concentration of 4% for 15min. Fixed cells were washed twice with potassium phosphate buffer and resuspended into PBS-BSA. Cells were then stained with Alexa Fluor 568-phalloidin (Invitrogen) and Hoechst stain. Samples were incubated in the dark at room temperature for one hour and washed again with PBS-BSA prior to imaging (Laporte et al., 2011). Background was subtracted from z-stacks (0.15µm steps over 3µm) taken with a 100X/1.49NA APO TIRF oil immersion objective using a rolling ball radius of 1 pixel in ImageJ (NIH). Maximal intensity projections were then blinded and cells classified based on the presence or absence of identifiable filamentous or bundled actin.

pH Measurements

The pHlourin calibration protocol was slightly adapted from Orij et al., (2009) to establish a standard curve. 50µg/mL (in PBS) of digitonin was used to permeabalize cells for 10min. After washing cells in PBS and placing them on ice, cells were then

incubated in citric acid/Na_2HPO_4 buffer with pH values ranging from pH 5.0 to pH 8.0. pHlourin emission intensity ratios resulting from 390nm and 470nm excitation ($R_{390nm/470nm}$) were then calculated from calibration images (taken with a 100X/1.49NA APO TIRF oil immersion objective) using a custom script in ImageJ (NIH) and compared to the pH values of the corresponding buffer. The resulting curve was used to estimate experimental intracellular pH values generated from emission ratios produced from the same ImageJ script. The standard curve and all experiments were performed using KWY 3661 expressing pHlourin.

Nuclear Volume

Nuclear volume measurements were conducted on KWY4796 cells expressing TetR-GFP (and DsRed-HDEL). Cells were grown in complete synthetic medium with 2 % dextrose overnight at 25ºC to OD 0.5-0.8. Cells were then treated as indicated and transferred to Labtek chambers (Nunc) coated with concanavalin A at OD 0.2. To wash cells into different medium conditions, cells were pelleted at 6000 rpm in a table top centrifuge and washed 4 times with synthetic medium lacking dextrose and then resuspended in synthetic medium either lacking dextrose or supplemented with 2 % dextrose. Threedimensional stacks with 0.24 um z stepping were acquired on a Zeiss Axio Observer Z1 spinning disk confocal microscope equipped with a motorized piezo stage (ASI) and an EMCCD camera (Andor Evolve) using a 100x 1.46 Oil, alpha Plan Apochromat objective. TetR-GFP was excited with a 488 nm laser line and scanned using a Quad Band "RQFT" 405/488/568/647 dichroic and a 520/35 band pass emission filter. Image stacks were processed in Imaris (Bitplane) to reconstruct nuclear volume.

FCS

For FCS measurements, KWY4343 expressing dsRed-HDEL for localization of the nucleus and free GFP or KWY 4796 expressing TetR-GFP were grown and treated as for the nuclear volume measurements. FCS measurements in the cytoplasm were carried out on a Zeiss LSM 710 microscope with an avalanche photodiode detector using a 40x 1.2NA Water C-Apochromat objective. Measurements were carried out for 30 sec exciting with a 488 nm Argon laser using a 488/594 dichroic and a 505-540 bandpass emission filter. The pinhole was set to 1 Airy unit. Curves were fit with an anomalous diffusion model with a variable offset in the Zeiss Confocar software. The structural parameter was set according to calibration measurements with free Alexa Fluor 488 dye.

Acknowledgements

We thank Nate Krefman (Drubin lab) for the TetR-3xmCherry construct, Ryan Melnyk (Coates lab) for the BW25113 strain of *E.coli*, and Robert Calderon (Niyogi lab) for access to and help with the Coulter Counter. We also thank Mikael Backlund and Sébastien Huet for guidance on the biophysical properties of intracellular diffusion and Leon Chan for critical review of the manuscript.

References

Abruzzi KC, Belostotsky DA, Chekanova JA, Dower K, Rosbash M. 3'-end formation signals modulate the association of genes with the nuclear periphery as well as mRNP dot formation. EMBO J. 2006 Sep 20;25(18):4253-62. Epub 2006 Aug 31. PubMed PMID: 16946703; PubMed Central PMCID: PMC1570430.

Adkins NL, Watts M, Georgel PT. To the 30-nm chromatin fiber and beyond. Biochim Biophys Acta. 2004 Mar 15;1677(1-3):12-23. Review. PubMed PMID: 15020041.

Ahmed S, Brickner DG, Light WH, Cajigas I, McDonough M, Froyshteter AB, Volpe T, Brickner JH. DNA zip codes control an ancient mechanism for gene targeting to the nuclear periphery. Nat Cell Biol. 2010 Feb;12(2):111-8. doi: 10.1038/ncb2011. Epub 2010 Jan 24. Erratum in: Nat Cell Biol. 2010 Mar;12(3):306. PubMed PMID: 20098417; PubMed Central PMCID: PMC2835469.

Ahmed S, Brickner JH. Regulation and epigenetic control of transcription at the nuclear periphery. Trends Genet. 2007 Aug;23(8):396-402. Epub 2007 Jun 12. Review. PubMed PMID: 17566592.

Akhtar A, Gasser SM. The nuclear envelope and transcriptional control. Nat Rev Genet. 2007 Jul;8(7):507-17. Epub 2007 Jun 5. Review. PubMed PMID: 17549064.

Albert B, Léger-Silvestre I, Normand C, Gadal O. Nuclear organization and chromatin dynamics in yeast: biophysical models or biologically driven interactions? Biochim Biophys Acta. 2012 Jun;1819(6):468-81. doi: 10.1016/j.bbagrm.2011.12.010. Epub 2012 Jan 5. Review. PubMed PMID: 22245105.

Andrulis ED, Neiman AM, Zappulla DC, Sternglanz R. Perinuclear localization of chromatin facilitates transcriptional silencing. Nature. 1998 Aug 6;394(6693):592-5. Erratum in: Nature 1998 Oct 1;395(6701):525. PubMed PMID: 9707122.

Andrulis ED, Zappulla DC, Ansari A, Perrod S, Laiosa CV, Gartenberg MR, Sternglanz R. Esc1, a nuclear periphery protein required for Sir4-based plasmid anchoring and partitioning. Mol Cell Biol. 2002 Dec;22(23):8292-301. PubMed PMID: 12417731; PubMed Central PMCID: PMC134074.

Arib G, Akhtar A. Multiple facets of nuclear periphery in gene expression control. Curr Opin Cell Biol. 2011 Jun;23(3):346-53. doi: 10.1016/j.ceb.2010.12.005. Epub 2011 Jan 15. Review. PubMed PMID: 21242077.

Ashe MP, De Long SK, Sachs AB. Glucose depletion rapidly inhibits translation initiation in yeast. Mol Biol Cell. 2000 Mar;11(3):833-48. PubMed PMID: 10712503; PubMed Central PMCID: PMC14814.

Ayscough KR, Stryker J, Pokala N, Sanders M, Crews P, Drubin DG. High rates of actin filament turnover in budding yeast and roles for actin in establishment and maintenance of cell polarity revealed using the actin inhibitor latrunculin-A. J Cell Biol. 1997 Apr 21;137(2):399-416. Erratum in: J Cell Biol 1999 Sep 6;146(5):following 1201. PubMed PMID: 9128251; PubMed Central PMCID: PMC2139767.

Baarlink C, Wang H, Grosse R. Nuclear actin network assembly by formins regulates the SRF coactivator MAL. Science. 2013 May 17;340(6134):864-7. doi: 10.1126/science.1235038. Epub 2013 Apr 4. PubMed PMID: 23558171.

Babazadeh R, Adiels CB, Smedh M, Petelenz-Kurdziel E, Goksör M, Hohmann S. Osmostress-induced cell volume loss delays yeast Hog1 signaling by limiting diffusion processes and by Hog1-specific effects. PLoS One. 2013;8(11):e80901. doi: 10.1371/journal.pone.0080901. PubMed PMID: 24278344; PubMed Central PMCID: PMC3835318.

Berger AB, Cabal GG, Fabre E, Duong T, Buc H, Nehrbass U, Olivo-Marin JC, Gadal O, Zimmer C. High-resolution statistical mapping reveals gene territories in live yeast. Nat Methods. 2008 Dec;5(12):1031-7. doi: 10.1038/nmeth.1266. Epub 2008 Nov 2. PubMed PMID: 18978785.

Blobel G. Gene gating: a hypothesis. Proc Natl Acad Sci U S A. 1985 Dec;82(24):8527-9. PubMed PMID: 3866238; PubMed Central PMCID: PMC390949.

Bolzer A, Kreth G, Solovei I, Koehler D, Saracoglu K, Fauth C, Müller S, Eils R, Cremer C, Speicher MR, Cremer T. Three-dimensional maps of all chromosomes in human male fibroblast nuclei and prometaphase rosettes. PLoS Biol. 2005 May;3(5):e157. Epub 2005 Apr 26. PubMed PMID: 15839726; PubMed Central PMCID: PMC1084335.

Bracey D, Holyoak CD, Nebe-von Caron G, Coote PJ. Determination of the intracellular pH (pHi) of growing cells of Saccharomyces cerevisiae: the effect of reduced-expression of the membrane H+-ATPase. J Microbiol Methods. 1998 Jan;31(3):113-125.

Brangwynne CP, Eckmann CR, Courson DS, Rybarska A, Hoege C, Gharakhani J, Jülicher F, Hyman AA. Germline P granules are liquid droplets that localize by controlled dissolution/condensation. Science. 2009 Jun 26;324(5935):1729-32. doi: 10.1126/science.1172046. Epub 2009 May 21. PubMed PMID: 19460965.

Brangwynne CP, Koenderink GH, MacKintosh FC, Weitz DA. Intracellular transport by active diffusion. Trends Cell Biol. 2009 Sep;19(9):423-7. doi: 10.1016/j.tcb.2009.04.004. Epub 2009 Aug 21. PubMed PMID: 19699642.

Brickner DG, Ahmed S, Meldi L, Thompson A, Light W, Young M, Hickman TL, Chu F, Fabre E, Brickner JH. Transcription factor binding to a DNA zip code controls interchromosomal clustering at the nuclear periphery. Dev Cell. 2012 Jun

12;22(6):1234-46. doi: 10.1016/j.devcel.2012.03.012. Epub 2012 May 10. PubMed PMID: 22579222; PubMed Central PMCID: PMC3376219.

Brickner DG, Cajigas I, Fondufe-Mittendorf Y, Ahmed S, Lee PC, Widom J, Brickner JH. H2A.Z-mediated localization of genes at the nuclear periphery confers epigenetic memory of previous transcriptional state. PLoS Biol. 2007 Apr;5(4):e81. PubMed PMID: 17373856; PubMed Central PMCID: PMC1828143.

Brickner JH, Walter P. Gene recruitment of the activated INO1 locus to the nuclear membrane. PLoS Biol. 2004 Nov;2(11):e342. Epub 2004 Sep 28. PubMed PMID: 15455074; PubMed Central PMCID: PMC519002.

Bystricky K, Heun P, Gehlen L, Langowski J, Gasser SM. Long-range compaction and flexibility of interphase chromatin in budding yeast analyzed by high-resolution imaging techniques. Proc Natl Acad Sci U S A. 2004 Nov 23;101(47):16495-500. Epub 2004 Nov 15. PubMed PMID: 15545610; PubMed Central PMCID: PMC534505.

Bystricky K, Laroche T, van Houwe G, Blaszczyk M, Gasser SM. Chromosome looping in yeast: telomere pairing and coordinated movement reflect anchoring efficiency and territorial organization. J Cell Biol. 2005 Jan 31;168(3):375-87. PubMed PMID: 15684028; PubMed Central PMCID: PMC2171726.

Cabal GG, Genovesio A, Rodriguez-Navarro S, Zimmer C, Gadal O, Lesne A, Buc H, Feuerbach-Fournier F, Olivo-Marin JC, Hurt EC, Nehrbass U. SAGA interacting factors confine sub-diffusion of transcribed genes to the nuclear envelope. Nature. 2006 Jun 8;441(7094):770-3. PubMed PMID: 16760982.

Capelson M, Liang Y, Schulte R, Mair W, Wagner U, Hetzer MW. Chromatin-bound nuclear pore components regulate gene expression in higher eukaryotes. Cell. 2010 Feb 5;140(3):372-83. doi: 10.1016/j.cell.2009.12.054. PubMed PMID: 20144761; PubMed Central PMCID: PMC2821818.

Carmo-Fonseca M, Platani M, Swedlow JR. Macromolecular mobility inside the cell nucleus. Trends Cell Biol. 2002 Nov;12(11):491-5. PubMed PMID: 12446102.

Casolari JM, Brown CR, Drubin DA, Rando OJ, Silver PA. Developmentally induced changes in transcriptional program alter spatial organization across chromosomes. Genes Dev. 2005 May 15;19(10):1188-98. PubMed PMID: 15905407; PubMed Central PMCID: PMC1132005.

Casolari JM, Brown CR, Komili S, West J, Hieronymus H, Silver PA. Genome-wide localization of the nuclear transport machinery couples transcriptional status and nuclear organization. Cell. 2004 May 14;117(4):427-39. PubMed PMID: 15137937.

Chambeyron S, Bickmore WA. Chromatin decondensation and nuclear reorganization of the HoxB locus upon induction of transcription. Genes Dev. 2004 May 15;18(10):1119-30. PubMed PMID: 15155579; PubMed Central PMCID: PMC415637.

Chowdhury S, Smith KW, Gustin MC. Osmotic stress and the yeast cytoskeleton: phenotype-specific suppression of an actin mutation. J Cell Biol. 1992 Aug;118(3):561-71. PubMed PMID: 1639843; PubMed Central PMCID: PMC2289551.

Chuang CH, Carpenter AE, Fuchsova B, Johnson T, de Lanerolle P, Belmont AS. Long-range directional movement of an interphase chromosome site. Curr Biol. 2006 Apr 18;16(8):825-31. PubMed PMID: 16631592.

Chubb JR, Boyle S, Perry P, Bickmore WA. Chromatin motion is constrained by association with nuclear compartments in human cells. Curr Biol. 2002 Mar 19;12(6):439-45. PubMed PMID: 11909528.

Clegg JS. Intracellular water and the cytomatrix: some methods of study and current views. J Cell Biol. 1984 Jul;99(1 Pt 2):167s-171s. Review. PubMed PMID: 6378919; PubMed Central PMCID: PMC2275590.

Conrad MN, Lee CY, Chao G, Shinohara M, Kosaka H, Shinohara A, Conchello JA, Dresser ME. Rapid telomere movement in meiotic prophase is promoted by NDJ1, MPS3, and CSM4 and is modulated by recombination. Cell. 2008 Jun 27;133(7):1175-87. doi: 10.1016/j.cell.2008.04.047. PubMed PMID: 18585352.

Cremer T, Cremer M. Chromosome territories. Cold Spring Harb Perspect Biol. 2010 Mar;2(3):a003889. doi: 10.1101/cshperspect.a003889. Review. PubMed PMID: 20300217; PubMed Central PMCID: PMC2829961.

Croft JA, Bridger JM, Boyle S, Perry P, Teague P, Bickmore WA. Differences in the localization and morphology of chromosomes in the human nucleus. J Cell Biol. 1999 Jun 14;145(6):1119-31. PubMed PMID: 10366586; PubMed Central PMCID: PMC2133153.

D'Angelo MA, Hetzer MW. The role of the nuclear envelope in cellular organization. Cell Mol Life Sci. 2006 Feb;63(3):316-32. Review. PubMed PMID: 16389459.

de Laat W, Grosveld F. Spatial organization of gene expression: the active chromatin hub. Chromosome Res. 2003;11(5):447-59. Review. PubMed PMID: 12971721.

Dechant R, Binda M, Lee SS, Pelet S, Winderickx J, Peter M. Cytosolic pH is a second messenger for glucose and regulates the PKA pathway through V-ATPase. EMBO J. 2010 Aug 4;29(15):2515-26. doi: 10.1038/emboj.2010.138. Epub 2010 Jun 25. PubMed PMID: 20581803; PubMed Central PMCID: PMC2928683.

Dekker J, Rippe K, Dekker M, Kleckner N. Capturing chromosome conformation. Science. 2002 Feb 15;295(5558):1306-11. PubMed PMID: 11847345.

Dernburg AF, Broman KW, Fung JC, Marshall WF, Philips J, Agard DA, Sedat JW. Perturbation of nuclear architecture by long-distance chromosome interactions. Cell. 1996 May 31;85(5):745-59. PubMed PMID: 8646782.

Dieker, T. 2004. Simulation of fractional brownian motion. MSc Theses, University of Twente, Amsterdam, the Netherlands.

Dieppois G, Iglesias N, Stutz F. Cotranscriptional recruitment to the mRNA export receptor Mex67p contributes to nuclear pore anchoring of activated genes. Mol Cell Biol. 2006 Nov;26(21):7858-70. Epub 2006 Sep 5. PubMed PMID: 16954382; PubMed Central PMCID: PMC1636739.

Doliwa B, Heuer A. Cage Effect, Local Anisotropies, and Dynamic Heterogeneities at the Glass Transition: A Computer Study of Hard Spheres. Phys Rev Lett.1998 Jun;80(22):4915-4918.

Drubin DA, Garakani AM, Silver PA. Motion as a phenotype: the use of live-cell imaging and machine visual screening to characterize transcription-dependent chromosome dynamics. BMC Cell Biol. 2006 Apr 24;7:19. PubMed PMID: 16635267; PubMed Central PMCID: PMC1488840.

Duan Z, Andronescu M, Schutz K, McIlwain S, Kim YJ, Lee C, Shendure J, Fields S, Blau CA, Noble WS. A three-dimensional model of the yeast genome. Nature. 2010 May 20;465(7296):363-7. doi: 10.1038/nature08973. Epub 2010 May 2. PubMed PMID: 20436457; PubMed Central PMCID: PMC2874121.

Fabry B, Maksym GN, Butler JP, Glogauer M, Navajas D, Fredberg JJ. Scaling the microrheology of living cells. Phys Rev Lett. 2001 Oct 1;87(14):148102. Epub 2001 Sep 13. PubMed PMID: 11580676.

Fels J, Orlov SN, Grygorczyk R. The hydrogel nature of mammalian cytoplasm contributes to osmosensing and extracellular pH sensing. Biophys J. 2009 May 20;96(10):4276-85. doi: 10.1016/j.bpj.2009.02.038. PubMed PMID: 19450498; PubMed Central PMCID: PMC2712211.

Felsenfeld G, Groudine M. Controlling the double helix.Nature. 2003 Jan 23;421(6921):448-53. Review. PubMed PMID: 12540921.

Fernandez-Martinez J, Rout MP. Nuclear pore complex biogenesis. Curr Opin Cell Biol. 2009 Aug;21(4):603-12. doi: 10.1016/j.ceb.2009.05.001. Epub 2009 Jun 11. Review. PubMed PMID: 19524430; PubMed Central PMCID: PMC2749478.

Feuerbach F, Galy V, Trelles-Sticken E, Fromont-Racine M, Jacquier A, Gilson E, Olivo-Marin JC, Scherthan H, Nehrbass U. Nuclear architecture and spatial positioning help establish transcriptional states of telomeres in yeast. Nat Cell Biol. 2002 Mar;4(3):214-21. PubMed PMID: 11862215.

Finlan LE, Sproul D, Thomson I, Boyle S, Kerr E, Perry P, Ylstra B, Chubb JR, Bickmore WA. Recruitment to the nuclear periphery can alter expression of genes in human cells. PLoS Genet. 2008 Mar 21;4(3):e1000039. doi: 10.1371/journal.pgen.1000039. PubMed PMID: 18369458; PubMed Central PMCID: PMC2265557.

Fischer T, Strässer K, Rácz A, Rodriguez-Navarro S, Oppizzi M, Ihrig P, Lechner J, Hurt E. The mRNA export machinery requires the novel Sac3p-Thp1p complex to dock at the nucleoplasmic entrance of the nuclear pores. EMBO J. 2002 Nov 1;21(21):5843-52. PubMed PMID: 12411502; PubMed Central PMCID: PMC131087.

Fisher AG, Merkenschlager M. Gene silencing, cell fate and nuclear organisation. Curr Opin Genet Dev. 2002 Apr;12(2):193-7. Review. PubMed PMID: 11893493.

Francastel C, Walters MC, Groudine M, Martin DI. A functional enhancer suppresses silencing of a transgene and prevents its localization close to centrometric heterochromatin. Cell. 1999 Oct 29;99(3):259-69. PubMed PMID: 10555142.

Fraser P, Bickmore W. Nuclear organization of the genome and the potential for gene regulation. Nature. 2007 May 24;447(7143):413-7. Review. PubMed PMID: 17522674.

Frey S, Richter RP, Görlich D. FG-rich repeats of nuclear pore proteins form a three-dimensional meshwork with hydrogel-like properties. Science. 2006 Nov 3;314(5800):815-7. PubMed PMID: 17082456.

Fullwood MJ, Liu MH, Pan YF, Liu J, Xu H, Mohamed YB, Orlov YL, Velkov S, Ho A, Mei PH, Chew EG, Huang PY, Welboren WJ, Han Y, Ooi HS, Ariyaratne PN, Vega VB, Luo Y, Tan PY, Choy PY, Wansa KD, Zhao B, Lim KS, Leow SC, Yow JS, Joseph R, Li H, Desai KV, Thomsen JS, Lee YK, Karuturi RK, Herve T, Bourque G, Stunnenberg HG, Ruan X, Cacheux-Rataboul V, Sung WK, Liu ET, Wei CL, Cheung E, Ruan Y. An oestrogen-receptor-alpha-bound human chromatin interactome. Nature. 2009 Nov 5;462(7269):58-64. doi: 10.1038/nature08497. PubMed PMID: 19890323; PubMed Central PMCID: PMC2774924.

Gahlmann A, Ptacin JL, Grover G, Quirin S, von Diezmann AR, Lee MK, Backlund MP, Shapiro L, Piestun R, Moerner WE. Quantitative multicolor subdiffraction imaging of bacterial protein ultrastructures in three dimensions. Nano Lett. 2013 Mar 13;13(3):987-93. doi: 10.1021/nl304071h. Epub 2013 Feb 25. PubMed PMID: 23414562; PubMed Central PMCID: PMC3599789.

Galy V, Olivo-Marin JC, Scherthan H, Doye V, Rascalou N, Nehrbass U. Nuclear pore complexes in the organization of silent telomeric chromatin. Nature. 2000 Jan 6;403(6765):108-12. PubMed PMID: 10638763.

Gartenberg MR, Neumann FR, Laroche T, Blaszczyk M, Gasser SM. Sir-mediated repression can occur independently of chromosomal and subnuclear contexts. Cell. 2004 Dec 29;119(7):955-67. PubMed PMID: 15620354.

Gasser SM, Hediger F, Taddei A, Neumann FR, Gartenberg MR. The function of telomere clustering in yeast: the circe effect. Cold Spring Harb Symp Quant Biol. 2004;69:327-37. Review. PubMed PMID: 16117665.

Goranov AI, Cook M, Ricicova M, Ben-Ari G, Gonzalez C, Hansen C, Tyers M, Amon A. The rate of cell growth is governed by cell cycle stage. Genes Dev. 2009 Jun 15;23(12):1408-22. doi: 10.1101/gad.1777309. PubMed PMID: 19528319; PubMed Central PMCID: PMC2701574.

Gotta M, Laroche T, Formenton A, Maillet L, Scherthan H, Gasser SM. The clustering of telomeres and colocalization with Rap1, Sir3, and Sir4 proteins in wild-type Saccharomyces cerevisiae. J Cell Biol. 1996 Sep;134(6):1349-63. PubMed PMID: 8830766; PubMed Central PMCID: PMC2121006.

Green EM, Jiang Y, Joyner R, Weis K. A negative feedback loop at the nuclear periphery regulates GAL gene expression. Mol Biol Cell. 2012 Apr;23(7):1367-75. doi: 10.1091/mbc.E11-06-0547. Epub 2012 Feb 9. PubMed PMID: 22323286; PubMed Central PMCID: PMC3315802.

Grimaud C, Becker PB. The dosage compensation complex shapes the conformation of the X chromosome in Drosophila. Genes Dev. 2009 Nov 1;23(21):2490-5. doi: 10.1101/gad.539509. PubMed PMID: 19884256; PubMed Central PMCID: PMC2779748.

Hajjoul H, Kocanova S, Lassadi I, Bystricky K, Bancaud A. Lab-on-Chip for fast 3D particle tracking in living cells. Lab Chip. 2009 Nov 7;9(21):3054-8. doi: 10.1039/b909016a. Epub 2009 Sep 2. PubMed PMID: 19823719.

Hajjoul H, Mathon J, Ranchon H, Goiffon I, Mozziconacci J, Albert B, Carrivain P, Victor JM, Gadal O, Bystricky K, Bancaud A. High-throughput chromatin motion tracking in living yeast reveals the flexibility of the fiber throughout the genome. Genome Res. 2013 Nov;23(11):1829-38. doi: 10.1101/gr.157008.113. Epub 2013 Sep 27. PubMed PMID: 24077391; PubMed Central PMCID: PMC3814883.

Halley JE, Kaplan T, Wang AY, Kobor MS, Rine J. Roles for H2A.Z and its acetylation in GAL1 transcription and gene induction, but not GAL1-transcriptional memory. PLoS Biol. 2010 Jun 22;8(6):e1000401. doi: 10.1371/journal.pbio.1000401. PubMed PMID: 20582323; PubMed Central PMCID: PMC2889906.

Hediger F, Neumann FR, Van Houwe G, Dubrana K, Gasser SM. Live imaging of telomeres: yKu and Sir proteins define redundant telomere-anchoring pathways in yeast. Curr Biol. 2002 Dec 23;12(24):2076-89. PubMed PMID: 12498682.

Heun P, Laroche T, Shimada K, Furrer P, Gasser SM. Chromosome dynamics in the yeast interphase nucleus. Science. 2001 Dec 7;294(5549):2181-6. PubMed PMID: 11739961.

Hiraoka Y, Dernburg AF. The SUN rises on meiotic chromosome dynamics. Dev Cell. 2009 Nov;17(5):598-605. doi: 10.1016/j.devcel.2009.10.014. Review. PubMed PMID: 19922865.

Hübner MR, Spector DL. Chromatin dynamics. Annu Rev Biophys. 2010;39:471-89. doi: 10.1146/annurev.biophys.093008.131348. Review. PubMed PMID: 20462379; PubMed Central PMCID: PMC2894465.

Ishii K, Arib G, Lin C, Van Houwe G, Laemmli UK. Chromatin boundaries in budding yeast: the nuclear pore connection. Cell. 2002 May 31;109(5):551-62. PubMed PMID: 12062099.

Jacobs CW, Adams AE, Szaniszlo PJ, Pringle JR. Functions of microtubules in the Saccharomyces cerevisiae cell cycle. J Cell Biol. 1988 Oct;107(4):1409-26. PubMed PMID: 3049620; PubMed Central PMCID: PMC2115239.

Jani D, Lutz S, Marshall NJ, Fischer T, Köhler A, Ellisdon AM, Hurt E, Stewart M. Sus1, Cdc31, and the Sac3 CID region form a conserved interaction platform that promotes nuclear pore association and mRNA export. Mol Cell. 2009 Mar 27;33(6):727-37. doi: 10.1016/j.molcel.2009.01.033. PubMed PMID: 19328066; PubMed Central PMCID: PMC2726291.

Jenuwein T, Allis CD. Translating the histone code. Science. 2001 Aug 10;293(5532):1074-80. Review. PubMed PMID: 11498575.

Johnston M, Flick JS, Pexton T. Multiple mechanisms provide rapid and stringent glucose repression of GAL gene expression in Saccharomyces cerevisiae. Mol Cell Biol. 1994 Jun;14(6):3834-41. PubMed PMID: 8196626; PubMed Central PMCID: PMC358750.

Jorgensen P, Nishikawa JL, Breitkreutz BJ, Tyers M. Systematic identification of pathways that couple cell growth and division in yeast. Science. 2002 Jul 19;297(5580):395-400. Epub 2002 Jun 27. PubMed PMID: 12089449.

Kalverda B, Pickersgill H, Shloma VV, Fornerod M. Nucleoporins directly stimulate expression of developmental and cell-cycle genes inside the nucleoplasm. Cell. 2010 Feb 5;140(3):360-71. doi: 10.1016/j.cell.2010.01.011. PubMed PMID: 20144760.

Karpen GH, Schaefer JE, Laird CD. A Drosophila rRNA gene located in euchromatin is active in transcription and nucleolus formation. Genes Dev. 1988 Dec;2(12B):1745-63. PubMed PMID: 3149250.

Knull H, Minton AP. Structure within eukaryotic cytoplasm and its relationship to glycolytic metabolism. Cell Biochem Funct. 1996 Dec;14(4):237-48. Review. PubMed PMID: 8952042.

Köhler A, Schneider M, Cabal GG, Nehrbass U, Hurt E. Yeast Ataxin-7 links histone deubiquitination with gene gating and mRNA export. Nat Cell Biol. 2008 Jun;10(6):707-15. doi: 10.1038/ncb1733. Epub 2008 May 18. PubMed PMID: 18488019.

Kosak ST, Skok JA, Medina KL, Riblet R, Le Beau MM, Fisher AG, Singh H. Subnuclear compartmentalization of immunoglobulin loci during lymphocyte development. Science. 2002 Apr 5;296(5565):158-62. PubMed PMID: 11935030.

Koszul R, Kim KP, Prentiss M, Kleckner N, Kameoka S. Meiotic chromosomes move by linkage to dynamic actin cables with transduction of force through the nuclear envelope. Cell. 2008 Jun 27;133(7):1188-201. doi: 10.1016/j.cell.2008.04.050. PubMed PMID: 18585353; PubMed Central PMCID: PMC2601696.

Kumaran RI, Spector DL. A genetic locus targeted to the nuclear periphery in living cells maintains its transcriptional competence. J Cell Biol. 2008 Jan 14;180(1):51-65. doi: 10.1083/jcb.200706060. PubMed PMID: 18195101; PubMed Central PMCID: PMC2213611.

Kurshakova MM, Krasnov AN, Kopytova DV, Shidlovskii YV, Nikolenko JV, Nabirochkina EN, Spehner D, Schultz P, Tora L, Georgieva SG. SAGA and a novel Drosophila export complex anchor efficient transcription and mRNA export to NPC. EMBO J. 2007 Dec 12;26(24):4956-65. Epub 2007 Nov 22. PubMed PMID: 18034162; PubMed Central PMCID: PMC2140098.

Lagorce A, Le Berre-Anton V, Aguilar-Uscanga B, Martin-Yken H, Dagkessamanskaia A, François J. Involvement of GFA1, which encodes glutamine-fructose-6-phosphate amidotransferase, in the activation of the chitin synthesis pathway in response to cell-wall defects in Saccharomyces cerevisiae. Eur J Biochem. 2002 Mar;269(6):1697-707. Erratum in: Eur J Biochem. 2006 Aug;273(16):3869. PubMed PMID: 11895440.

Lainé JP, Singh BN, Krishnamurthy S, Hampsey M. A physiological role for gene loops in yeast. Genes Dev. 2009 Nov 15;23(22):2604-9. doi: 10.1101/gad.1823609. PubMed PMID: 19933150; PubMed Central PMCID: PMC2779762.

Lanctôt C, Cheutin T, Cremer M, Cavalli G, Cremer T. Dynamic genome architecture in the nuclear space: regulation of gene expression in three dimensions. Nat Rev Genet. 2007 Feb;8(2):104-15. Review. PubMed PMID: 17230197.

Laporte D, Lebaudy A, Sahin A, Pinson B, Ceschin J, Daignan-Fornier B, Sagot I. Metabolic status rather than cell cycle signals control quiescence entry and exit. J Cell Biol. 2011 Mar 21;192(6):949-57. doi: 10.1083/jcb.201009028. Epub 2011 Mar 14. PubMed PMID: 21402786; PubMed Central PMCID: PMC3063145.

Latulippe DR, Zydney AL. Radius of gyration of plasmid DNA isoforms from static light scattering. Biotechnol Bioeng. 2010 Sep 1;107(1):134-42. doi: 10.1002/bit.22787. PubMed PMID: 20506212.

Liang Y, Hetzer MW. Functional interactions between nucleoporins and chromatin. Curr Opin Cell Biol. 2011 Feb;23(1):65-70. doi: 10.1016/j.ceb.2010.09.008. Epub 2010 Oct 26. Review. PubMed PMID: 21030234; PubMed Central PMCID: PMC3753814.

Lieberman-Aiden E, van Berkum NL, Williams L, Imakaev M, Ragoczy T, Telling A, Amit I, Lajoie BR, Sabo PJ, Dorschner MO, Sandstrom R, Bernstein B, Bender MA, Groudine M, Gnirke A, Stamatoyannopoulos J, Mirny LA, Lander ES, Dekker J. Comprehensive mapping of long-range interactions reveals folding principles of the human genome. Science. 2009 Oct 9;326(5950):289-93. doi: 10.1126/science.1181369. PubMed PMID: 19815776; PubMed Central PMCID: PMC2858594.

Light WH, Brickner DG, Brand VR, Brickner JH. Interaction of a DNA zip code with the nuclear pore complex promotes H2A.Z incorporation and INO1 transcriptional memory. Mol Cell. 2010 Oct 8;40(1):112-25. doi: 10.1016/j.molcel.2010.09.007. PubMed PMID: 20932479; PubMed Central PMCID: PMC2953765.

Lim RY, Fahrenkrog B. The nuclear pore complex up close.Curr Opin Cell Biol. 2006 Jun;18(3):342-7. Epub 2006 May 2. Review. PubMed PMID: 16631361.

Longtine MS, McKenzie A 3rd, Demarini DJ, Shah NG, Wach A, Brachat A, Philippsen P, Pringle JR. Additional modules for versatile and economical PCR-based gene deletion and modification in Saccharomyces cerevisiae. Yeast. 1998 Jul;14(10):953-61. PubMed PMID: 9717241.

Luby-Phelps K. Cytoarchitecture and physical properties of cytoplasm: volume, viscosity, diffusion, intracellular surface area. Int Rev Cytol. 2000;192:189-221. Review. PubMed PMID: 10553280.

Luthra R, Kerr SC, Harreman MT, Apponi LH, Fasken MB, Ramineni S, Chaurasia S, Valentini SR, Corbett AH. Actively transcribed GAL genes can be physically linked to the nuclear pore by the SAGA chromatin modifying complex. J Biol Chem. 2007 Feb 2;282(5):3042-9. Epub 2006 Dec 6. PubMed PMID: 17158105.

Madrid AS, Mancuso J, Cande WZ, Weis K. The role of the integral membrane nucleoporins Ndc1p and Pom152p in nuclear pore complex assembly and function. J

Cell Biol. 2006 May 8;173(3):361-71. PubMed PMID: 16682526; PubMed Central PMCID: PMC2063837.

Mahy NL, Perry PE, Bickmore WA. Gene density and transcription influence the localization of chromatin outside of chromosome territories detectable by FISH. J Cell Biol. 2002 Dec 9;159(5):753-63. Epub 2002 Dec 9. PubMed PMID: 12473685; PubMed Central PMCID: PMC2173389.

Mandadapu KK, Govindjee S, Mofrad MR. On the cytoskeleton and soft glassy rheology. J Biomech. 2008;41(7):1467-78. doi: 10.1016/j.jbiomech.2008.02.014. Epub 2008 Apr 9. PubMed PMID: 18402964.

Marshall WF, Straight A, Marko JF, Swedlow J, Dernburg A, Belmont A, Murray AW, Agard DA, Sedat JW. Interphase chromosomes undergo constrained diffusional motion in living cells. Curr Biol. 1997 Dec 1;7(12):930-9. PubMed PMID: 9382846.

Martin DS, Forstner MB, Käs JA. Apparent subdiffusion inherent to single particle tracking. Biophys J. 2002 Oct;83(4):2109-17. PubMed PMID: 12324428; PubMed Central PMCID: PMC1302299.

Mendjan S, Taipale M, Kind J, Holz H, Gebhardt P, Schelder M, Vermeulen M, Buscaino A, Duncan K, Mueller J, Wilm M, Stunnenberg HG, Saumweber H, Akhtar A. Nuclear pore components are involved in the transcriptional regulation of dosage compensation in Drosophila. Mol Cell. 2006 Mar 17;21(6):811-23. PubMed PMID: 16543150.

Meneghini MD, Wu M, Madhani HD. Conserved histone variant H2A.Z protects euchromatin from the ectopic spread of silent heterochromatin. Cell. 2003 Mar 7;112(5):725-36. PubMed PMID: 12628191.

Menon BB, Sarma NJ, Pasula S, Deminoff SJ, Willis KA, Barbara KE, Andrews B, Santangelo GM. Reverse recruitment: the Nup84 nuclear pore subcomplex mediates Rap1/Gcr1/Gcr2 transcriptional activation. Proc Natl Acad Sci U S A. 2005 Apr 19;102(16):5749-54. Epub 2005 Apr 7. PubMed PMID: 15817685; PubMed Central PMCID: PMC556015.

Miermont A, Waharte F, Hu S, McClean MN, Bottani S, Léon S, Hersen P. Severe osmotic compression triggers a slowdown of intracellular signaling, which can be explained by molecular crowding. Proc Natl Acad Sci U S A. 2013 Apr 2;110(14):5725-30. doi: 10.1073/pnas.1215367110. Epub 2013 Mar 14. PubMed PMID: 23493557; PubMed Central PMCID: PMC3619343.

Miesenböck G, De Angelis DA, Rothman JE. Visualizing secretion and synaptic transmission with pH-sensitive green fluorescent proteins. Nature. 1998 Jul 9;394(6689):192-5. PubMed PMID: 9671304.

Misteli T. Beyond the sequence: cellular organization of genome function. Cell. 2007 Feb 23;128(4):787-800. Review. PubMed PMID: 17320514.

Morrissey JP, Deardorff JA, Hebron C, Sachs AB. Decapping of stabilized, polyadenylated mRNA in yeast pab1 mutants. Yeast. 1999 Jun 15;15(8):687-702. PubMed PMID: 10392446.

Narayanaswamy R, Levy M, Tsechansky M, Stovall GM, O'Connell JD, Mirrielees J, Ellington AD, Marcotte EM. Widespread reorganization of metabolic enzymes into reversible assemblies upon nutrient starvation. Proc Natl Acad Sci U S A. 2009 Jun 23;106(25):10147-52. doi: 10.1073/pnas.0812771106. Epub 2009 Jun 5. PubMed PMID: 19502427; PubMed Central PMCID: PMC2691686.

Neumann FR, Dion V, Gehlen LR, Tsai-Pflugfelder M, Schmid R, Taddei A, Gasser SM. Targeted INO80 enhances subnuclear chromatin movement and ectopic homologous recombination. Genes Dev. 2012 Feb 15;26(4):369-83. doi: 10.1101/gad.176156.111. PubMed PMID: 22345518; PubMed Central PMCID: PMC3289885.

Neumann FR, Nurse P. Nuclear size control in fission yeast. J Cell Biol. 2007 Nov 19;179(4):593-600. Epub 2007 Nov 12. PubMed PMID: 17998401; PubMed Central PMCID: PMC2080919.

Orij R, Postmus J, Ter Beek A, Brul S, Smits GJ. In vivo measurement of cytosolic and mitochondrial pH using a pH-sensitive GFP derivative in Saccharomyces cerevisiae reveals a relation between intracellular pH and growth. Microbiology. 2009 Jan;155(Pt 1):268-78. doi: 10.1099/mic.0.022038-0. PubMed PMID: 19118367.

Osborne CS, Chakalova L, Brown KE, Carter D, Horton A, Debrand E, Goyenechea B, Mitchell JA, Lopes S, Reik W, Fraser P. Active genes dynamically colocalize to shared sites of ongoing transcription. Nat Genet. 2004 Oct;36(10):1065-71. Epub 2004 Sep 7. PubMed PMID: 15361872.

O'Sullivan JM, Tan-Wong SM, Morillon A, Lee B, Coles J, Mellor J, Proudfoot NJ. Gene loops juxtapose promoters and terminators in yeast. Nat Genet. 2004 Sep;36(9):1014-8. Epub 2004 Aug 15. PubMed PMID: 15314641.

Ozalp VC, Pedersen TR, Nielsen LJ, Olsen LF. Time-resolved measurements of intracellular ATP in the yeast Saccharomyces cerevisiae using a new type of nanobiosensor. J Biol Chem. 2010 Nov 26;285(48):37579-88. doi: 10.1074/jbc.M110.155119. Epub 2010 Sep 29. PubMed PMID: 20880841; PubMed Central PMCID: PMC2988363.

Parry BR, Surovtsev IV, Cabeen MT, O'Hern CS, Dufresne ER, Jacobs-Wagner C. The Bacterial Cytoplasm Has Glass-like Properties and Is Fluidized by Metabolic

Activity. Cell. 2014 Jan 16;156(1-2):183-94. doi: 10.1016/j.cell.2013.11.028. Epub 2013 Dec 19. PubMed PMID: 24361104.

Pavani SR, Thompson MA, Biteen JS, Lord SJ, Liu N, Twieg RJ, Piestun R, Moerner WE. Three-dimensional, single-molecule fluorescence imaging beyond the diffraction limit by using a double-helix point spread function. Proc Natl Acad Sci U S A. 2009 Mar 3;106(9):2995-9. doi: 10.1073/pnas.0900245106. Epub 2009 Feb 11. PubMed PMID: 19211795; PubMed Central PMCID: PMC2651341.

Pelletier V, Gal N, Fournier P, Kilfoil ML. Microrheology of microtubule solutions and actin-microtubule composite networks. Phys Rev Lett. 2009 May 8;102(18):188303. Epub 2009 May 7. PubMed PMID: 19518917.

Peters LZ, Hazan R, Breker M, Schuldiner M, Ben-Aroya S. Formation and dissociation of proteasome storage granules are regulated by cytosolic pH. J Cell Biol. 2013 May 27;201(5):663-71. doi: 10.1083/jcb.201211146. Epub 2013 May 20. PubMed PMID: 23690178; PubMed Central PMCID: PMC3664706.

Pickersgill H, Kalverda B, de Wit E, Talhout W, Fornerod M, van Steensel B. Characterization of the Drosophila melanogaster genome at the nuclear lamina. Nat Genet. 2006 Sep;38(9):1005-14. Epub 2006 Jul 30. PubMed PMID: 16878134.

Piper P, Calderon CO, Hatzixanthis K, Mollapour M. Weak acid adaptation: the stress response that confers yeasts with resistance to organic acid food preservatives. Microbiology. 2001 Oct;147(Pt 10):2635-42. Review. PubMed PMID: 11577142.

Pliss A, Malyavantham KS, Bhattacharya S, Berezney R. Chromatin dynamics in living cells: identification of oscillatory motion. J Cell Physiol. 2013 Mar;228(3):609-16. doi: 10.1002/jcp.24169. PubMed PMID: 22886456.

Qian H, Sheetz MP, Elson EL. Single particle tracking. Analysis of diffusion and flow in two-dimensional systems. Biophys J. 1991 Oct;60(4):910-21. PubMed PMID: 1742458; PubMed Central PMCID: PMC1260142.

Ragoczy T, Bender MA, Telling A, Byron R, Groudine M. The locus control region is required for association of the murine beta-globin locus with engaged transcription factories during erythroid maturation. Genes Dev. 2006 Jun 1;20(11):1447-57. Epub 2006 May 16. PubMed PMID: 16705039; PubMed Central PMCID: PMC1475758.

Ramachandran V, Shah KH, Herman PK. The cAMP-dependent protein kinase signaling pathway is a key regulator of P body foci formation. Mol Cell. 2011 Sep 16;43(6):973-81. doi: 10.1016/j.molcel.2011.06.032. PubMed PMID: 21925385; PubMed Central PMCID: PMC3176436.

Reddy KL, Zullo JM, Bertolino E, Singh H. Transcriptional repression mediated by repositioning of genes to the nuclear lamina. Nature. 2008 Mar 13;452(7184):243-7. doi: 10.1038/nature06727. Epub 2008 Feb 13. PubMed PMID: 18272965.

Ren B, Robert F, Wyrick JJ, Aparicio O, Jennings EG, Simon I, Zeitlinger J, Schreiber J, Hannett N, Kanin E, Volkert TL, Wilson CJ, Bell SP, Young RA. Genome-wide location and function of DNA binding proteins. Science. 2000 Dec 22;290(5500):2306-9. PubMed PMID: 11125145.

Rodríguez-Navarro S, Fischer T, Luo MJ, Antúnez O, Brettschneider S, Lechner J, Pérez-Ortín JE, Reed R, Hurt E. Sus1, a functional component of the SAGA histone acetylase complex and the nuclear pore-associated mRNA export machinery. Cell. 2004 Jan 9;116(1):75-86. PubMed PMID: 14718168.

Ross CA, Poirier MA. Protein aggregation and neurodegenerative disease. Nat Med. 2004 Jul;10 Suppl:S10-7. Review. PubMed PMID: 15272267.

Roy R, Meier B, McAinsh AD, Feldmann HM, Jackson SP.Separation-of-function mutants of yeast Ku80 reveal a Yku80p-Sir4p interaction involved in telomeric silencing. J Biol Chem. 2004 Jan 2;279(1):86-94. Epub 2003 Oct 9. PubMed PMID: 14551211.

Ruiz A, Xu X, Carlson M. Roles of two protein phosphatases, Reg1-Glc7 and Sit4, and glycogen synthesis in regulation of SNF1 protein kinase. Proc Natl Acad Sci U S A. 2011 Apr 19;108(16):6349-54. doi: 10.1073/pnas.1102758108. Epub 2011 Apr 4. PubMed PMID: 21464305; PubMed Central PMCID: PMC3081026.

Rusche LN, Kirchmaier AL, Rine J. The establishment, inheritance, and function of silenced chromatin in Saccharomyces cerevisiae. Annu Rev Biochem. 2003;72:481-516. Epub 2003 Mar 27. Review. PubMed PMID: 12676793.

Sage D, Neumann FR, Hediger F, Gasser SM, Unser M. Automatic tracking of individual fluorescence particles: application to the study of chromosome dynamics. IEEE Trans Image Process. 2005 Sep;14(9):1372-83. PubMed PMID: 16190472.

Sagot I, Pinson B, Salin B, Daignan-Fornier B. Actin bodies in yeast quiescent cells: an immediately available actin reserve? Mol Biol Cell. 2006 Nov;17(11):4645-55. Epub 2006 Aug 16. PubMed PMID: 16914523; PubMed Central PMCID: PMC1635378.

Santangelo GM. Glucose signaling in Saccharomyces cerevisiae. Microbiol Mol Biol Rev. 2006 Mar;70(1):253-82. Review. PubMed PMID: 16524925; PubMed Central PMCID: PMC1393250.

Sarma NJ, Buford TD, Haley T, Barbara-Haley K, Santangelo GM, Willis KA. The nuclear pore complex mediates binding of the Mig1 repressor to target promoters. PLoS

One. 2011;6(11):e27117. doi: 10.1371/journal.pone.0027117. Epub 2011 Nov 14. PubMed PMID: 22110603; PubMed Central PMCID: PMC3215702.

Sarma NJ, Haley TM, Barbara KE, Buford TD, Willis KA, Santangelo GM. Glucose-responsive regulators of gene expression in Saccharomyces cerevisiae function at the nuclear periphery via a reverse recruitment mechanism. Genetics. 2007 Mar;175(3):1127-35. Epub 2007 Jan 21. PubMed PMID: 17237508; PubMed Central PMCID: PMC1840092.

Savin T, Doyle PS. Static and dynamic errors in particle tracking microrheology. Biophys J. 2005 Jan;88(1):623-38. Epub 2004 Nov 8. PubMed PMID: 15533928; PubMed Central PMCID: PMC1305040.

Schlaich NL, Hurt EC. Analysis of nucleocytoplasmic transport and nuclear envelope structure in yeast disrupted for the gene encoding the nuclear pore protein Nup1p. Eur J Cell Biol. 1995 May;67(1):8-14. PubMed PMID: 7641732.

Schmid M, Arib G, Laemmli C, Nishikawa J, Durussel T, Laemmli UK. Nup-PI: the nucleopore-promoter interaction of genes in yeast. Mol Cell. 2006 Feb 3;21(3):379-91. PubMed PMID: 16455493.

Schober H, Ferreira H, Kalck V, Gehlen LR, Gasser SM. Yeast telomerase and the SUN domain protein Mps3 anchor telomeres and repress subtelomeric recombination. Genes Dev. 2009 Apr 15;23(8):928-38. doi: 10.1101/gad.1787509. PubMed PMID: 19390087; PubMed Central PMCID: PMC2675861.

Schwelberger HG, Kohlwein SD, Paltauf F. Molecular cloning, primary structure and disruption of the structural gene of aldolase from Saccharomyces cerevisiae. Eur J Biochem. 1989 Mar 15;180(2):301-8. PubMed PMID: 2647491.

Shav-Tal Y, Darzacq X, Shenoy SM, Fusco D, Janicki SM, Spector DL, Singer RH. Dynamics of single mRNPs in nuclei of living cells. Science. 2004 Jun 18;304(5678):1797-800. PubMed PMID: 15205532.

Shaw LC, Lewin AS. The Cbp2 protein stimulates the splicing of the omega intron of yeast mitochondria. Nucleic Acids Res. 1997 Apr 15;25(8):1597-604. PubMed PMID: 9092668; PubMed Central PMCID: PMC146636.

Spagnol ST, Noel Dahl K. Active cytoskeletal force and chromatin condensation independently modulate intranuclear network fluctuations. Integr Biol (Camb). 2014 Mar 12. [Epub ahead of print] PubMed PMID: 24619297.

Straight AF, Belmont AS, Robinett CC, Murray AW. GFP tagging of budding yeast chromosomes reveals that protein-protein interactions can mediate sister chromatid cohesion. Curr Biol. 1996 Dec 1;6(12):1599-608. PubMed PMID: 8994824.

Sutherland H, Bickmore WA. Transcription factories: gene expression in unions? Nat Rev Genet. 2009 Jul;10(7):457-66. doi: 10.1038/nrg2592. Review. PubMed PMID: 19506577.

Taddei A, Hediger F, Neumann FR, Bauer C, Gasser SM.Separation of silencing from perinuclear anchoring functions in yeast Ku80, Sir4 and Esc1 proteins. EMBO J. 2004 Mar 24;23(6):1301-12. Epub 2004 Mar 11. PubMed PMID: 15014445; PubMed Central PMCID: PMC381416.

Taddei A, Hediger F, Neumann FR, Gasser SM. The function of nuclear architecture: a genetic approach. Annu Rev Genet. 2004;38:305-45. Review. PubMed PMID: 15568979.

Taddei A, Van Houwe G, Hediger F, Kalck V, Cubizolles F, Schober H, Gasser SM. Nuclear pore association confers optimal expression levels for an inducible yeast gene. Nature. 2006 Jun 8;441(7094):774-8. PubMed PMID: 16760983.

Taddei A. Active genes at the nuclear pore complex. Curr Opin Cell Biol. 2007 Jun;19(3):305-10. Epub 2007 Apr 27. Review. PubMed PMID: 17467257.

Tanaka K, Tanaka TU. Live cell imaging of kinetochore capture by microtubules in budding yeast. Methods Mol Biol. 2009;545:233-42. doi: 10.1007/978-1-60327-993-2_14. PubMed PMID: 19475392.

Tang L, Nogales E, Ciferri C. Structure and function of SWI/SNF chromatin remodeling complexes and mechanistic implications for transcription. Prog Biophys Mol Biol. 2010 Jun-Jul;102(2-3):122-8. doi: 10.1016/j.pbiomolbio.2010.05.001. Epub 2010 May 20. Review. PubMed PMID: 20493208; PubMed Central PMCID: PMC2924208.

Tan-Wong SM, Wijayatilake HD, Proudfoot NJ. Gene loops function to maintain transcriptional memory through interaction with the nuclear pore complex. Genes Dev. 2009 Nov 15;23(22):2610-24. doi: 10.1101/gad.1823209. PubMed PMID: 19933151; PubMed Central PMCID: PMC2779764.

Texari L, Dieppois G, Vinciguerra P, Contreras MP, Groner A, Letourneau A, Stutz F. The nuclear pore regulates GAL1 gene transcription by controlling the localization of the SUMO protease Ulp1. Mol Cell. 2013 Sep 26;51(6):807-18. doi: 10.1016/j.molcel.2013.08.047. PubMed PMID: 24074957.

Thompson MA, Casolari JM, Badieirostami M, Brown PO, Moerner WE. Three-dimensional tracking of single mRNA particles in Saccharomyces cerevisiae using a double-helix point spread function. Proc Natl Acad Sci U S A. 2010 Oct 19;107(42):17864-71. doi: 10.1073/pnas.1012868107. Epub 2010 Oct 4. PubMed PMID: 20921361; PubMed Central PMCID: PMC2964242.

Tolhuis B, Palstra RJ, Splinter E, Grosveld F, de Laat W.Looping and interaction between hypersensitive sites in the active beta-globin locus. Mol Cell. 2002 Dec;10(6):1453-65. PubMed PMID: 12504019.

Tolić-Nørrelykke IM, Munteanu EL, Thon G, Oddershede L, Berg-Sørensen K. Anomalous diffusion in living yeast cells. Phys Rev Lett. 2004 Aug 13;93(7):078102. Epub 2004 Aug 13. PubMed PMID: 15324280.

Uesono Y, Ashe MP, Toh-E A. Simultaneous yet independent regulation of actin cytoskeletal organization and translation initiation by glucose in Saccharomyces cerevisiae. Mol Biol Cell. 2004 Apr;15(4):1544-56. Epub 2004 Jan 23. PubMed PMID: 14742701; PubMed Central PMCID: PMC379254.

Uesono Y, Toh-E A. Transient inhibition of translation initiation by osmotic stress. J Biol Chem. 2002 Apr 19;277(16):13848-55. Epub 2002 Jan 16. PubMed PMID: 11796711.

Vagnarelli P. Mitotic chromosome condensation in vertebrates. Exp Cell Res. 2012 Jul 15;318(12):1435-41. doi: 10.1016/j.yexcr.2012.03.017. Epub 2012 Mar 27. Review. PubMed PMID: 22475678.

Van de Vosse DW, Wan Y, Lapetina DL, Chen WM, Chiang JH, Aitchison JD, Wozniak RW. A role for the nucleoporin Nup170p in chromatin structure and gene silencing. Cell. 2013 Feb 28;152(5):969-83. doi: 10.1016/j.cell.2013.01.049. PubMed PMID: 23452847; PubMed Central PMCID: PMC3690833.

Vaquerizas JM, Suyama R, Kind J, Miura K, Luscombe NM, Akhtar A. Nuclear pore proteins nup153 and megator define transcriptionally active regions in the Drosophila genome. PLoS Genet. 2010 Feb 12;6(2):e1000846. doi: 10.1371/journal.pgen.1000846. PubMed PMID: 20174442; PubMed Central PMCID: PMC2820533.

Vazquez J, Belmont AS, Sedat JW. Multiple regimes of constrained chromosome motion are regulated in the interphase Drosophila nucleus. Curr Biol. 2001 Aug 21;11(16):1227-39. PubMed PMID: 11525737.

Vodala S, Abruzzi KC, Rosbash M. The nuclear exosome and adenylation regulate posttranscriptional tethering of yeast GAL genes to the nuclear periphery. Mol Cell. 2008 Jul 11;31(1):104-13. doi: 10.1016/j.molcel.2008.05.015. PubMed PMID: 18614049; PubMed Central PMCID: PMC2753219.

Volpi EV, Chevret E, Jones T, Vatcheva R, Williamson J, Beck S, Campbell RD, Goldsworthy M, Powis SH, Ragoussis J, Trowsdale J, Sheer D. Large-scale chromatin organization of the major histocompatibility complex and other regions of human chromosome 6 and its response to interferon in interphase nuclei. J Cell Sci. 2000 May;113 (Pt 9):1565-76. PubMed PMID: 10751148.

Weber SC, Spakowitz AJ, Theriot JA. Bacterial chromosomal loci move subdiffusively through a viscoelastic cytoplasm. Phys Rev Lett. 2010 Jun 11;104(23):238102. Epub 2010 Jun 8. PubMed PMID: 20867274.

Weber SC, Spakowitz AJ, Theriot JA. Nonthermal ATP-dependent fluctuations contribute to the in vivo motion of chromosomal loci. Proc Natl Acad Sci U S A. 2012 May 8;109(19):7338-43. doi: 10.1073/pnas.1119505109. Epub 2012 Apr 19. PubMed PMID: 22517744; PubMed Central PMCID: PMC3358901.

Weber SC, Theriot JA, Spakowitz AJ. Subdiffusive motion of a polymer composed of subdiffusive monomers. Phys Rev E Stat Nonlin Soft Matter Phys. 2010 Jul;82(1 Pt 1):011913. Epub 2010 Jul 19. PubMed PMID: 20866654.

Weber SC, Thompson MA, Moerner WE, Spakowitz AJ, Theriot JA. Analytical tools to distinguish the effects of localization error, confinement, and medium elasticity on the velocity autocorrelation function. Biophys J. 2012 Jun 6;102(11):2443-50. doi: 10.1016/j.bpj.2012.03.062. Epub 2012 Jun 5. PubMed PMID: 22713559; PubMed Central PMCID: PMC3368140.

Weeks ER, Crocker JC, Levitt AC, Schofield A, Weitz DA. Three-dimensional direct imaging of structural relaxation near the colloidal glass transition. Science. 2000 Jan 28;287(5453):627-31. PubMed PMID: 10649991.

Wegel E, Shaw P. Gene activation and deactivation related changes in the three-dimensional structure of chromatin.Chromosoma. 2005 Nov;114(5):331-7. Epub 2005 Nov 12. Review. PubMed PMID: 16075283.

Weis K. Regulating access to the genome: nucleocytoplasmic transport throughout the cell cycle. Cell. 2003 Feb 21;112(4):441-51. Review. PubMed PMID: 12600309.

Weis K. The nuclear pore complex: oily spaghetti or gummy bear? Cell. 2007 Aug 10;130(3):405-7. Review. PubMed PMID: 17693250.

Wilmes GM, Guthrie C. Getting to the gate: crystallization of a Sac3(CID):Sus1:Cdc31 complex. Mol Cell. 2009 Mar 27;33(6):671-2. doi: 10.1016/j.molcel.2009.03.003. PubMed PMID: 19328059.

Yao J, Ardehali MB, Fecko CJ, Webb WW, Lis JT. Intranuclear distribution and local dynamics of RNA polymerase II during transcription activation. Mol Cell. 2007 Dec 28;28(6):978-90. PubMed PMID: 18158896.

Yoshida T, Shimada K, Oma Y, Kalck V, Akimura K, Taddei A, Iwahashi H, Kugou K, Ohta K, Gasser SM, Harata M. Actin-related protein Arp6 influences H2A.Z-dependent and -independent gene expression and links ribosomal protein genes to nuclear pores.PLoS Genet. 2010 Apr 15;6(4):e1000910. doi: 10.1371/journal.pgen.1000910. PubMed PMID: 20419146; PubMed Central PMCID: PMC2855322.

Young BP, Shin JJ, Orij R, Chao JT, Li SC, Guan XL, Khong A, Jan E, Wenk MR, Prinz WA, Smits GJ, Loewen CJ. Phosphatidic acid is a pH biosensor that links membrane biogenesis to metabolism. Science. 2010 Aug 27;329(5995):1085-8. doi: 10.1126/science.1191026. PubMed PMID: 20798321.

Zarnack K, Feldbrügge M. mRNA trafficking in fungi. Mol Genet Genomics. 2007 Oct;278(4):347-59. Epub 2007 Sep 1. Review. PubMed PMID: 17768642.

Zeitler B, Weis K. The FG-repeat asymmetry of the nuclear pore complex is dispensable for bulk nucleocytoplasmic transport in vivo. J Cell Biol. 2004 Nov 22;167(4):583-90. PubMed PMID: 15557115; PubMed Central PMCID: PMC2172579.

Zhou C, Slaughter BD, Unruh JR, Eldakak A, Rubinstein B, Li R. Motility and segregation of Hsp104-associated protein aggregates in budding yeast. Cell. 2011 Nov 23;147(5):1186-96. doi: 10.1016/j.cell.2011.11.002. PubMed PMID: 22118470; PubMed Central PMCID: PMC3237388.

Zidovska A, Weitz DA, Mitchison TJ. Micron-scale coherence in interphase chromatin dynamics. Proc Natl Acad Sci U S A. 2013 Sep 24;110(39):15555-60. doi: 10.1073/pnas.1220313110. Epub 2013 Sep 9. PubMed PMID: 24019504; PubMed Central PMCID: PMC3785772.

Appendix:

The relationship between *REG1*, intracellular pH, and starvation

Background

Our previous results (**Chap 4**) indicated that the starvation-induced cell contraction and subsequent molecular crowding is sufficient to confine macromolecular mobility and depolymerize the actin cytoskeleton. However, this work did not identify the signaling pathways or mechanism by which starvation prompts a loss of cell volume. Interestingly, a deletion of *REG1*, the negative regulator of Snf1-kinase, is known to rescue many of the starvation-induced phenotypes of wildtype (WT) cells, including the depolymerization of the actin cytoskeleton (Uesono et al., 2004) and the collapse of global polysome profiles (Ashe et al., 2000). Moreover, a deletion of *REG1* also prevents the reduction of intracellular pH (pH_i) normally observed in glucose-starved cells (Young et al., 2010). We therefore hypothesized that *REG1* may be involved in the signaling pathway which stimulates the confinement of macromolecular mobility and thus investigated the relationship between *REG1*, pH_i, and starvation.

Results and Discussion

We first confirmed that *reg1*Δ cells maintain a more neutral pH_i upon glucose starvation (**Fig A.1A**). Indeed, whereas the pH_i of wildtype cells reduced from pH ~7.2 to pH ~6.4 upon glucose starvation, the pH_i of *reg1*Δ cells only reduced to pH ~6.9 from an initial value of pH ~7.0. Because Reg1 is repressed during growth on non-fermentable carbon sources (Ruiz et al., 2011), we next investigated whether or not the substantial drop in pH_i still occurs in cells acutely starved for galactose. Notably, acute starvation from galactose induces a more temperate reduction in pH_i than glucose starvation, but does not fully phenocopy *reg1*Δ cells (**Fig A.1A**). This suggests that the full maintenance of a neutral pH_i is specific to *reg1*Δ mutants acutely starved for glucose.

A deletion of *REG1* was previously reported to rescue the starvation-induced depolymerization of the actin cytoskeleton (Uesono et al., 2004). Moreover, we preveiously demonstrated that an artificial reduction of pH_i is sufficient to perturb the actin cytoskeleton (**Chap 4**). We therefore hypothesized, given the relatively neutral pH_i of galactose-starved cells, that wildtype cells acutely starved for galactose would also maintain a robust network of actin. To investigate this, we acutely starved cells of galactose prior to staining cells with phalloidin and quantified the number of cells with filamentous actin. Interestingly, this experiment revealed that galactose-starved cells maintained a higher frequency of filamentous actin despite already having a decreased abundance during logarithmic growth (**Fig A.1B**). Indeed, normalizing the percentage of cells with detectable filaments to pre-starvation levels reveals that ~30% of galactose-starved cells maintain filamentous actin compared to only ~2% of glucose-starved cells.

Our previous experiments (**Chap 4**) suggested that the starvation-induced depolymerization of the actin cytoskeleton may function, in part, to preserve intracellular ATP. If this is indeed the case, we would then expect that galactose-starved WT cells and *reg1*Δ mutants acutely starved for glucose to have a higher concentration of intracellular ATP, which would then sustain the residual activity of the actin cytoskeleton. To explore this possibility, we utilized a luciferase-based ATP assay to quantify intracellular concentrations of ATP upon starvation (Ashe et al., 2000).

Figure A1

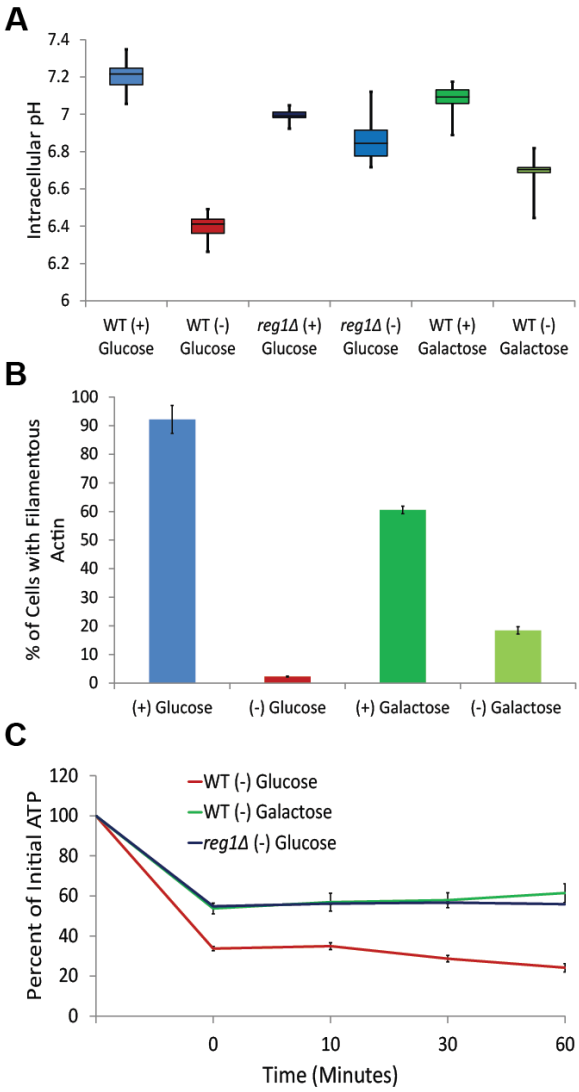

Figure A1: Quantification of the intracellular environment of acutely-starved cells. **A.** Intracellular pH after acute starvation. Log-growing cells were acutely starved for thirty minutes prior to ratiometric imaging of the pH-biosensor, pHlourin. Intracellular pH values were estimated based on comparison to a standard curve (data not shown) (Orij et al., 2009). Values from biological replicates were pooled and compiled into boxplots. **B.** Quantification of filamentous actin before and after acute starvation from glucose or galactose. Log-growing cells were acutely starved for thirty minutes prior to fixation and staining with phalloidin. Cells were classified based on the presence or absence of detectable filaments. Error bars represent SEM for three biological replicates. **C.** Intracellular ATP concentrations after acute starvation. Log-growing cells were acutely starved and ATP concentrations quantified using a luciferase-based ATP assay (Ashe et al., 2000). The 0 min time point was taken immediately after starvation. Concentrations were normalized to pre-starvation levels (Initial ATP). Error bars represent the variation between biological replicates.

Notably, both galactose-starved WT cells and glucose-starved *reg1*Δ mutants maintain an intracellular ATP concentration which is nearly double that of glucose-starved WT cells (**Fig A.1C**). Importantly, ATP concentrations were virtually identical prior to starvation (data not shown). Thus, we conclude that the residual activity of the actin cytoskeleton observed in both galactose-starved cells and *reg1*Δ mutants is likely fostered, in part, through a relative abundance of intracellular ATP.

These experiments suggested that galactose-starved WT cells and *reg1*Δ mutants acutely starved for glucose may maintain an intracellular environment sufficient to sustain chromatin mobility, given the relatively neutral pHi (**Fig A.1A**), abundance of ATP (**Fig A.1B**), and residual activity of the actin cytoskeleton (**Fig A.1C**) (**Chap 4**). To test this possibility, we monitored the mobility of the *POA1* locus in WT cells acutely starved for both glucose and galactose, as well as *reg1*Δ mutants acutely starved for glucose. As expected (**Chap 4**), glucose starvation of WT cells resulted in a massive confinement of the *POA1* locus (**Fig A.2A**). Astonishingly, in contrast, galactose starvation of WT cells only moderately reduced chromatin mobility, and acute glucose starvation of *reg1*Δ mutants resulted in only a temperate decrease of mobility (**Fig A.2A**).

Given our previous work describing the pH_i-induced confinement of macromolecular mobility (**Chap 4**), we hypothesized that the sustained chromatin mobility in galactose-starved WT cells and glucose-starved *reg1*Δ mutants may be a direct consequence of their neutral intracellular pH. This would also suggest that the contraction in cell size observed upon glucose starvation is prompted by the reduction of intracellular pH (**Chap 4**). As previously described (Dechant et al., 2010), we therefore acutely starved WT cells of glucose in media at pH 7.4, which prevents the normal reduction in intracellular pH. Despite maintaining a neutral pH, however, chromatin mobility is still substantially confined in cells acutely starved for glucose at pH 7.4 (**Fig A.2B**). Thus, we conclude that the relatively neutral pH_i of galactose-starved cells and *reg1*Δ mutants is insufficient to sustain chromatin mobility and, consistent with our previous results (**Chap 4**), that the drop in intracellular pH is unlikely to prompt cell contraction upon starvation.

Interestingly, the acidification of the yeast cytosol has been hypothesized to function in the cessation of PKA signaling upon glucose starvation (Dechant et al., 2010). We therefore wondered if artificially maintaining a neutral pH_i, through starvation at pH 7.4, induced pleiotropic effects within the cell, which may confound our results. Indeed, whereas various other experiments uncovered no such effects (data not shown), analysis of ATP levels revealed that glucose starvation at pH 7.4 prompts a thorough depletion of intracellular ATP (**Fig A.3A**).

Importantly, if the observed depletion of intracellular ATP was induced solely through constitutive PKA signaling, we postulated that starving cells at pH 5.0 (to inhibit PKA) before incubation at pH 7.4 would prevent the exhaustion of ATP. To our surprise however, cells acutely starved for glucose and maintained in SC pH 5.0 for an hour still rapidly deplete intracellular ATP when subsequently incubated at pH 7.4 (**Fig A.3B**). This suggests that the acidification of the yeast cytosol plays an additional role in cellular metabolism beyond its hypothesized function in the cessation of PKA signaling (Dechant et al., 2010). Moreover, the pH 7.4-induced exhaustion of ATP is remarkably similar to the phenotype described for glucose-starved *cbp2*Δ cells which are deficient in

Figure A2

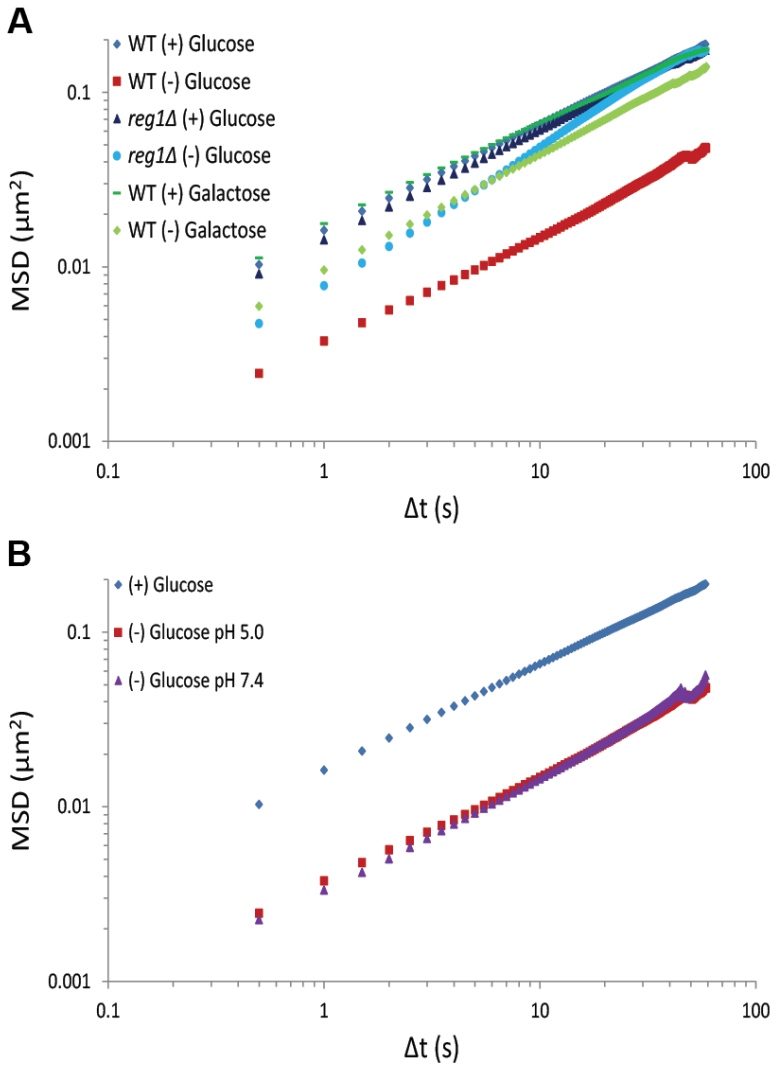

Figure A2: Mobility of the *POA1* locus after acute starvation.
A. Log-Log Mean Square Displacement (MSD) plot of the *POA1* locus during log-growth and after acute starvation. Log-growing cells were acutely starved for thirty minutes prior to time-lapse imaging and particle tracking of the *POA1* locus tagged with 256 LacO repeats (Green et al., 2012). Ensemble averaged MSDs were compiled from 300-1000 minute-long trajectories (0.5 sec frame rate) in each condition.
B. Log-Log MSD plot of the *POA1* locus during log-growth and after acute starvation in (-)glucose media at pH 5.0 or pH 7.4. Log-growing cells were acutely starved for thirty minutes prior to time-lapse imaging and particle tracking of the *POA1* locus. Ensemble averaged MSDs were compiled from 300-1000 minute-long trajectories (0.5 sec frame rate) in each condition.

mitochondrial function (**Chap 4**). This indicates that the starvation-induced acidification of the yeast cytosol may play an essential role in establishing a cellular environment conducive to oxidative phosphorylation, representing a global and pervasive mechanism to regulate cellular metabolism. Consistent with this, we find that prolonged starvation at pH 7.4 results in a massive decline in cellular viability (**Fig A.3C**). More experiments are necessary, however, to elucidate the true function(s) of cytosolic acidification, as well as the additional mechanisms utilized by cells to maintain viability during starvation.

Figure A3

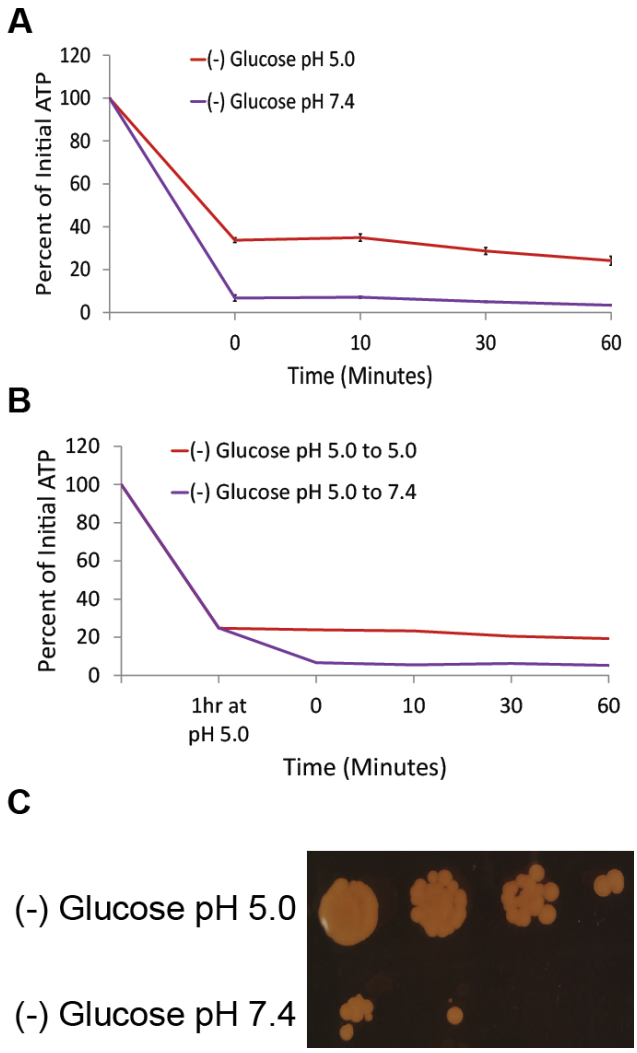

Figure A3: Glucose starvation at pH7.4 rapidly exhausts intracellular ATP.
A. Intracellular ATP concentrations after acute starvation in (-) glucose media at pH 5.0 or pH 7.4. Log-growing cells were acutely starved and ATP concentrations quantified using a luciferase-based ATP assay. The 0 min time point was taken immediately after starvation. Concentrations were normalized to pre-starvation levels (Initial ATP). Error bars represent the variation between biological replicates.
B. Intracellular ATP concentrations from log-growing cells acutely starved in (-) glucose media at pH 5.0, incubated for an hour, split and concentrated, and then resuspended in (-) glucose media at either pH 5.0 or pH 7.4. The 0 min time point was taken immediately after resuspension. Concentrations were normalized to pre-starvation levels (Initial ATP).
C. Cell viability after prolonged 24hr starvation in (-) glucose media at pH 5.0 or 7.4. Log-growing cells were acutely starved in (-) glucose media at pH 5.0 or 7.4 for 24hrs before frogging onto YPD plates and growing at 30ºC for 2 days.

Materials and Methods

Strains and Growth

Yeast strains used in this study are of the W303 strain-background. Genotypes for every strain are listed in **Table A1**; plasmids are described in **Table A2**. Unless otherwise indicated, cells were grown at room temperature (22ºC) in synthetic complete (SC) media at pH 5.0 (titrated with 1M HCl) containing 2% Dextrose (SCD). Specific dropout media was used to maintain plasmids when necessary.

Imaging and Particle Tracking

Time-lapse fluorescence imaging was performed using an inverted Nikon TE2000 microscope equipped with an Andor CCD camera, a motorized stage (ASI), 60X/1.49NA APO TIRF oil immersion objective, and controlled with Metamorph® software. Cells were stabilized by coating the glass-bottom of MatTek dishes (MatTek Corporation, PG35G-1.5-14-C) with 0.2% Concanavalin A and aspirating the solution prior to adding 300μL of OD_{600} 0.2-0.3 cells. All imaging was performed at room temperature (22ºC). Images were analyzed and particles tracked using custom MatLab (The MathWorks, Inc.) scripts based on the 2D feature finding and particle tracking software made available by Maria Kinfoil (Pelletier et al., 2009; http://people.umass.edu/kilfoil/downloads.html).

Ensemble averaged MSDs were calculated for each condition using the equation:

$$MSD\tau = \langle \left(r_{(t+\tau)} - r_t \right)^2 \rangle$$

Acute Starvation

5mL of cells grown in SCD media (OD_{600}=0.4-0.7) were collected by centrifugation (3000rpm) for 2min. The supernatant was then removed and cells resuspended in 1mL of SC media. Four additional wash steps followed, with two 2min spins (6000rpm) succeeded by two 1min spins. The OD_{600} of the final cell suspension was determined and cells diluted into fresh SC or SCD media for analysis.

ATP Measurements

The protocol employed was only marginally modified from Ashe et al. (2000). Briefly, 20μL of sample (KWY 1622 cells in culture) was added to 20μL of 10% TCA and immediately vortexed for 1min. 10μL of the 40μL solution was then added to 990μL of ATP reaction buffer (25 mM HEPES, 2 mM EDTA, pH 7.75). After the time course, 50μL of a luciferin/luciferase kit (ATP Determination Kit, Sensitive Assay - B-Bridge International, Inc.) was directly added to 50μL of the buffered-ATP solutions and briefly mixed by pipetting the solutions in a Corning® 96-well opaque white plate. Reactions were allowed to transpire in the dark for 10min at room temperature. Luminescence was then measured using a Tecan Infinite® 200 Pro microplatereader, which was set for

a 10sec integration time and no attenuation. Sample aliquots were taken at 0, 10, 30, and 60 minutes and standardized to a pre-treatment control. ATP concentrations were also corrected for OD_{600} at the beginning and end of each time course. ATP standards were used to generate a standard curve to insure linearity and estimate intracellular ATP concentrations.

Filamentous Actin Quantification

To quantify filamentous actin, KWY 165 cells were fixed with formaldehyde at a final concentration of 4% for 15min. Fixed cells were washed twice with potassium phosphate buffer and resuspended into PBS-BSA. Cells were then stained with Alexa Fluor 568-phalloidin (Invitrogen) and Hoechst stain. Samples were incubated in the dark at room temperature for one hour and washed again with PBS-BSA prior to imaging (Laporte et al., 2011). Background was subtracted from z-stacks (0.15µm steps over 3µm) taken with a 100X/1.49NA APO TIRF oil immersion objective using a rolling ball radius of 1 pixel in ImageJ (NIH). Maximal intensity projections were then blinded and cells classified based on the presence or absence of identifiable filamentous or bundled actin.

pH Measurements

The pHlourin calibration protocol was slightly adapted from Orij et al., (2009) to establish a standard curve. 50µg/mL (in PBS) of digitonin was used to permeabalize cells for 10min. After washing cells in PBS and placing them on ice, cells were then incubated in citric acid/Na_2HPO_4 buffer with pH values ranging from pH 5.0 to pH 8.0. pHlourin emission intensity ratios resulting from 390nm and 470nm excitation ($R_{390nm/470nm}$) were then calculated from calibration images (taken with a 100X/1.49NA APO TIRF oil immersion objective) using a custom script in ImageJ (NIH) and compared to the pH values of the corresponding buffer. The resulting curve was used to estimate experimental intracellular pH values generated from emission ratios produced from the same ImageJ script.

Table A1: Yeast strains used in this study.

Strain #	Genotype	Source
KWY 165	*MATa* ura3-*1 leu2-3 his3-11,15 trp1-1 ade2-1*	This Study
KWY 1622	*MATα ybr022w::256LacO::LEU2 his3::LacI-GFP::HIS3 trp1::dsRED-HDEL::TRP1*	Green et al., 2012
KWY 3420	*KWY 1622, reg1∆::KANMX*	This Study
KWY 3661	*KWY 165, pHlourin::URA3*	This Study
KWY 3935	*KWY 165, reg1∆::KANMX pHlourin::URA3*	This Study

W303 Background:
*MAT*a/*MAT*α *leu2-3,112 trp1-1 can1-100 ura3-1 ade2-1 his3-11, 15*

Table A2: Plasmids used in this study.

Plasmid	Description	Source
pKW 2957	pYES2-PACT1-pHluorin (CEN, URA3)	Orij et al., 2009

Appendix References

Ashe MP, De Long SK, Sachs AB. Glucose depletion rapidly inhibits translation initiation in yeast. Mol Biol Cell. 2000 Mar;11(3):833-48. PubMed PMID: 10712503; PubMed Central PMCID: PMC14814.

Dechant R, Binda M, Lee SS, Pelet S, Winderickx J, Peter M. Cytosolic pH is a second messenger for glucose and regulates the PKA pathway through V-ATPase. EMBO J. 2010 Aug 4;29(15):2515-26. doi: 10.1038/emboj.2010.138. Epub 2010 Jun 25. PubMed PMID: 20581803; PubMed Central PMCID: PMC2928683.

Green EM, Jiang Y, Joyner R, Weis K. A negative feedback loop at the nuclear periphery regulates GAL gene expression. Mol Biol Cell. 2012 Apr;23(7):1367-75. doi: 10.1091/mbc.E11-06-0547. Epub 2012 Feb 9. PubMed PMID: 22323286; PubMed Central PMCID: PMC3315802.

Orij R, Postmus J, Ter Beek A, Brul S, Smits GJ. In vivo measurement of cytosolic and mitochondrial pH using a pH-sensitive GFP derivative in Saccharomyces cerevisiae reveals a relation between intracellular pH and growth. Microbiology. 2009 Jan;155(Pt 1):268-78. doi: 10.1099/mic.0.022038-0. PubMed PMID: 19118367.

Pelletier V, Gal N, Fournier P, Kilfoil ML. Microrheology of microtubule solutions and actin-microtubule composite networks. Phys Rev Lett. 2009 May 8;102(18):188303. Epub 2009 May 7. PubMed PMID: 19518917.

Ruiz A, Xu X, Carlson M. Roles of two protein phosphatases, Reg1-Glc7 and Sit4, and glycogen synthesis in regulation of SNF1 protein kinase. Proc Natl Acad Sci U S A. 2011 Apr 19;108(16):6349-54. doi: 10.1073/pnas.1102758108. Epub 2011 Apr 4. PubMed PMID: 21464305; PubMed Central PMCID: PMC3081026.

Uesono Y, Ashe MP, Toh-E A. Simultaneous yet independent regulation of actin cytoskeletal organization and translation initiation by glucose in Saccharomyces cerevisiae. Mol Biol Cell. 2004 Apr;15(4):1544-56. Epub 2004 Jan 23. PubMed PMID: 14742701; PubMed Central PMCID: PMC379254.

Young BP, Shin JJ, Orij R, Chao JT, Li SC, Guan XL, Khong A, Jan E, Wenk MR, Prinz WA, Smits GJ, Loewen CJ. Phosphatidic acid is a pH biosensor that links membrane biogenesis to metabolism. Science. 2010 Aug 27;329(5995):1085-8. doi: 10.1126/science.1191026. PubMed PMID: 20798321.